Atomistic Simulation Studies of Alkali Ion Conducting Superionic Conductors

by

Krishnanjan Pramanik

A thesis submitted
in Partial Fulfillment of the Requirements
for the Degree of

DOCTOR OF PHILOSOPHY.

Department of Physics
Indian Institute of Technology Guwahati
Guwahati 781039, India.

November 2020


भारतीय प्रौद्योगिकी संस्थान गुवाहाटी
Indian Institute of Technology Guwahati

CERTIFICATE

It is certified that the work contained in the thesis entitled "*Atomistic Simulation Studies of Alkali Ion Conducting Superionic Conductors*" by Mr. Krishnanjan Pramanik, a student of Department of Physics, IIT Guwahati, was carried out under my supervision and has not been submitted elsewhere for award of any degree.

Prof. Padma Kumar Padmanabhan,
Department of Physics, IIT Guwahati,
Guwahati-781039, Assam, India.
NOVEMBER, 2020

ACKNOWLEDGMENTS

First and foremost, I am gratefull to my thesis supervisor, Prof. Padma Kumar Padmanabhan, for giving me the chance to work with him and constantly guiding me through the nitty-gritty of the field. He has always been patient with me.

Prof. Subhradip Ghosh, not only the chairman of my doctoral committee but also a guardian for all these years of my stay in IITG campus. His statistical mechanics course during my course work days helped me to a great extend to reshape the way I percieve science.

Other members of my doctoral committee, Prof. Subhash Thota and Prof. Dipankar Bandyopadhayay, have always motivated me through their critical questions and comments on my works.

Prof. Saurabh Basu, Prof. P Poulose and Prof. Subhradip Ghosh, the previous and the current heads of the department of physics, thank you for all the supports.

Basab B Purakayastha, Hemanta Medhi, members of the technical team of the department, thank you for all the helps that I got from you. My sincere gratitutde to Dr. Sidananda Sarma for always being there for every kind of help, no matter if its official or not. I would also like to thank Mr. Aditya Kalita, and Mr. Lokesh Chakravorty, specially for taking me to the Guwahati science fair back in 2016. Those two days are important in my life for various reasons.

Thanks to Supriyo da, Kartik, Sangkha, with whom I've worked extensively and from whom I've learned many things. Sudeshna, Sunil, it was really wonderful working with you during the last couple of years of my Ph.D.

Lastly, I'm indebted to IITG campus, to Guwahati, to Assam, to the north-east, for everything, for every single thing.

ABSTRACT

Designing of *all-solid-state-battery* by replacing the currently used liquid/gel electrolytes with solid ones is the prospect of next generation energy storage devices. This advancement promises higher energy density, safety and longer operating cycles. However, the progress towards the commercial realization of such devices demands microscopic insights on various factors, including the mechanism of ion transport in solids. This calls for computational investigations complementing experimental studies. In this thesis, computational studies of some of the promising classes of Li/Na-ion conducting solids are presented. The first chapter of the thesis is devoted to the review of the ongoing research on Li/Na-ion conducting inorganic solids. In the second chapter, the theoretical background of the computational methods, such as classical and *ab initio* molecular dynamics, metadynamics, nudged elastic band method, etc. employed in the studies are discussed. The third chapter presents fresh atomic-scale insights on the role of framework dynamics on ion transport in Li-substituted NASICONs ($LiM_2P_3O_{12}$ where M = Zr, Hf, Sn, Ti) based on classical molecular dynamics study. The fourth chapter of the thesis addresses the 'time scale' issue of standard molecular dynamics simulation in the study of slow diffusing systems. Plugged in with classical molecular dynamics, the utility of metadynamics technique has been demonstrated by taking the low diffusing phosphate and silicate end members of the *true*-NASICON family $Na_{1+x}Zr_2Si_xP_{3-x}O_{12}$ ($0 \leq x \leq 3$) as the prototype systems. This utility is further explored in the fifth chapter by using metadynamics interfaced with *ab initio* molecular dynamics, to understand the Li migration mechanism in γ-Li_3PS_4. The sixth chapter summarizes the results.

TABLE OF CONTENTS

CHAPTER 1

INTRODUCTION

One of the major concerns currently before mankind is that of environmental conservation. The unscrupulous use of fossil fuels in the last several decades in particular, has inflicted a fatal scar on our planet, in the form of global warming and consequent environmental damages. To overcome this crisis, development of alternative and sustainable green energy sources, replacing fossil fuels, is necessary. The evolving strategy is mutli-faceted, and involves harvesting of natural power sources such as solar and wind, to development of environmentally benign energy devices including batteries and fuel cells. Apart from powering automobiles, portable energy sources such as batteries attract great demands from the ever growing market of compact electronic gadgets.

Historically the concept of converting chemical energy into electrical through a device is due to Alessandro Volta in 1800. Known as Voltaic pile, with zinc and copper used as the electrodes and brine (concentrated solution of NaCl) soaked cloth as electrolyte, it was the first device that could provide continuous electric current [1, 2]. Three decades later John F. Daniell designed an improved version of the Volta cell, with copper sulfate and dilute sulfuric acid as electrolytes that provide much steadier power [3, 4]. The first known rechargeable battery was designed by Gaston Plante using lead-acid in 1859 [2, 5, 6]. In 1899, Waldmar Jungner invented another rechargeable battery, called nickle-cadmium (NiCd) battery, in which nickle was used as cathode and cadmium was used as anode material[5]. For the major part of the twentieth century, these lead-acid and NiCd rechargeable batteries were largely the choice for almost all kind of technological applications. Even in modern days, despite its toxicity, lead-acid batteries are extensively used in automobiles, power back up systems, etc. Later on NiCd batteries were gradually replaced by somewhat safer NiMH (Nickel metal hydride) batteries [7].

However, over the last couple of decades, with the surge in compact and portable electronic gadgets, the demand for batteries with much higher energy density intensified. This motivated the search for new generation of energy storage devices leading to the development of lithium ion batteries (LIBs). First commercialized by Sony in 1991, these LIBs were a major breakthrough in technology [8, 9]. Standard LIBs are constructed with lithium intercalated graphite as anode and Li_xCoO_2 as cathode material which are good electronic conductors as well. Non-aqueous solutions or gels of Li salts, such as $LiPF_6$, $LiClO_4$, etc., are used as the electrolytes. Recently, more efficient LIBs are proposed, such as lithium-sulphur, lithium-silicon, lithium-air batteries [10–20]. Nevertheless, these liquid/gel electrolytes come with major issues related to longevity and safety, as they are flammable. Replacing the liquid/gel electrolyte with solid state electrolyte, is one of the major directions of research in the present day, as it promises safer and high energy density devices. Solid electrolytes scores over the current liquid/gel electrolytes in various aspects. Solid electrolytes offer better safety as they inhibit the growths of dendrites that leads to short-circuits causing fire. All-solid-state batteries also promise better thermal and chemical stability at the electrode/electrolyte interface, yielding longer battery life. Inorganic solid electrolyte materials, in particular, can operate over wider ranges of temperatures improving their reliability. Another advantage of solid electrolytes is the absence of bulk polarization as the anionic frameworks, by and large, stay rigid allowing higher current density.

Materials that exhibit high ionic conductivity ($> 10^{-4}\ S/cm$) are known as fast ion conductors or superionic conductors [21–25]. Fast ion conducting solids, but having negligible electronic conductivity, are promising candidates as solid electrolytes. The discovery of fast ion conductors can be traced way back to 1830's when Faraday discovered low electrical resistance in Ag_2S and PbF_2 and accounted the phenomenon to the existence of mobile charge carriers other than those responsible for the high electrical conductivity in metals, now realized as electrons. Two materials in particular, AgI and $\beta-alumina$ ($M_2O \cdot 11Al_2O_3$, where M = Li, Na, Ag, K or Rb), having ionic conductivity of the order of $10\ mS/cm$ at $300K$ were among the most popular fast ion conductors during the initial periods of development. Probably, these materials inspired the creation of a new scientific sub-discipline named "Solid State Ionics", since Takehiko Takahashi. [26, 27]

In 1976, Hong and Goodenough *et al.* [28, 29] reported the synthesis and characterization of a few families of fast ion conductors, having *skeleton structures*. This is regarded as a major breakthrough in the field of fast ion conductors, and in recognition of the contribution John B Goodenough was awarded Nobel prize for chemistry in 2019, along with Stanley Whittingham and Akira Yoshino. It shall be noted that prior to Hong and Goodenough *et al.* [28, 29] it was generally believed that only soft framework structures such as AgI, Ag_2S etc. (opposed to strongly covalently bonded framework solids) could favor fast ion transport, taking beta-alumina an exception. Among the skeleton structures synthesized by Hong and Goodenough *et al.*, NASICON (acronym for Na^+ Super Ionic CONductor) structural family, with the general formula $Na_{1+x}Zr_2Si_xP_{3-x}O_{12}$ stood out as the most promising class of materials for solid electrolytes. The material has been very popular over these years for their structural, chemical and thermodynamic stability over a wide range of ionic substitutions. This spurred rigorous research works on fast ion conductors particularly pertaining to the class of skeleton structures that promises the feasibility of a new generation of batteries entirely of the solid components. Nevertheless, practical realization of all-solid-state batteries demands that apart from having high ionic conductivity at ambient temperatures, the electrolyte materials should maintain high thermal and chemical stability, along with low contact resistance, at their interface with the electrodes [30–48].

Over the last couple of decades several fast ion conducting solids have been synthesized and their utility in battery and fuel-cell applications are being examined. Among these are solids conducting electricity via, oxide ions (O^{2-}) [49–53], protons (H^+) [54–56], fluoride (F^-) [57–59], copper (Cu^{2+}) [60, 61], silver (Ag^+) [62–64], and alkali ions (Li^+ and Na^+) [65–67]. Among these oxide ion and protonic conductors find enormous application in the development of fuel-cells. Cu^{2+} conductors discovered are very limited in number, and are of high activation energy due to the higher charge of the species. Fluoride ion conductors are highly toxic in nature thus are of limited practical applications. Li^+ and Na^+ ion conducting solids are believed to be the most promising materials for all solid state batteries, and are being extensively studied since the last couple of decades. Silver ion conductors are too expensive for large scale applications. However, they have been subject of rigorous studies in the past, particularly of theoretical and computational nature, providing better understanding of the diffusion phenomena in solids. Hence the rest of the discussion in this chapter will focus on promising families of Li^+ and Na^+ conducting inorganic solids, along with Ag^+ conductors – in view of their academic interest.

1.1 Ag^+ Ion Conductor

The most well known and widely studied Ag^+ ion conductor is perhaps silver iodide (AgI), the inception of which can be traced back to 1914. While studying electrical properties of different silver halides, Tubandt and Lorenz [68] discovered that the solid AgI exhibits ionic conductivity comparable to that of liquid electrolytes. In comparison to AgBr or AgCl, it was found that AgI has the highest conducting solid phase which was later named as the α-AgI [69]. The low temperature phase, known as β-AgI exhibits low ionic conduction owing to its hexagonal close packed (*hcp*) configuration of the I ions. The $\beta \leftrightarrow \alpha$ phase transition occurs at a temperature around 420 K. In the α phase, the I ions form *bcc* configuration among which the Ag^+ ions are reported to occupy three crystallographic positions, namely the octahedral $6b$ sites, tetrahedral $12d$ sites and trigonal $24h$ sites [70–72]. In their seminal work, Vashishtha and Rahman carried out classical molecular dynamics (MD) simulation to investigate the ion dynamics in α-AgI by employing an empirical interaction potential [73]. The study showed that majority of ion jumps occur between neighbouring tetrahedral $12d$ sites along [110] direction. Later in 1983, Parrinello *et al.* extended the work to investigate the $\beta - \alpha$ phase transition in AgI employing isothermal-isobaric (NPT) ensemble MD techniques [74]. In 2008, *Ab initio* MD study was carried out on the α-AgI by Sun *et al.*, and the migration mechanism of Ag^+ ions through the framework structure was revisited [75].

As the high conducting α phase occurs at a temperature much higher than ambient temperature, efforts had been used to stabilize the *bcc* phase at the room temperature by means of doping different elements in the framework. One such early attempt was perhaps by Takahashi *et al.* back in 1964, through anionic substitution in the system which resulted the material Ag_3SI [76]. At room temperature, the framework (immobile species) forms a *bcc* cell in which the I^- ions occupies the corners of the cube and the S^- ion occupies the center. The material exhibited appreciable conductivity (10 mS/cm), but had stability issues. Different cationic substitutions also have been investigated in past years, among which a popular material is Ag_4RbI_5, that has a cubic structure with an ionic conductivity of about 20 mS/cm at room temperature [77–81]. Another set of quasi-binary systems based on α-AgI, namely $AgI-AgX$, where X = Br, Cl and AgMI where M = Cu, Cs, also stabilizes for a wide range of temperature as well as concentrations.

Both experimental and computational studies have been carried out on these materials in order to investigate the conductivity variation over different concentration range. It is found that in α-$AgI_{1-x}Cl_x$ ($0 < x < 0.25$) and in α-$Ag_{1-x}Cu_xI$ where ($0 < x < 0.25$) the conductivity decreases monotonically with the concentration of the dopant, respectively Cl and Cu, in the system [82–85]. Silver chalcogenides, Ag_2X where X = S, Se, Te, are another family of material, known for their mixed (both ionic and electronic) conductivity. Both S and Se compositions show α-AgI type structure at high temperature where S or Se make *bcc* framework and Ag occupies the tetrahedral and octahedral positions. On the other hand Ag_2Te is known to have an anti-fluorite type of structure [86–90].

First reported by Kuhs *et al.* back in 1979 [61], the argyrodites have been a center of research interest for a long time. The Ag argyrodites had gained attention for their appreciable ionic conductivity. The general formula is given as $Ag^{+}_{12-n-x}M^{n+}X^{2-}_{6-x}Y^{-}_{x}$ where M = Al, Ga, Si, Ge, Sn, P, or As ; X = S, Se, or Te and Y = Cl, Br, or I ($0 \leq x \leq 1$). Structural analysis over the years have concluded that there are two phases, the low temperature phase which stabilizes in various ordered structures and the higher temperature cubic phase with $F\bar{4}3m$ space group. The phase transition reportedly occurs at a temperature near the ambient temperature. The higher temperature phase shows good ionic conductivity [91–95]. In recent years, the Li^+ counterparts of this family, which is discussed in the later section, are also gaining scientific attention.

1.2 Li^+ and Na^+ Ion Conductors

A number of different families of fast ion conducting skeleton structures, having both Li^+ and Na^+ counterparts, such as LISICON, NASICONs, Perovskites, Garnets, etc. have been synthesized over the years, and is still a vibrant area of research [31, 45, 96–104].

1.2.1 LISICON

While trying to substitute Li^+ directly in NASICON, Hong *et al.* synthesized a material with chemical formula $Li_{14}Zn(GeO_4)_4$ which exhibited conductivity as high as 130 mS/cm at 300^o C [105]. Named as LISICON (Lithium superionic conductor) the material was reported to stabilize in orthorhombic structure with $Pnma$ space group. Four crystallographic sites for Li^+-ions have been reported in the LISICON framework, $[Li_{11}Zn(GeO_4)_4]^{3-}$. The remaining three Li^+-ions diffuse through the framework. Later studies reported that the material is highly reactive against Li metal and have a low room temperature conductivity (0.01 mS/cm) [106].

LISICON structures are known to be related to the γ-Li_3PO_4 structure. In γ-Li_3PO_4, the cations (*i.e.* P^{5+} and Li^+) are tetrahedrally connected with the O^{2-}. In the pure structure, all the Li^+-ions are located at perfect crystallographic sites for which they can only diffuse through the vacancy mechanism process which causes very low ionic conductivity [107–115]. But aliovalent doping, such as P^{5+} by Si^{4+} or Ge^{4+} can create interstitial positions to accommodate the extra Li^+-ions, and as an outcome conductivity can increase significantly. The general chemical formula for such doped Li_3PO_4 is given by $Li_{3+x}(P_{1-x}Si_x)O_4$ [105, 113, 116]. These materials also shows ionic conductivity of the order of 0.001 mS/cm at room temperature. In later research works, it has been observed that substituting oxygen by sulphur has a dramatic effect on the conductivity. These sulphur substituted materials, $Li_{3+x}(P_{1-x}Si_x)S_4$, known as $thio-LISICON$s, show at least three orders of magnitude higher conductivity at room temperature compared to LISIOCNs [117].

In 2011, Kamaya *et al.* reported a material with the chemical formula, $Li_{10}GeP_2S_{12}$ (LGPS), which exhibited a conductivity of 12 mS/cm, highest ever among inorganic solid electrolytes, reported till then[118]. The XRD data revealed that the structure differs from that of $thio-LISICON$. The LGPS structure stabilizes in the tetragonal cell with the space group $P4_2/nmc$. The framework is made of isolated PS_4 and GeS_4 tetrahedral wherein there are four different crystallographic sites for Li^+-ions - $4c$, $4d$, $8f$, and $16h$. The Li^+-ions located at the $4d$ sites contribute to the framework structure and believed to be less mobile. The initial analysis suggested the existence of dominant one dimensional diffusion pathway connected via the $16h$ and $8f$ sites. Later two different groups, Mo *et al.* and Hu *et al.* [119, 120], performed first principle MD simulation on LGPS and observed that diffusion across the *ab*-plane is also possible for Li^+-ions which suggests three dimensional conduction. In another study employing bond valence technique, Adams and Rao [121] also reported existence of three dimensional channel. Despite having an excellent conductivity at room temperature, the difficulties with devices involving LGPS are the cost of Ge which limits wider commercial applications and the sensitivity of sulfide based materials to air and moisture.

In a further development, Ong *et al.* [122] performed *ab-initio* MD on a group of materials with the general chemical formula $Li_{10\pm1}MP_2X_{12}$ where M = Ge, Si, Sn, Al or P and X = O, S or Se to investigate the phase stability, electrochemical stability and ionic conductivity across the series. The study concluded that Ge can be substituted with cheaper Sn or Si to address cost related disadvantage of LGPS. Such isovalent substitution have small effects on the desired properties. They also noted that aliovalent substitution with Al or P have small effect on the Li^+ diffusivity in the system. However, the issues related to sensitivity is difficult to overcome by O or Se substitutions. Followed by the computational study, Bron *et al.* [123] experimentally investigated $Li_{10}SiP_2S_{12}$ and found a conductivity of 4 mS/cm which is less than that of LGPS. In 2014, Kato *et al.* [124] did an experimental study on a series of similar material with general chemical formula $Li_{10}(Ge_{1-x}M_x)P_2S_{12}$ where M = Si, Sn. Both compositions exhibited single phase solid solution for $0 \leq x \leq 1.0$. The cell volume found to be monotonically increasing from $Li_{10}SiP_2S_{12}$ to $Li_{10}SnP_2S_{12}$ through the intermediate Ge system. But the conductivity was found to be initially increasing with the cell volume, showing the highest value of 8.6 mS/cm for $Li_{10}Ge_{0.95}Si_{0.05}P_2S_{12}$, comparable to the original LGPS system, and then decreased as the volume increased further with Sn substitution. This observation indicates that there is an optimum cell volume for which the Li^+ diffusion occurs at maximum rate. Much progress have been made in the synthesis of higher conducting materials such as $Li_{11}Si_2PS_{12}$ which shows even higher ionic conductivity than $LGPS$ [125]. Two new LGPS type material was reported by Kato *et al.* [126], $Li_{9.54}Si_{1.74}P_{1.44}S_{11.7}Cl_{0.3}$ and $Li_{9.6}P_3S_{12}$, the former having room temperature conductivity as high as 25 mS/cm. The electrochemical cell based on these materials was reported to have much better stability as well.

Sedlmaier *et al.* reported a newer material, Li_4PS_4I, from the quasy-ternary family $L_2S-P_2S_5-LiI$ in 2017 [127], the structure of which is made of layers of isolated PS_4^{3+} tetrahedral. The Li^+ diffuses through a three dimensional network. The conductivity reported for the system is 0.12 mS/cm at room temperature. Richards *et al.* [128], in 2016, performed an *ab-initio* MD study on $LiZnPS_4$, having *bcc* type framework, which known to be suitable for high ionic conductivity. Although the material exhibited poor conductivity, the study was extended to the derivatives of $LiZnPS_4$ by introducing interstitial defects in the structure. The derivatives are presented with the common chemical formula $Li_{1+2x}Zn_{1-x}PS_4$ $(0 \leq x \leq 0.75)$. The structure of $LiZnPS_4$ consists of layers of corner sharing PS_4 tetrahedral along the c-axis. The Zn and Li rich layers are sandwiched in between the PS_4 layers. The extra Li^+ ions occupies the vacant corner sharing tetrahedral sites in the PS_4 layers. The study showed that the extrapolated room temperature conductivity can reach up to 53.8 mS/cm within the solid solubility limit of $x = 0.5$, which is much higher than existing reports. It is predicted that if the solubility can be raised to $x = 0.75$, *i.e.* $Li_{2.5}Zn_{0.5}PS_4$, the conductivity may achieve an unprecedented value of 100 mS/cm [128]. In 2018, Kaup *et al.* [129] reported synthesis of $Li_{1.7}Zn_{0.65}PS_4$ and $Li_{1.2}Zn_{0.9}PS_4$ solids, which measures conductivities of 0.13 mS/cm and 0.0165 mS/cm respectively. This was however lower than the theoretical prediction. The probable causes of such lower conductivity are attributed to the inaccessibility of desired Li^+ defect concentration and the probability that the 'defect compositions' are meta-stable.

LPS family, also known as the $Li_2S-P_2S_5$ binary system, is another promising class of material for the designing of *all solid state battery* which show good ionic conductivity even without the incorporation of any dopant such as Ge, Si, Al. Absence of such metallic elements make the system electrochemically more stable [130]. Kudu *et al.* [131], in a detailed review have categorized five different species in this class: **a.** Ortho-thiophosphate, where the framework is made of isolated ${PS_4}^{3-}$ tetrahedral units, **b.** Hypo-thiodiphosphate, where the framework is made of two PS_3 units with $P-P$ bond, **c.** Pyro-thiophosphate, with two corner sharing PS_4 units, **d.** meta-thiodiphosphate, with two PS_4 units sharing edges, and **e.** meta-thiophosphate, ${PS_3}^-$ making polymeric chain.

The most intriguing material in the *LPS* family is perhaps $Li_7P_3S_{11}$, having very high conductivity of 17 mS/cm at room temperature, even higher than the *LGPS* system described previously [132, 133]. First principle MD study by Chu *et al.* [134] has found a highly correlated Li^+-ion motion in $Li_7P_3S_{11}$ system and the diffusion mechanism was also compared with that of *LGPS*. The AIMD study found conductivity value much higher than the experimental one (57 mS/cm compared to 17 mS/cm). Another well known material from the *LPS* family is Li_3PS_4 which exhibits four different phases [130, 135, 136]. This material has been studied in this thesis, thus shall be discussed in detail in chapter five of the thesis.

The Na counterpart of the above discussed Li-thiophosphate is currently undergoing a rigorous research for its high ionic conductivity, low grain boundary resistance, etc. It has been over a couple of decades since Na_3PS_4 is known as a Na^+ conductor [137–139]. This material has gained a fresh round of attention after Hayashi *et al.* [140] in 2012 reported successful stabilization of the high temperature cubic phase at ambient temperatures. The room temperature conductivity reported for this newly synthesised Na_3PS_4 was 0.2 mS/cm. Later in 2014, Hayashi *et al.* [141] reported an improved conductivity value of 0.46 mS/cm. The framework of cubic Na_3PS_4 (space group: $I\bar{4}3m$) is made of independent

PS_4 tetrahedral among which two distinct sites for Na^+ have been observed, 6*b* and 12*d*. It is to note that studies have suggested only small structural difference between the cubic and the tetragonal phases of Na_3PS_4 [142].

Since the achievement of Hayashi *et al.* [141], further efforts have been made to improve the conductivity value by various approaches. In 2014, a new pseudo-binary system, $(100-x)Na_3PS_4 \cdot xNa_4SiS_4$ was reported by Tanibata *et al.* [143, 144] in which a maximum conductivity value (0.74 mS/cm) was achieved for $x = 6$, *i.e.* $94Na_3PS_4 \cdot 6Na_4SiS_4$. Further observation showed that the partial substitution of Si for P results larger 12*d* site occupancy which causes the enhanced mobility for Na^+ ion. In another study, Zhang *et al.* [145] investigated the effect of substitution of larger Se^{2-} for S^{2-} in the cubic Na_3PS_4 The study was carried out for the series $Na_3PSe_{4-x}S_x$ $(0 \le x \le 4)$ and a very high ionic conductivity value 1.16 mS/cm was obtained for the $NaPSe_4$ at room temperature. Two factors were proposed for the increase in the conductivity with Se^{2-} incorporation: *a*) the larger cell volume and higher polarizability of Se^{2-} compared to S^{2-} which helps to provide optimum channel size for Na^+ while also weakens the attractive interaction between the framework and the mobile ion, and *b*) the resulting broader distribution of the 12*d* sites which enables additional interstitial sites for Na^+. Karuskopf *et al.* [146] investigated the effect of lattice softness on ionic conductivity in $Na_3PSe_{4-x}S_x$ and showed that the softening of vibrational frequency indeed play crucial role in Na^+ conduction. In 2016, there were at least three reports on derivative of Na_3PS_4, where in P^{5+} is substituted with Sb^{5+}[147–149]. The structure of Na_3SbS_4 was determined to be tetragonal with space group $P\bar{4}2_1c$. Banerjee *et al.* and Wang *et al.* [147, 148] reported the room temperature conductivity to be 1.1 mS/cm and 1 mS/cm respectively, whereas Zhang *et al.* [149] reported a conductivity ranging 3 mS/cm at room temperature to 16 mS/cm at 90^o C.

Another well known strategy to enhance the ionic conductivity is to introduce defects by various aliovalent substitution. Experimental effort had been made by Hibi *et al.* [150] by incorporating I^- in the system, resulting to $(100-x)Na_3PS_4 \cdot xNaI$ glass ceramic, but the conductivity obtained was not up to the desired value. Also the formation of an unknown phase indicated incompatibility to host large I^- in the framework. Later Chu *et al.* [151] conducted a study combining AIMD and experiment on tetragonal $Na_{3-x}PS_{4-x}Cl_x$ and reported an enhancement in the room temperature conductivity value (up to 1 mS/cm). Similar computational study with halogen substitution have also been carried out by Huang *et al.* [152] and a high conductivity of 2.37 mS/cm at ambient temperature is reported for the Br doped tetragonal Na_3PS_4. Recently, Moon *et al.* [153] carried out a study by partially substituting Ca^{2+} in the tetragonal Na_3PS_4 structure. This substitution resulted the series $Na_{3-2x}Ca_xPS_4$ ($0 < x \leq 0.375$) stabilizing in cubic phase. Also the Na vacancy induced by the divalent cation substitution enabled a much higher conductivity of 1 mS/cm at room temperature. Much exploration and progress have been made through many more various substitutions resulting new derivatives such as, Na_3SbSe_4 (3.7 mS/cm)[154], $Na_3P_{0.62}As_{0.38}S_4$ (1.46 mS/cm), $Na_{4-x}Sn_{1-x}Sb_xS_4$ (0.51 mS/cm)[155] etc., by different groups. Zhu *et al.* [156] conducted a computational study to investigate the phase stability, defect formation energy, and conductivity in $c-Na_3PS_4$ and on the series $Na_{3+x}M^{4+}_xP^{5+}_{1-x}S_4$ (M = Ge, Sn; x = 0.0625 and M = Si ; x = 0.0625, 0.125). They showed that pristine cubic-Na_3PS_4 is a poor conductor and incorporation of more Na^+ in the system through aliovalent doping is a major key to enhance the conductivity as the Si doped composition ($x = 0.0625$) showed a conductivity of 1.66 mS/cm in good agreement with experimental report. Interestingly the Sn composition exhibited a conductivity value 10.7 mS/cm which is much higher for the same $x = 0.0625$ concentration. Another computational study by Klerk *et al.* [157] showed that vacancy inducing through halogen F, Cl, Br, I doping in $c-Na_3PS_4$ can also enable high conduction, in agreement with the previously described study by Chu *et al.* [151] and Huang *et al.* [152]. Very recently, Femprikis *et al.* [158] reported the existence of a third polymorph, γ-Na_3PS_4, above 500^o C in which a 10 fold increment in conductivity is observed compared to the $\beta-phase$ ($c-Na_3PS_4$). The structure of this new phase is found to be orthorhombic ($Fddd$ space group). Five distinct sites for Na^+ are identified, namely $32h, 16g, 8f, 16f, 16g$. The PS_4 tetrahedral of the framework structure have the possibility of multiple conformations, indicating the character of a 'plastic crystal'. The study proposed that the Na^+ conduction is enhanced by the rotational dynamics of the PS_4 tetrahedra.

The Na counterpart of the famous $LGPS$, $Na_{10}GeP_2S_{12}$, was first theoretically predicted by Kandagal *et al.* [159] in 2015. The room temperature conductivity was predicted to be, 4.7 mS/cm. The first experimental synthesis of the material was reported by Tsuji *et al.* [160] and the conductivity was found to be around 0.01 mS/cm which is much lower than the theoretically predicted value. The reason of such discrepancy is not yet clear, but the 'order-disorder transition' has been pointed out to be a probable factor. Richards *et al.* [128] conducted a combined computational and experimental study on $Na_{10}MP_2S_{12}$ where M = Sn, Ge or Si. Their computations suggest that the activation energy changes across the series follows, $E_{Si} < E_{Ge} < E_{Sn}$. Experimentally they obtained appreciable conductivity (0.4 mS/cm) for the Si composition at room temperature. Another composition, $Na_{11}Sn_2PS_{12}$, was reported to exhibit a high conductivity value of 1.4 mS/cm at room temperature, and has a tetragonal structure (space group:$I4_1/acd:2$) [161–163]. Based on computational techniques Wang *et al.* [164] predicted another set of material, $A_7P_3X_{11}$ (A = Na, Li; X = O, S, Se), to have very high conductivity values in tune to 10.97 mS/cm and 12.56 mS/cm, respectively for $Na_7P_3S_{11}$ and $Na_7P_3Se_{11}$. Another major breakthrough came in 2019, again from Hayashi *et al.* [165], wherein they report a partially tungsten substituted Na_3SbS_4, namely $Na_{2.88}Sb_{0.88}W_{0.14}S_4$, to measure an unprecedented high conductivity value of 32 mS/cm at room temperature. Further understanding of the mechanism leading to the high Na^+ conductivity in this system is awaited.

1.2.2 Argyrodite

In 2008, Deiseroth *et al.* [166] reported the structure of Lithium argyrodite which has the chemical formula Li_6PS_5X where X = Cl, Br, I for the first time. The structure stabilizes in cubic form having space group $F\bar{4}3m$, similar to its Ag, Cu counterparts. The structure consists of isolated PS_4 tetrahedral units forming the cubic lattice. The Li^+-sites ($48h$ and $24g$), are arranged in octahedral formations, the centers of which are occupied by some of the remaining S/X ($4d$). The rest of the S/X ($4a$) are arranged in fcc formations[167]. Li^+ diffusion occurs via migration through these $48h$ and $24g$ sites. Li-Argyrodite are known to be high conducting material [168–171]. Klerk *et al.* [157] carried out *ab-initio* MD study on a series of high temperature phases (here it is to note that the phase transition temperature depends on the composition: without halogen, its above 450 K and with halogen its $170K$) of argyrodite materials (Li_7PS_6, Li_7PSe_6, Li_6PS_5X with X = Cl, Br, I) and investigated the influence of substitution of S with Se and also the substitution of chalcogen (S) with halogen. The study suggested that although Li^+ vacancy induced by halogen substitution is important for better diffusivity, the halogen distribution over the possible sites is equally crucial as it influence the Li^+ vacancy distribution which dictates the total conductivity. The MD study also predicted that conductivity as high as 10 mS/cm is achievable for argyrodite materials. Further experimental studies have been conducted to study the effect of different types of doping in the system. Bernges *et al.* [172] did an experimental study by incorporating Se in the structure, the chemical formula of which is $Li_6PS_{5-x}Se_xBr$ $[0 \leq x \leq 1.0]$. The study concluded that, firstly, incorporation of more polarizable Se in the system softened the lattice which caused the activation energy and the Arrhenius pre-factor to decrease at the same time. As a result no significant improvement in conductivity was observed. This observation is in tune with another study on argyrodites by Kraft *et al.* [173] where it has been concluded that the general belief that *softer the lattice, higher the conductivity* is not quite 'straightforward'. Secondly the disorder corresponding to Br^-/Ch^{2-} sites (where Ch stands for chalcogens) was found to decrease with Se content and disappeared for $x = 1$ which effected the arrangement of local Li^+ sub-lattice and this thwarted the effect of widening of the diffusion pathway due to the increase in the unit cell volume with Se substitution. The effect of the anion disorder is also recently investigated by Hanghofer *et al.* [167] for the parent series of argyrodite where it has been found that more ordered Li_6PS_5I shows low conductivity as the local clusters made of short range Li^+ hops are truncated from each other. Another recent study by Minafra *et al.* [174] on $Li_{6+x}P_{1-x}Si_xS_5Br$ $(0 \leq x \leq 0.5)$ found increase in the conductivity with Si content and shows maximum value at $x = 0.35$ attributed to the increment of number of Li^+ as well as the unit cell volume. Very recently, Kim *et al.* [175] reported an anomalously high conductivity of 10.2 mS/cm) at room temperature for $Li_{5.5}PS_{4.5}Cl_{1.5}$, highest for a halogen rich lithium argyrodite (HRLA). Also, Feng *et al.* [176] reported room temperature conductivity as high as 17 mS/cm for a very similar composition, $Li_{5.3}PS_{4.3}Cl_{1.7}$, and attributed it to the S/Cl disorder and redistribution Li-ions among the $48h$ and $24g$ sites. Perhaps the first study on the possibility of Na^+ argyrodite material is recently carried out by Ceder *et al.* [177] by employing first-principle computation with different pinctogen, chalcogen and halogen combinations. The study predicted both good stability and ionic conductivity for the Na−P−Se−X (X =Cl, Br, I) compositions.

1.2.3 Lithium Garnets

In a remarkable achievement Li^+-ion conducting garnet structures of the formula, $Li_5La_3M_2O_{12}$ where M = Nb, Ta, were first synthesized by Thangadurai *et al.* [178] in 2003. The material exhibited ionic conductivity of 0.001 mS/cm at 25^o C [179–181]. The general chemical formula of garnet is given by $A_3B_2(XO_4)_3$, where A = Ca, Mg, Y or La is a eight coordinated cationic site, B = Ga, Mn, Fe, Ni, Al or Cr is a six coordinated cationic site and X = Al, Si, Ge or V is four coordinated cationic site. The structure is cubic with the space group $Ia\bar{3}d$. Subsequently, in order to improve the Li^+ ion conductivity, extra lithium ions were incorporated in the system by substitution of different valance cations in A and B sites [182–184]. The series of garnet-like $Li_3Ln_3Te_2O_{12}$ where Ln = Y, Pr, Nd, Sm or Lu was studied by O'Callaghan *et al.* [185] to investigate the Li^+ conductivity. Across the series, the Li^+ ion occupies the tetrahedral $24d$ sites in the structure. The unit cell volume was found to increase with the ionic radius of Ln but the Li^+ conductivity was found to be very low for all the cases (maximum 0.01 mS/cm at 850^o C was obtained for Nd composition). This is indicative of the fact that the tetrahedral Li^+-ions are less mobile and do not contribute to the overall conductivity. In later study from the same group [186], garnet series with excess Li^+, $Li_{3+x}Nd_3Te_{2-x}Sb_xO_{12}$ ($x = 0.05 - 1.5$) was investigated and the Li^+ conductivity was found to improve dramatically, and reached the maximum value of 10 mS/cm for the composition $Li_{3.5}Nd_3Te_{1.5}Sb_{0.5}O_{12}$ at 400^o C. The extra Li^+-ions, which contribute to the bulk conductivity, occupies the distorted octahedral sites ($48g$ and $96h$). Increasing the number of Li^+-ion is considered to be one of the most effective way to enhance the ionic conductivity in garnet like materials.

Li^+ concentration had been increased by doping divalent ions at the trivalent La^{3+} sites. The general chemical formula of such series is given by $Li_6ALa_2M_2O_{12}$ where A = Mg, Ca, Sr or Ba and M = Nb, Ta [187–190]. It has been further reported that the pentavalent M sites can be substituted with tri or tetravalent ions which further increases the Li^+-ion concentration in the distorted octahedral sites and lower the concentration in the tetrahedral sites. Murugan *et al.* [191] synthesized *cubic* $Li_7La_3Zr_2O_{12}$ in 2007 and reported a high conductivity value of 0.1 mS/cm around room temperature. Later tetragonal $Li_7La_3Zr_2O_{12}$ structure was reported [192–195] in which the Li^+ ions are distributed in $8a$ tetrahedral sites and $16f$ and $32g$ octahedral sites. However, the ionic conductivity for this phase was found to be less (10^{-6} S/cm). Till date, among Li garnets promising high Li^+ conductivity at room temperature has been achieved for compositions, $Li_{6.55}La_3Zr_2Ga_{0.15}O_{12}$ and $Li_{6.4}La_3Zr_{1.4}Ta_{0.6}O_{12}$ [196–198].

Many computational studies have been carried out in order to unearth the atomic-scale insights of Li^+-garnets [199–205]. In 2004, Thangadurai *et al.* [206] performed a computational study on $Li_5La_3M_2O_{12}$ where M =Nb, Ta, using bond valance sum technique and investigated the hoping mechanism of Li^+ in the structure. The analysis suggested that the three dimensional diffusion network is made of '*non-planar*' squares constructed with four octahedral Li^+ sites with a tetrahedral Li^+ site at the center of it. As each octahedral Li^+ site is shared by two such planes, a mobile Li^+-ion has the probability to hop in any of the four directions to equivalent Li^+ sites. Later in 2012, Xu *et al.* [207] performed *ab-initio* NEB calculation on $Li_{3+x}La_3M_2O_{12}$ (M = Te, Nb and Zr) to find the minimum energy path for Li^+-ions. For $Li_3La_3Te_2O_{12}$, in which the tetrahedral $24d$ are the only occupied sites by Li^+, the ion jump found to be only possible to the neighbouring octahedral $48g$ or $96h$ sites. The energy barrier for such jumps came out to be as high as 1.5 eV. For $Li_5La_3Nb_2O_{12}$, the predominant mechanism found to be consisted of jump from the octahedral site to a neighbouring vacant octahedral site as they are partially filled by Li^+ ions. The energy barrier for this case came out to be 0.8 eV. And lastly, for $Li_7La_3Zr_2O_{12}$, as the population at the tetrahedral sites is lesser compared to that at the octahedral sites, the jumping mechanism was found to be between two octahedral sites through a tetrahedral site, the energy barrier for which came out to be 0.26 eV, minimum among the three cases.

1.2.4 Perovskite-type

The perovskite (ABO_3) materials are popular oxygen conductors and have applications in solid oxide fuel cells [50, 208–212]. Incorporation of Li^+ ion in the A-sites of perovskite structure, can result high Li^+ conductivity at room temperature[213]. Such aliovalent substitution results materials like $Li_{3x}La_{(\frac{2}{3}-x)}\square_{(\frac{1}{3}-2x)}TiO_3$ where $\square$ represents vacancies [214–217]. Excellent bulk conductivity has been observed in $Li_{0.34}La_{0.56}TiO_3$ at room temperature (1 mS/cm) [218]. Structurally, the compositions with low-Li^+ concentration are reported to have orthorhombic symmetry and those with high-Li^+ concentration have tetragonal symmetry. Studies have suggested that the La/Li distribution over the A sites are not random, rather arranged with La rich and La poor planes along the c-axis [219–226]. The diffusion pathway of Li^+ is mainly distributed in the ab-plane for the La-rich (*i.e.* poor-Li) cases. But for the Li-rich cases, in which vacancy concentration is also high, the diffusion is reported to be also possible in the c-direction and thus resulting a three dimensional network. The Li^+-ions migrate through the square bottlenecks made with *oxygen* ions, the size of which largely depends on the A-cation size [227]. Investigations have been carried out with different A-ion substitutions, such as Sm^{3+}, Pr^{3+}, Nd^{3+} and La^{3+}, among which the composition with La (having larger ionic radius than the rest) showed the highest conductivity [214, 228]. On the the other hand, partial incorporation of Sr, which has larger ionic radius than La, increased the conductivity. In 2000, Thangadurai *et al.* [229] carried out detailed investigation of the effect of different

B-ion substitution, which causes tuning of the B – O bonds, on the Li^+ conductivity. The study reported that the (Li, La)TiO_3 system with 0.5 mol of Al substitution shows the highest conductivity, and concluded that there exist an effect of the bond strength on the conductivity.

Zhao *et al.* [230], in 2012, proposed a new family of superionic conductors ((Cl, Br)OLi_3) based on anti-perovskite structure. The materials are structurally similar to perovskites, but "*electronically inverted*". That is, in the usual $A^+B^{2+}X^-$ perovskites, the A^+ and B^{2+} ions are replaced respectively by monovalent and divalent anions and the strongly electronegative X is replaced with electropositive cation, *i.e.* Li^+, resulting the anti-perovskite structure, $A^-B^{2-}X^+$. The ionic conductivity was reported to be 0.85 mS/cm for $ClOLi_3$ and 1.94 mS/cm for $Cl_{0.5}Br_{0.5}OLi_3$ at room temperature. Zhang *et al.* [231] carried out *ab-initio* MD study on the series and suggested that Li^+ vacancy and structural disorder enables higher ionic conductivity in anti-perovskites. Studies have been done to investigate the effects of different substitutions, like larger halide ions or divalent cations in the system. Braga *et al.* [232] reported a series of glassy electrolytes with anti-perovskite structure, $Li_{3-2x}M_xXO$ where M represents divalent cations such as Ca^{2+}, Mg^{2+} etc and X stands for halides (Cl^-, I^-), that exhibits very high conductivity (25 mS/cm) at room temperature. In their computational study, Emly *et al.* [233] proposed a cooperative jumping mechanism within the 'Li interstitial dumbbells' for the crystalline anti-perovskites. In another classical MD study, Mouta *et al.* [234] concluded that vacancies generated from Schottky defects plays major role in the ion diffusion mechanism in Li_3OCl, whereas in 'LiCl-deficient' materials where charge compensation creates Li^+ interstitial sites, the interstitial mechanism is dominating. However, the diffusion mechanism in anti-perovskite materials is still largely debatable and still undergoing rigorous research work [235, 236].

The Na^+ counter parts of the anti-perovskite material are also been researched for past few years[237]. In 2015 Wang *et al.* [238] newly proposed structural manipulation approach with $Na_3OCl_{1-x}Br_x$ ($0 < x < 1$) and $Na_3OBr_{1-x}I_x$ ($0 < x < 0.6$) to increase the Na^+ conductivity. In 2019, a new member Na_3OBH_4 was reported [239] which exhibited four orders of magnitude higher conductivity than the standard Na-rich anti-perovskites at room temperature. A very recent report [237] investigated the effect of halide substitution in Na_3OX where X = Cl, Br, BH_4. Although the previously reported [239] high room temperature conductivity in Na_3OBH_4 could not be reproduced, the study suggested that the size of halogen determines the lattice volume and thus the Na^+ conductivity. It was also proposed that the polarizability of the halogen effects the activation energy via lattice softness, thus partial substitution of O^{2-} with S^{2-} can increase the conductivity.

1.2.5 NASICON-type

Na SuperIonic CONductors ($NASICON$), first reported by Hong and Goodenough *et al.* [28, 29] are another promising class of material for a variety of technological applications, including that as solid electrolytes. The typical chemical formula of this family is $Na_{1+x}Zr_2Si_xP_{3-x}O_{12}$ $(0 \leq x \leq 3)$, and generally stabilize in the rhombohedral phase with space group ($R\bar{3}c$). However, compositions ranging between $1.8 \leq x \leq 2.2$ is reported to have structural distortion at room temperature, where it stabilizes in monoclinic $C2/c$ unit cell. Above 423 K, all the compositions stabilizes in rhombohedral $R\bar{3}c$ unit cell and this phase exhibits superionic conduction. In the compositions with low Na^+ concentration, like the phosphate end member, the Na^+ ions occupy the $6b$ crystallographic sites and as more Na^+ are incorporated in the system, the extra ions occupy the $18e$ positions. The highest conductivity is observed in the $x = 2$ composition, *i.e.* for $Na_3Zr_2Si_2PO_{12}$. It shows conductivity value of 0.67 mS/cm at room temperature and around 200 mS/cm at a higher temperature (300^o C). The conductivity value decreases on the both side of $x = 2$ and shows minimum for the end members: $NaZr_2(PO_4)_3$ and $Na_4Zr_2(SiO_4)_3$ [240, 241]. The fourth chapter of this thesis is dedicated to the computational study on this two end members employing metadynamics technique. Multiple studies have been conducted on the series and such anomalous behaviour in the conductivity trend has been proposedly attributed to the optimum ion-ion correlations, and suitable bottleneck size along the diffusion pathway of Na^+ ions. The framework structure also allows various chemical substitution through which structural properties can be tuned [102].

Many such studies with different substitution have been carried out since their inception 1976. Vogel *et al.* [242] reported a Hf substituted series, $Na_{1+x}Hf_2Si_xP_{3-x}O_{12}$ $(1.4 \leq x \leq 2.8)$, in which extrapolated room temperature conductivity reached up to 2.3 mS/cm which is higher than the Zr counterpart. Tillement *et al.* [243] investigated the effect of mixed valance (Fe^{II}/Fe^{III}) doping on the ionic conductivity in NASICON. The series, $Na_{2+x+y}Zr_{1-y}Fe^{II}{}_xFe^{III}{}_{1-x+y}(PO_4)_3$ was found to stabilize in the rhombohedral $R\bar{3}c$ symmetry for $y = 0, 0 \leq x \leq 1$ and $x + y = 1, 0 \leq y \leq 0.5$. The maximum conductivity, 4 mS/cm, was obtained for $Na_{2.3}ZrFe^{II}{}_{0.2}Fe^{III}{}_{0.3}(PO_4)_3$ at 300^o C. But the appreciable value of electronic conductivity of the material makes them suitable for electrode component. In 2016, Ma *et al.* [244] reported a Sc substituted $Na_3Zr_2Si_2PO_{12}$ series with general formula $Na_{3+x}Sc_xZr_{2-x}Si_2PO_{12}$ ($0.0 \leq x \leq 0.6$). The structure reported to be changing from monoclinic to rhombohedral as x goes from 0.0 to 0.6. The intermediate structures showed combination of monoclinic and rhombohedral phases. The highest conductivity at room temperature was obtained for the $x = 0.4$ composition, which showed a conductivity value of 4.0 mS/cm. Chen *et al.* [245] investigated influence of variety of dopant (Nb^{5+},Ti^{4+},Y^{3+},Zn^{2+}) at the octahedral Zr^{4+} position on the conductivity in $Na_3Zr_2Si_2PO_{12}$. They concluded that dopant with low valance state enables higher ionic conductivity owing to weak electrostatic interaction between the dopant and the Na^+ ions. The study showed that the highest conductivity was obtained for $Na_3Zr_{1.8}Zn_{0.2}Si_2PO_{11.8}$ ceramic which reached a value of 1.44 mS/cm at room temperature. Efforts have also been made to stabilize the high conducting phase, *i.e.* the rhombohedral phase of NASICON at room temperature. Jolley *et al.* [246] have performed a study on $Na_3Zr_2Si_2PO_{12}$ by doping different trivalent atoms such as Al, Y, Fe, divalent atoms such as Co, Ni, Zn at the octahedral Zr position and investigated the structural phase transition behaviour. They found that the Y^{3+} doping results to the lowest phase transition temperature and smallest lattice distortion. Lalère *et al.* [247] proposed an all-solid-state battery operating at 200^oC built of all-NASICON type materials where $Na_3V_2(PO_4)_3$ [248–253] was used as both of the electrodes, and $Na_3Zr_2Si_2PO_{12}$ was used as the electrolyte.

The first *full* interatomic potential for the *true*-NASICON family ($Na_{1+x}Zr_2Si_xP_{3-x}O_{12}$ was developed by Kumar and Yashonath [254, 255] and classical MD and Monte Carlo (MC) studies were carried out to investigate various structural and dynamical properties of the system across the series. This study for the first time demonstrated that the migration channel in NASICONs is the one that connect an Na1 site (6*b* sites) to six neighboring Na1 sites through the Na2 site (18*e* sites). More recently, Roy and Kumar [256, 257], showed that the Si/P ordering influences the Na^+ conductivity to a great extent owing to the differences in the strength of the electrostatic interaction between Na – Si and Na – P. In 2016, Bui *et al.* [258] carried out density functional theory (DFT) calculations and also NEB calculations to investigate the structural properties and diffusion mechanism in the low temperature ($C2/c$) phase of $Na_3Zr_2Si_2PO_{12}$. Three possible '*inner-chain*' processes and one possible 'inter-chain' process was suggested for Na^+ dynamics. The activation energies for both processes were found to be comparable and thus a combination of all the mechanism in three dimension was concluded. In 2017, Mo *et al.* [259] carried out *ab-initio* MD (AIMD) on a wide variety of superionic conductors including Na^+ conducting NASICONs and demonstrated the crucial role of 'concerted' migration in superionic conductors. It is proposed that mobile ions at higher energy sites induce such 'concerted' migration through a lower energy barrier. Later in 2019, Zhang *et al.* [260] conducted a detailed study focusing on the correlated migration mechanism in both low and high temperature phases of $Na_3Zr_2Si_2PO_{12}$ by employing AIMD. They reported a previously unknown Na5 site in the low temperature monoclinic structure. The study concluded that increasing the concentration of Na^+ ion is a more effective strategy for achieving higher ionic conductivity than to solely enhancing the cell volume. The study also experimentally verified that forcing the mobile ion species into the higher energy sites indeed helps in lowering the migration energy barrier. In another computational study, Zou *et al.* [261] revisited the rhombohedral NASICON structure and the migration mechanism in it.

Substituting Na^+ by Li^+ in the $NASICON$ framework can produce promising lithium ion conductors. The series $LiM_2(PO_4)_3$ where M = Zr, Hf, Sn, Ti or Ge is under rigorous research over at least last couple of decades [262–270]. The effect of different M ions on the conductivity and its relation to the framework flexibility in $LiM_2(PO_4)_3$, where M = Zr, Hf, Sn or Ti, has been carried out by us, and the results are presented in the third chapter of this thesis. For M = Ti, Ge systems, the structure of $LiM_2(PO_4)_3$ is known to be stabilized in the rhombohedral ($R\bar{3}c$) unit cell at room temperature whereas for higher M-ion radius, *i.e.* for Zr, Hf, Sn a lower symmetric triclinic phase ($C\bar{1}$) at room temperature has been reported in literature [267, 270–274]. The $LiTi_2(PO_4)_3$ (LTP)is one of the widely studied material in the family. The room temperature conductivity in LTP is very low for any practical application. Studies were conducted by introducing another Li-compound, such as Li_3PO_4, Li_3BO_3 etc., in the system to enhance the ionic conductivity in the system. The second compound serves as 'flux' at the grain boundaries and encourage crystallization which enables higher conductivity. For instance incorporation of 20% Li_2O in pure $LiTi_2(PO_4)_3$ improves the conductivity to 0.5 S/cm [275, 276]. Another strategy is to increase Li^+ concentration via aliovalent doping which may also alter the bottleneck sizes on the diffusion pathway. Numerous studies [277–282] have been carried out over the years by partial incorporation of trivalent ions (Ga^{3+}, Sc^{3+}, In^{3+}, Al^{3+} etc.) in the Ti^{4+} position. Among these materials, $Li_{1.3}Al_{0.3}Ti_{1.7}(PO_4)_3$ is reported to have the highest bulk conductivity (1 mS/cm) at room temperature [283]. Studies have suggested that in $Li_{1+x}Al_xTi_{2-x}(PO_4)_3$, the extra Li^+ ions occupy a new crystallographic site, called Li3 ($36f$), which is situated between two neighbouring Li1 ($6b$) sites. The diffusion channel follows Li1-Li3-Li3-Li1 connectivity [284]. Similar studies have been carried out for $LiGe_2(PO_4)_3$ system as well [285]. Despite the high conductivity value at room temperature, Ti based Li-NASICON compositions are unstable against metallic Li [286]. One of the way to overcome this issue is to introduce a stable 'barrier layer' to separate Li anode and the electrolyte [287]. In 2016, Zhao *et al.* [288] proposed a bi-layer LATP/LAGP ($Li_{1.3}Al_{0.3}Ti_{1.7}(PO_4)_3/Li_{1.3}Al_{0.3}Ge_{1.7}(PO_4)_3$) system in which the LAGP part acts like the separator. The combined system exhibited around 0.34 mS/cm ionic conductivity at 25^o C. The system was found to be showing stability against the Li anode as $LAGP$ has good stability. On the other hand, better stability has been predicted against Li anode for the $LiZr_2(PO_4)_3$ (LZP). But the triclinic structure at room temperature has a very low conductivity, [265] which together with their low affinity for doping limits applicability. El-Shinawi *et al.* [289] in 2018 introduced a new approach for synthesis of $LiZr_2(PO_4)_3$ and reported a conductivity of 0.1 mS/cm at 80^o C, and showed good compatibility with LZP electrolyte. The improvement in conductivity is attributed to the lower grain-boundary resistance. In another study, Zhang *et al.* [290] reported a series of Al^{3+} substituted LZP systems, $Li_{1+x}Al_xZr_{2-x}(PO_4)_3$ ($0.0 \leq x \leq 0.5$), which retains the high temperature rhombohedral phase at room temperature and owing to the increased number of Li^+ ions, the conductivity also reaches up to 0.0031 mS/cm for $x = 0.275$ composition. Similarly, La^{3+} substituted LZP has also been reported which retain the rhombohedral structure at room temperature [291]. Computational studies of the migration barrier in LTP and related materials have been performed by Lang *et al.* [292]. Investigation of the effect of Ca doping in LZP [293], and study of migration mechanism in LZP [294] also have been carried out in recent years.

1.2.6 $Na_2M_2TeO_6$ (M = Ni, Co, Zn or Mg)

The new class of Na based fast ion conductor, $Na_2M_2TeO_6$ where M = Ni, Co, Zn or Mg, was first reported by Evstigneeva *et al.* [295] in 2011. All four structures stabilize in the hexagonal cell with the framework made of edge sharing TeO_6 and MO_6 octahedra. The octahedral layers align perpendicular to the *c*-axis and Na^+-ions are distributed in between consecutive layers, making NaO_6 prisms. It is proposed that in the $Na_2Ni_2TeO_6$ structure, the octahedral columns along *c*-axis are arranged as Te - Te - Te - Te and M - M - M - M and the space group for this case is identified as $P6_3/mcm$. On the other hand, in the remaining cases, *i.e.* for M = Co, Mg or Zn, the octahedral columns are arranged as Te - M - Te - M and M - M - M - M and space group is $P6_322$. Three sites for Na^+ ions have been reported in the interlayer distribution, and the Na^+ diffusion happens strictly in the *ab*-plane owing to the tightly packed octahedral layers. Interatomic potentials were developed for the family and classical MD study was conducted [296, 297] which highlighted crucial atomic-scale insights. The correlated motion of Na^+ and the disorder in the Na sub-lattice were proposed as the key factors influencing the diffusion. Recently, an *ab-initio* MD study [298] on $Na_2Zn_2TeO_6$ have showed the tendency of Na^+ ions to form disordered Na sub-lattice while maintaining the primary prismatic positions. Partial doping of trivalent Ga in place of divalent Zn, resulting to $Na_{2-x}Zn_{1-x}Ga_xTeO_6$ ($0 \leq x \leq 0.15$), has shown to enhance the room temperature conductivity up to 1.1 mS/cm owing to the Na vacancy creation in the system [299]. Deng *et al.* [300] reported that incorporation of Ca in the $Na_2Zn_2TeO_6$ structure enlarge the octahedral interlayer spacing which in turn assist higher Na^+ diffusion. Further exploration related to this family is still under-way [301–303].

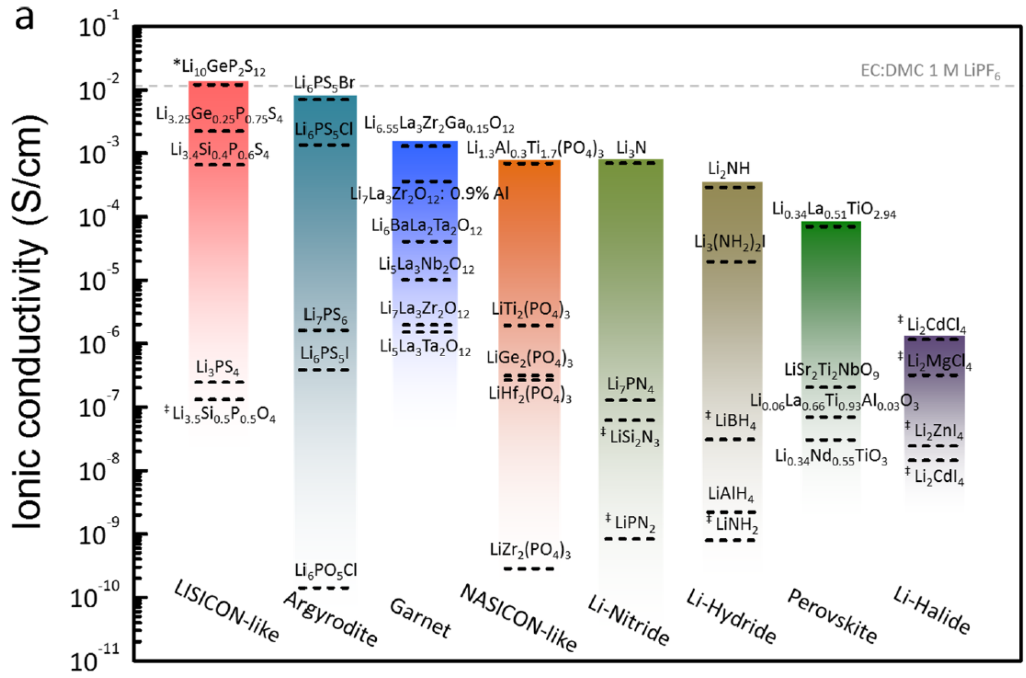

Figure 1.1: Reported room temperature conductivties of some of the promising classes of Li-ion conducting inorganic solids. Figure used with permission from ref. 96. Copyright ©2016, American Chemical Society.

1.3 Summary

The development of all-solid-state batteries, for large scale applications, such as in automobiles, and miniature electronic gadgets, remain one of the major goals before the scientific community. This is necessary for the sustainability of the environment, and for technological advancement across a multitude of areas. However replacing liquid/gel electrolytes, used in the present day battery technology, by solid electrolytes poses great technological challenges. The above account highlights several structurally diverse families of fast ion conducting solids which are promising in this pursuit. Figure 1.1 [96] provides an overview of the range of room temperature conductivity of some of the promising families of Li-ion conductors. As discussed in the previous sections, the Na- counterparts of these classes of solids are also promising in terms of their room temperature conductivities. The experimental and computational studies across these spectrum of materials have identified numerous key factors that govern ion transport in solids. Ionic conduction mechanism in solids usually occurs by means of: (a) direct hopping/vacancy diffusion in which an ion jumps to a neighbouring vacant site, (b) interstitial diffusion, in which partially occupied interstitial sites plays major role. 'Concerted migration' of the diffusing species has been found to be an important factor for diffusion in several classes of materials [259]. It has also been reported that 'bcc'-type anionic frameworks are particularly favorable for 'Li'-ion migration owing to the lower migration barrier compared to 'fcc', 'hcp' type frameworks [304].

One of the experimental strategies, exploited since long, is to make isovalent substitutions of the framework cations by larger ones, which causes an expansion of the lattice parameters, making wider migration channels. However, there are counter examples which suggest an optimal sized channel, rather than bigger channels, enhances ion mobility. Some theoretical predictions [305] and experimental observations, such as on $Li_{10}(Ge_{1-x}M_x)P_2S_{12}$ where M = Si, Sn [124], support this argument.

It has also been generally agreed upon that there is an optimal balance between the concentration of mobile species in the system and the number of available sites. The optimal composition however may vary based on the topology of the migration channel in the matrix. Typically concentration of the mobile species are tuned through aliovalent substitutions of the framework cations. This widely employed strategies have yielded several advancements across the spectrum of solids, $Li_{1+x}Al_xTi_{2-x}(PO_4)_3$ ($x = 0.3$), $Na_{1+x}Zr_2Si_xP_{3-x}O_{12}$ ($x = 2$), $Na_{3+x}M_x^{4+}P_{1-x}S_4$ (M = Ge or Sn, and x = 0.0625 and M

= Si; x = 0.0625, 0.125) , to name a few typical examples. Studies have also shown that the ordering of the framework cations, such as Si/P ordering in the NASICON framework, plays a crucial role on determining ion transport in solids [256, 257, 306–309]. Another aspect closely related to the ion concentration is the ion-ion correlations. Many computational studies, such as that of $Na_2Ni_2TeO_6$, suggest that an optimal correlation between ions thermodynamically favours higher disorder of the mobile ion sub-lattice, resulting in enhanced ion transport [297]. Proposedly, one of the reasons for the high conductivity of $Na_3Zr_2Si_2P_{12}$ has also been attributed to this effect [241, 310]. In Chapter 3 of this thesis we present theoretical evidence that ion hops are indeed correlated with the framework motion. Recent studies are exploring to improve the ion transport through softening of the frameworks. This has attracted fresh attention on chalcogenide systems, and resulted the discovery of materials such as thio-phosphates [117, 311]. Studies have also suggested that in some systems such softening lead to decrease in the Arrhenius pre-factor and thus making the effect of softer lattice on diffusion ambiguous, at least in some cases [172, 173].

Thus several factors that influence ion transport in solids have been recognized, and efforts are on to combine and optimize these, often competing, aspects to achieve better ionic conductivity. Further, apart from achieving high ionic conductivity several other aspects related to the stability and compatibility at the electrode/electrolyte interfaces also need be addressed to realize commercially viable all-solid-state batteries.

1.4 Objective of the thesis

From the above review on fast ion conducting solids it is evident that further advancement in this direction calls for concerted efforts wherein experimental, theoretical and computational approach compliment each other. Atomistic computer simulation techniques such as molecular dynamics (MD) is an extremely powerful tool to investigate materials properties at atomic length and time scales. In the study of ion conduction, these techniques have been successfully used over the last three decade [312–315], as highlighted in the previous sections. These studies have provided many important microscopic insights related to ion transport in solids, such as the migration channels, microscopic energetics, mechanism of ion mobility, etc. These insights are important in the tailor making of materials for solid state batteries. The thesis presents simulation studies on some of the promising Li^+ and Na^+ conducting inorganic solid electrolytes.

The remaining chapters of the thesis are organized as follows,

- Chapter 2 discusses the theoretical foundations of the computational techniques employed in the study.
- In Chapter 3 investigation of the role of framework flexibility on ion transport mechanism in $LiM_2(PO_4)_3$, where M = Zr, Hf, Sn or Ti, and the correlation between the bottleneck size and ion dynamics have been discussed.
- Chapter 4 discusses utility of the metadynamics technique in exploring slow diffusion in solids, where in the time-scale of standard molecular dynamics (MD) is inadequate. The implementation of the technique is demonstrated for the two end members of the NASICON family, namely $NaZr_2(PO_4)_3$ and $Na_4Zr_2(SiO_4)_3$.
- Chapter 5 discusses the Li^+-ion diffusion mechanism in γ-Li_3PS_4 by incorporating metadynamics technique within *ab-initio*-MD. The diffusion channels and mechanism of Li^+ transport are explored. The underlying microscopic energy barriers, are estimated both from metadynamics as well as from nudged elastic band method.
- Chapter 6 summarizes the findings of the study, with an outlook to future directions.

BIBLIOGRAPHY

[1] W. M. Sudduth, *Ambix*, 1980, **27**, 26–35.

[2] B. Scrosati, *Journal of solid state electrochemistry*, 2011, **15**, 1623–1630.

[3] A. Boulabiar, K. Bouraoui, M. Chastrette and M. Abderrabba, *J. Chem. Educ.*, 2004, **81**, 754.

[4] G. F. Martins, *J. Chem. Educ.*, 1990, **67**, 482.

[5] R. Boddula, R. Pothu, A. M. Asiri *et al.*, *Rechargeable Batteries: History, Progress, and Applications*, John Wiley & Sons, 2020.

[6] J. Jung, L. Zhang and J. Zhang, *Lead-acid battery technologies: fundamentals, materials, and applications*, Crc Press, 2015, vol. 8.

[7] P. T. Moseley and J. Garche, *Electrochemical energy storage for renewable sources and grid balancing*, Newnes, 2014.

[8] M. Yoshio, R. J. Brodd and A. Kozawa, *Lithium-ion batteries*, Springer, 2009, vol. 1.

[9] J. B. Goodenough and K.-S. Park, *J. Am. Chem. Soc*, 2013, **135**, 1167–1176.

[10] M. Balaish, A. Kraytsberg and Y. Ein-Eli, *Phys. Chem. Chem. Phys.*, 2014, **16**, 2801–2822.

[11] M. A. Rahman, X. Wang and C. Wen, *J. Appl. Electrochem.*, 2014, **44**, 5–22.

[12] Z. Ma, X. Yuan, L. Li, Z.-F. Ma, D. P. Wilkinson, L. Zhang and J. Zhang, *Energy Environ. Sci.*, 2015, **8**, 2144–2198.

[13] B. Kumar, J. Kumar, R. Leese, J. P. Fellner, S. J. Rodrigues and K. Abraham, *J. Electrochem. Soc*, 2009, **157**, A50.

[14] J. Scheers, S. Fantini and P. Johansson, *J. Power Sources*, 2014, **255**, 204–218.

[15] R. Chen, T. Zhao and F. Wu, *ChemComm*, 2015, **51**, 18–33.

[16] X. Gu and C. Lai, *Journal of Materials Research*, 2018, **33**, 16–31.

[17] X. Su, Q. Wu, J. Li, X. Xiao, A. Lott, W. Lu, B. W. Sheldon and J. Wu, *Adv. Energy Mater.*, 2014, **4**, 1300882.

[18] X. Zuo, J. Zhu, P. Müller-Buschbaum and Y.-J. Cheng, *Nano Energy*, 2017, **31**, 113–143.

[19] M. Ge, X. Fang, J. Rong and C. Zhou, *Nanotechnology*, 2013, **24**, 422001.

[20] G.-A. Nazri and G. Pistoia, *Lithium batteries: science and technology*, Springer Science & Business Media, 2008.

[21] C. R. A. Catlow, *J. Chem. Soc. Faraday Trans*, 1990, **86**, 1167–1176.

[22] H. L. Tuller and P. K. Moon, *Mat. Sci. Eng. B-Adv*, 1988, **1**, 171–191.

[23] H. Schulz, *Annu. Rev. Mater. Sci.*, 1982, **12**, 351–376.

[24] W. Gool, *Annu. Rev. Mater. Sci.*, 1974, **4**, 311–335.

[25] A. D. Sendek, Q. Yang, E. D. Cubuk, K.-A. N. Duerloo, Y. Cui and E. J. Reed, *Energy Environ. Sci.*,

2017, **10**, 306–320.

[26] T. Takahashi, S. Ikeda and O. Yamamoto, *J. Electrochem. Soc*, 1972, **119**, 477.

[27] T. Takahashi, S. Ikeda and O. Yamamoto, *J. Electrochem. Soc*, 1973, **120**, 647.

[28] H.-P. Hong, *Mater. Res. Bull.*, 1976, **11**, 173–182.

[29] J. B. Goodenough, H.-P. Hong and J. Kafalas, *Mater. Res. Bull.*, 1976, **11**, 203–220.

[30] C. Cao, Z.-B. Li, X.-L. Wang, X.-B. Zhao and W.-Q. Han, *Front. Energy Res.*, 2014, **2**, 25.

[31] X. Chen and P. M. Vereecken, *Adv. Mater. Interfaces*, 2019, **6**, 1800899.

[32] X.-B. Cheng, R. Zhang, C.-Z. Zhao, F. Wei, J.-G. Zhang and Q. Zhang, *Adv. Sci.*, 2016, **3**, 1500213.

[33] T. Liu, X. Zhang, X. Wang, J. Yu and L. Li, *Ionics*, 2016, **22**, 2249–2262.

[34] N. Mahato, A. Banerjee, A. Gupta, S. Omar and K. Balani, *Prog. Mater. Sci*, 2015, **72**, 141–337.

[35] M. Á. Muñoz-Márquez, D. Saurel, J. L. Gómez-Cámer, M. Casas-Cabanas, E. Castillo-Martínez and T. Rojo, *Adv. Energy Mater.*, 2017, **7**, 1700463.

[36] Y.-Z. Sun, J.-Q. Huang, C.-Z. Zhao and Q. Zhang, *Sci. China Chem.*, 2017, **60**, 1508–1526.

[37] M. Tatsumisago, M. Nagao and A. Hayashi, *J. Asian Ceram. Soc.*, 2013, **1**, 17–25.

[38] P. Verma, P. Maire and P. Novák, *Electrochimica. Acta.*, 2010, **55**, 6332–6341.

[39] A. Wang, S. Kadam, H. Li, S. Shi and Y. Qi, *Npj Comput. Mater.*, 2018, **4**, 1–26.

[40] X. Yao, B. Huang, J. Yin, G. Peng, Z. Huang, C. Gao, D. Liu and X. Xu, *Chin. Phys. B*, 2015, **25**, 018802.

[41] X. Yu and A. Manthiram, *Acc. Chem. Res.*, 2017, **50**, 2653–2660.

[42] S. S. Zhang, *J. Power Sources*, 2006, **162**, 1379–1394.

[43] B. Zhang, R. Tan, L. Yang, J. Zheng, K. Zhang, S. Mo, Z. Lin and F. Pan, *Energy Stor. Mater.*, 2018, **10**, 139–159.

[44] C.-Z. Zhao, B.-C. Zhao, C. Yan, X.-Q. Zhang, J.-Q. Huang, Y. Mo, X. Xu, H. Li and Q. Zhang, *Energy Stor. Mater.*, 2020, **24**, 75–84.

[45] F. Zheng, M. Kotobuki, S. Song, M. O. Lai and L. Lu, *J. Power Sources*, 2018, **389**, 198–213.

[46] R. Agrawal and G. Pandey, *J. Phys. D: Appl. Phys*, 2008, **41**, 223001.

[47] C. Zhao, L. Liu, X. Qi, Y. Lu, F. Wu, J. Zhao, Y. Yu, Y.-S. Hu and L. Chen, *Adv. Energy Mater.*, 2018, **8**, 1703012.

[48] Y. Zhao, K. Zheng and X. Sun, *Joule*, 2018, **2**, 2583–2604.

[49] J. B. Goodenough, *Annu. Rev. Mater. Res.*, 2003, **33**, 91–128.

[50] L. Malavasi, C. A. Fisher and M. S. Islam, *Chem. Soc. Rev*, 2010, **39**, 4370–4387.

[51] D. J. Brett, A. Atkinson, N. P. Brandon and S. J. Skinner, *Chem. Soc. Rev*, 2008, **37**, 1568–1578.

[52] A. Orera and P. Slater, *Chem. Mater*, 2010, **22**, 675–690.

[53] P. Knauth and H. L. Tuller, *J. Am. Ceram. Soc*, 2002, **85**, 1654–1680.

[54] S. Hossain, A. M. Abdalla, S. N. B. Jamain, J. H. Zaini and A. K. Azad, *Renew. Sustain. Energy Rev*, 2017, **79**, 750–764.

[55] E. Fabbri, D. Pergolesi and E. Traversa, *Chem. Soc. Rev*, 2010, **39**, 4355–4369.

[56] R. Reijers and W. Haije, *Energy research Centre of the Netherlands*, 2008, **8**, year.

[57] N. Sorokin and B. Sobolev, *Crystallogr. Rep.*, 2007, **52**, 842–863.

[58] F. Gschwind, G. Rodriguez-Garcia, D. Sandbeck, A. Gross, M. Weil, M. Fichtner and N. Hörmann, *J.*

Fluor. Chem, 2016, **182**, 76–90.

[59] L. Patro and K. Hariharan, *Solid State Ionics*, 2013, **239**, 41–49.

[60] J. B. Goodenough, *Proc. R. Soc. Lond*, 1984, **393**, 215–234.

[61] W. Kuhs, R. Nitsche and K. Scheunemann, *Mater. Res. Bull*, 1979, **14**, 241–248.

[62] M. Kobayashi, *Solid State Ionics*, 1990, **39**, 121–149.

[63] T. Takahashi, *J. Appl. Electrochem.*, 1973, **3**, 79–90.

[64] K. Shahi, *Phys. Status Solidi (a)*, 1977, **41**, 11–44.

[65] M. Yashima, *J. Ceram. Soc. Jpn.*, 2009, **117**, 1055–1059.

[66] J. Gao, Y.-S. Zhao, S.-Q. Shi and H. Li, *Chin. Phys. B*, 2015, **25**, 018211.

[67] P. Knauth, *Solid State Ionics*, 2009, **180**, 911–916.

[68] C. Tubandt and E. Lorenz, *Z. Phys. Chem.*, 1914, **87**, 513–542.

[69] K. Funke, *Prog. Solid. State Ch.*, 1976, **11**, 345–402.

[70] J. Boyce, T. Hayes, W. Stutius and J. Mikkelsen Jr, *Phys. Rev. Lett.*, 1977, **38**, 1362.

[71] R. Cava, F. Reidinger and B. Wuensch, *Solid State Commun.*, 1977, **24**, 411–416.

[72] A. Wright and B. Fender, *J. Phys. C: Solid State*, 1977, **10**, 2261.

[73] P. Vashishta and A. Rahman, *Phys. Rev. Lett.*, 1978, **40**, 1337.

[74] M. Parrinello, A. Rahman and P. Vashishta, *Phys. Rev. Lett.*, 1983, **50**, 1073.

[75] S.-r. Sun and D.-g. Xia, *Solid State Ionics*, 2008, **179**, 2330–2334.

[76] T. Takahashi and O. Yamamoto, *Denki Kagaku,(Tokyo)*, 1964, **32**, 610–615.

[77] B. B. Owens and G. R. Argue, *Science*, 1967, **157**, 308–310.

[78] S. Geller, *Science*, 1967, **157**, 310–312.

[79] N. Valverde, *J. Electrochem. Soc*, 1980, **127**, 2425.

[80] G. Burns, F. Dacol and M. Shafer, *Solid State Commun.*, 1976, **19**, 287–290.

[81] W. Johnston, H. Wiedersich and G. Lindberg, *J. Chem. Phys*, 1969, **51**, 3739–3747.

[82] R. Biefeld, R. Johnson Jr and M. Karnowsky, *J. Electrochem. Soc*, 1979, **126**, 818.

[83] K. Shahi and J. Wagner Jr, *Phys. Rev. B*, 1981, **23**, 6417.

[84] J. Bazán and J. Schmidt, *J. Appl. Electrochem.*, 1976, **6**, 411–415.

[85] A. Ivanov-Shitz, B. Y. Mazniker and E. Povolotskaya, *Crystallogr. Rep.*, 2002, **47**, 117–119.

[86] M. Kobayashi, K. Ishikawa, F. Tachibana and H. Okazaki, *Phys. Rev. B*, 1988, **38**, 3050.

[87] M. Kobayashi, T. Tomari, F. Tachibana and H. Okazaki, *Phys. Rev. B*, 1989, **40**, 9552.

[88] F. Tachibana, M. Kobayashi and H. Okazaki, *Solid State Ionics*, 1988, **28**, 41–45.

[89] J. R. Ray and P. Vashishta, *J. Chem. Phys*, 1989, **90**, 6580–6586.

[90] I. Ebbsjo, P. Vashishta, R. Dejus and K. Skold, *J. Phys. C: Solid State*, 1987, **20**, L441.

[91] S. Fiechter and E. Gmelin, *Thermochimica acta*, 1985, **87**, 319–334.

[92] H. Wada and M. Onoda, *J. Less Common Met.*, 1991, **175**, 209–217.

[93] H. Wada, *J. Alloys Compd*, 1992, **178**, 315–323.

[94] H. Wada, M. Ishii, M. Onoda, M. Tansho and A. Sato, *Solid state ionics*, 1996, **86**, 159–163.

[95] H. Wada, A. Sato, M. Onoda, S. Adams, M. Tansho and M. Ishii, *Solid state ionics*, 2002, **154**, 723–727.

[96] J. C. Bachman, S. Muy, A. Grimaud, H.-H. Chang, N. Pour, S. F. Lux, O. Paschos, F. Maglia, S. Lupart,

P. Lamp *et al.*, *Chem. Rev.*, 2016, **116**, 140–162.

[97] T. Famprikis, P. Canepa, J. A. Dawson, M. S. Islam and C. Masquelier, *Nat. Mater.*, 2019, 1–14.

[98] W. Liu, X. Sun, H. Wang and X. Cao, *Front. Energy Res.*, 2019, **7**, 112.

[99] Z. Zhang, Y. Shao, B. Lotsch, Y.-S. Hu, H. Li, J. Janek, L. F. Nazar, C.-W. Nan, J. Maier, M. Armand *et al.*, *Energy Environ. Sci.*, 2018, **11**, 1945–1976.

[100] W. Zhao, J. Yi, P. He and H. Zhou, *Electrochem. Energ. Rev.*, 2019, 1–32.

[101] V. Palomares, P. Serras, I. Villaluenga, K. B. Hueso, J. Carretero-González and T. Rojo, *Energy Environ. Sci.*, 2012, **5**, 5884–5901.

[102] N. Anantharamulu, K. K. Rao, G. Rambabu, B. V. Kumar, V. Radha and M. Vithal, *J. Mater. Sci.*, 2011, **46**, 2821–2837.

[103] M. D. Slater, D. Kim, E. Lee and C. S. Johnson, *Adv. Funct. Mater*, 2013, **23**, 947–958.

[104] B. L. Ellis and L. F. Nazar, *Curr. Opin. Solid. State Mater. Sci.*, 2012, **16**, 168–177.

[105] H.-P. Hong, *Mater. Res. Bull*, 1978, **13**, 117–124.

[106] U. Alpen, M. Bell, W. Wichelhaus, K. Cheung and G. Dudley, *Electrochimica Acta*, 1978, **23**, 1395–1397.

[107] J. Bates, N. Dudney, G. Gruzalski, R. Zuhr, A. Choudhury, C. Luck and J. Robertson, *Solid state ionics*, 1992, **53**, 647–654.

[108] J. Bates, N. Dudney, G. Gruzalski, R. Zuhr, A. Choudhury, C. Luck and J. Robertson, *J. Power Sources*, 1993, **43**, 103–110.

[109] Y. A. Du and N. Holzwarth, *J. Electrochem. Soc*, 2007, **154**, A999.

[110] Y. A. Du and N. Holzwarth, *Phys. Rev. B*, 2007, **76**, 174302.

[111] B. Wang, B. Chakoumakos, B. Sales, B. Kwak and J. Bates, *J. Solid State Chem.*, 1995, **115**, 313–323.

[112] X. Yu, J. Bates, G. Jellison Jr and F. Hart, *J. Electrochem. Soc*, 1997, **144**, 524.

[113] Y.-W. Hu, I. Raistrick and R. A. Huggins, *J. Electrochem. Soc*, 1977, **124**, 1240.

[114] N. Lepley, N. Holzwarth and Y. A. Du, *Phys. Rev. B*, 2013, **88**, 104103.

[115] A. Al-Qawasmeh and N. Holzwarth, 2017.

[116] R. Shannon, B. Taylor, A. English and T. Berzins, International Symposium on Solid Ionic and Ionic-Electronic Conductors, 1977, pp. 783–796.

[117] M. Murayama, R. Kanno, M. Irie, S. Ito, T. Hata, N. Sonoyama and Y. Kawamoto, *J. Solid State Chem.*, 2002, **168**, 140–148.

[118] N. Kamaya, K. Homma, Y. Yamakawa, M. Hirayama, R. Kanno, M. Yonemura, T. Kamiyama, Y. Kato, S. Hama, K. Kawamoto *et al.*, *Nat. Mater.*, 2011, **10**, 682–686.

[119] Y. Mo, S. P. Ong and G. Ceder, *Chem. Mater*, 2012, **24**, 15–17.

[120] C. Hu, Z. Wang, Z. Sun and C. Ouyang, *Chem. Phys. Lett*, 2014, **591**, 16–20.

[121] S. Adams and R. P. Rao, *J. Mater. Chem.*, 2012, **22**, 7687–7691.

[122] S. P. Ong, Y. Mo, W. D. Richards, L. Miara, H. S. Lee and G. Ceder, *Energy Environ. Sci.*, 2013, **6**, 148–156.

[123] P. Bron, S. Johansson, K. Zick, J. Schmedt auf der Gunne, S. Dehnen and B. Roling, *J. Am. Chem. Soc*, 2013, **135**, 15694–15697.

[124] Y. Kato, R. Saito, M. Sakano, A. Mitsui, M. Hirayama and R. Kanno, *J. Power Sources*, 2014, **271**,

60–64.

[125] A. Kuhn, O. Gerbig, C. Zhu, F. Falkenberg, J. Maier and B. V. Lotsch, *Phys. Chem. Chem. Phys.*, 2014, **16**, 14669–14674.

[126] Y. Kato, S. Hori, T. Saito, K. Suzuki, M. Hirayama, A. Mitsui, M. Yonemura, H. Iba and R. Kanno, *Nat. Energy.*, 2016, **1**, 1–7.

[127] S. J. Sedlmaier, S. Indris, C. Dietrich, M. Yavuz, C. Drager, F. von Seggern, H. Sommer and J. Janek, *Chem. Mater*, 2017, **29**, 1830–1835.

[128] W. D. Richards, Y. Wang, L. J. Miara, J. C. Kim and G. Ceder, *Energy Environ. Sci.*, 2016, **9**, 3272–3278.

[129] K. Kaup, F. Lalere, A. Huq, A. Shyamsunder, T. Adermann, P. Hartmann and L. F. Nazar, *Chem. Mater*, 2018, **30**, 592–596.

[130] K. Homma, M. Yonemura, T. Kobayashi, M. Nagao, M. Hirayama and R. Kanno, *Solid State Ionics*, 2011, **182**, 53–58.

[131] Ö. U. Kudu, T. Famprikis, B. Fleutot, M.-D. Braida, T. Le Mercier, M. S. Islam and C. Masquelier, *J. Power Sources*, 2018, **407**, 31–43.

[132] Y. Seino, T. Ota, K. Takada, A. Hayashi and M. Tatsumisago, *Energy Environ. Sci.*, 2014, **7**, 627–631.

[133] M. R. Busche, D. A. Weber, Y. Schneider, C. Dietrich, S. Wenzel, T. Leichtweiss, D. Schroder, W. Zhang, H. Weigand, D. Walter *et al.*, *Chem. Mater*, 2016, **28**, 6152–6165.

[134] I.-H. Chu, H. Nguyen, S. Hy, Y.-C. Lin, Z. Wang, Z. Xu, Z. Deng, Y. S. Meng and S. P. Ong, *ACS Appl. Mater. Interfaces*, 2016, **8**, 7843–7853.

[135] K. Homma, M. Yonemura, M. Nagao, M. Hirayama and R. Kanno, *J. Phys. Soc. Jpn*, 2010, **79**, 90–93.

[136] J.-S. Kim, W. D. Jung, S. Choi, J.-W. Son, B.-K. Kim, J.-H. Lee and H. Kim, *J. Phys. Chem. Lett*, 2018, **9**, 5592–5597.

[137] M. Jansen and U. Henseler, *J. Solid State Chem.*, 1992, **99**, 110–119.

[138] A. Hooper, P. McGeehin, K. Harrison and B. Tofield, *J. Solid State Chem.*, 1978, **24**, 265–275.

[139] S. Milne and A. West, *Mater. Res. Bull*, 1984, **19**, 705–710.

[140] A. Hayashi, K. Noi, A. Sakuda and M. Tatsumisago, *Nat. Commun.*, 2012, **3**, 1–5.

[141] A. Hayashi, K. Noi, N. Tanibata, M. Nagao and M. Tatsumisago, *J. Power Sources*, 2014, **258**, 420–423.

[142] T. Krauskopf, S. P. Culver and W. G. Zeier, *Inorg. Chem*, 2018, **57**, 4739–4744.

[143] N. Tanibata, K. Noi, A. Hayashi and M. Tatsumisago, *RSC Adv.*, 2014, **4**, 17120–17123.

[144] N. Tanibata, K. Noi, A. Hayashi, N. Kitamura, Y. Idemoto and M. Tatsumisago, *ChemElectroChem*, 2014, **1**, 1130–1132.

[145] L. Zhang, K. Yang, J. Mi, L. Lu, L. Zhao, L. Wang, Y. Li and H. Zeng, *Adv. Energy Mater.*, 2015, **5**, 1501294.

[146] T. Krauskopf, C. Pompe, M. A. Kraft and W. G. Zeier, *Chem. Mater*, 2017, **29**, 8859–8869.

[147] A. Banerjee, K. H. Park, J. W. Heo, Y. J. Nam, C. K. Moon, S. M. Oh, S.-T. Hong and Y. S. Jung, *Angew. Chem*, 2016, **128**, 9786–9790.

[148] H. Wang, Y. Chen, Z. D. Hood, G. Sahu, A. S. Pandian, J. K. Keum, K. An and C. Liang, *Angew. Chem*, 2016, **128**, 8693–8697.

[149] L. Zhang, D. Zhang, K. Yang, X. Yan, L. Wang, J. Mi, B. Xu and Y. Li, *Adv. Sci.*, 2016, **3**, 1600089.

[150] Y. Hibi, N. Tanibata, A. Hayashi and M. Tatsumisago, *Solid State Ionics*, 2015, **270**, 6–9.

[151] I.-H. Chu, C. S. Kompella, H. Nguyen, Z. Zhu, S. Hy, Z. Deng, Y. S. Meng and S. P. Ong, *Sci. Rep*, 2016, **6**, 33733.

[152] H. Huang, H.-H. Wu, X. Wang, B. Huang and T.-Y. Zhang, *Phys. Chem. Chem. Phys.*, 2018, **20**, 20525–20533.

[153] C. K. Moon, H.-J. Lee, K. H. Park, H. Kwak, J. W. Heo, K. Choi, H. Yang, M.-S. Kim, S.-T. Hong, J. H. Lee *et al.*, *ACS Energy Lett.*, 2018, **3**, 2504–2512.

[154] N. Wang, K. Yang, L. Zhang, X. Yan, L. Wang and B. Xu, *J. Mater. Sci.*, 2018, **53**, 1987–1994.

[155] J. W. Heo, A. Banerjee, K. H. Park, Y. S. Jung and S.-T. Hong, *Adv. Energy Mater.*, 2018, **8**, 1702716.

[156] Z. Zhu, I.-H. Chu, Z. Deng and S. P. Ong, *Chem. Mater*, 2015, **27**, 8318–8325.

[157] N. J. de Klerk and M. Wagemaker, *Chem. Mater*, 2016, **28**, 3122–3130.

[158] T. Famprikis, J. A. Dawson, F. Fauth, O. Clemens, E. Suard, B. Fleutot, M. Courty, J.-N. Chotard, M. S. Islam and C. Masquelier, *ACS Mater. Lett.*, 2019, **1**, 641–646.

[159] V. S. Kandagal, M. D. Bharadwaj and U. V. Waghmare, *J. Mater. Chem. A*, 2015, **3**, 12992–12999.

[160] F. Tsuji, N. Tanibata, A. Sakuda, A. Hayashi and M. Tatsumisago, *Chem. Lett*, 2018, **47**, 13–15.

[161] M. Duchardt, U. Ruschewitz, S. Adams, S. Dehnen and B. Roling, *Angew. Chem International Edition*, 2018, **57**, 1351–1355.

[162] Z. Zhu, *PhD thesis*, UC San Diego, 2019.

[163] K. Oh, D. Chang, I. Park, K. Yoon and K. Kang, *Chem. Mater*, 2019, **31**, 6066–6075.

[164] Y. Wang, W. D. Richards, S.-H. Bo, L. J. Miara and G. Ceder, *Chem. Mater*, 2017, **29**, 7475–7482.

[165] A. Hayashi, N. Masuzawa, S. Yubuchi, F. Tsuji, C. Hotehama, A. Sakuda and M. Tatsumisago, *Nat. Commun.*, 2019, **10**, 1–6.

[166] H.-J. Deiseroth, S.-T. Kong, H. Eckert, J. Vannahme, C. Reiner, T. Zaiß and M. Schlosser, *Angew. Chem*, 2008, **120**, 767–770.

[167] I. Hanghofer, M. Brinek, S. Eisbacher, B. Bitschnau, M. Volck, V. Hennige, I. Hanzu, D. Rettenwander and H. Wilkening, *Phys. Chem. Chem. Phys.*, 2019, **21**, 8489–8507.

[168] R. P. Rao, N. Sharma, V. Peterson and S. Adams, *Solid State Ionics*, 2013, **230**, 72–76.

[169] C. Yu, S. Ganapathy, J. Hageman, L. van Eijck, E. R. Van Eck, L. Zhang, T. Schwietert, S. Basak, E. M. Kelder and M. Wagemaker, *ACS Appl. Mater. Interfaces*, 2018, **10**, 33296–33306.

[170] S. T. Kong, Ö. Gün, B. Koch, H. J. Deiseroth, H. Eckert and C. Reiner, *Chem. Eur. J*, 2010, **16**, 5138–5147.

[171] P. Adeli, J. D. Bazak, K. H. Park, I. Kochetkov, A. Huq, G. R. Goward and L. F. Nazar, *Angew. Chem International Edition*, 2019, **58**, 8681–8686.

[172] T. Bernges, S. P. Culver, N. Minafra, R. Koerver and W. G. Zeier, *Inorg. Chem*, 2018, **57**, 13920–13928.

[173] M. A. Kraft, S. P. Culver, M. Calderon, F. Bocher, T. Krauskopf, A. Senyshyn, C. Dietrich, A. Zevalkink, J. Janek and W. G. Zeier, *J. Am. Chem. Soc*, 2017, **139**, 10909–10918.

[174] N. Minafra, S. P. Culver, T. Krauskopf, A. Senyshyn and W. G. Zeier, *J. Mater. Chem. A*, 2018, **6**, 645–651.

[175] W. D. Jung, J.-S. Kim, S. Choi, S. Kim, M. Jeon, H.-G. Jung, K. Y. Chung, J.-H. Lee, B.-K. Kim, J.-H.

Lee *et al.*, *Nano Lett.*, 2020, **20**, 2303–2309.

[176] X. Feng, P.-H. Chien, Y. Wang, S. Patel, P. Wang, H. Liu, M. Immediato-Scuotto and Y.-Y. Hu, *Energy Stor. Mater.*, 2020.

[177] B. Ouyang, Y. Wang, Y. Sun and G. Ceder, *Chem. Mater*, 2020, **32**, 1896–1903.

[178] V. Thangadurai, H. Kaack and W. J. Weppner, *J. Am. Ceram. Soc*, 2003, **86**, 437–440.

[179] F. Abbattista, M. Vallino and D. Mazza, *Mater. Res. Bull*, 1987, **22**, 1019–1027.

[180] D. Mazza, *Mater. Lett*, 1988, **7**, 205–207.

[181] H. Hyooma and K. Hayashi, *Mater. Res. Bull*, 1988, **23**, 1399–1407.

[182] V. Thangadurai, S. Narayanan and D. Pinzaru, *Chem. Soc. Rev*, 2014, **43**, 4714–4727.

[183] E. J. Cussen, *ChemComm*, 2006, 412–413.

[184] E. J. Cussen, *J. Mater. Chem.*, 2010, **20**, 5167–5173.

[185] M. P. O'Callaghan, D. R. Lynham, E. J. Cussen and G. Z. Chen, *Chem. Mater*, 2006, **18**, 4681–4689.

[186] M. P. O'Callaghan, A. S. Powell, J. J. Titman, G. Z. Chen and E. J. Cussen, *Chem. Mater*, 2008, **20**, 2360–2369.

[187] V. Thangadurai and W. Weppner, *J. Am. Ceram. Soc*, 2005, **88**, 411–418.

[188] V. Thangadurai and W. Weppner, *Adv. Funct. Mater*, 2005, **15**, 107–112.

[189] R. Murugan, V. Thangadurai and W. Weppner, *J. Electrochem. Soc*, 2007, **155**, A90.

[190] H. Xie, Y. Li, J. Han, Y. Dong, M. P. Paranthaman, L. Wang, M. Xu, A. Gupta, Z. Bi, C. A. Bridges *et al.*, *J. Electrochem. Soc*, 2012, **159**, A1148.

[191] R. Murugan, V. Thangadurai and W. Weppner, *Angew. Chem International Edition*, 2007, **46**, 7778–7781.

[192] C. A. Geiger, E. Alekseev, B. Lazic, M. Fisch, T. Armbruster, R. Langner, M. Fechtelkord, N. Kim, T. Pettke and W. Weppner, *Inorg. Chem*, 2011, **50**, 1089–1097.

[193] J. Awaka, N. Kijima, H. Hayakawa and J. Akimoto, *J. Solid State Chem.*, 2009, **182**, 2046–2052.

[194] J. Awaka, N. Kijima, K. Kataoka, H. Hayakawa, K.-i. Ohshima and J. Akimoto, *J. Solid State Chem.*, 2010, **183**, 180–185.

[195] J. Percival, E. Kendrick, R. Smith and P. Slater, *Dalton Trans.*, 2009, 5177–5181.

[196] C. Bernuy-Lopez, W. Manalastas Jr, J. M. Lopez del Amo, A. Aguadero, F. Aguesse and J. A. Kilner, *Chem. Mater*, 2014, **26**, 3610–3617.

[197] Y. Li, J.-T. Han, C.-A. Wang, H. Xie and J. B. Goodenough, *J. Mater. Chem.*, 2012, **22**, 15357–15361.

[198] C. Deviannapoorani, L. Dhivya, S. Ramakumar and R. Murugan, *J. Power Sources*, 2013, **240**, 18–25.

[199] Y. Wang, A. Huq and W. Lai, *Solid state ionics*, 2014, **255**, 39–49.

[200] R. Jalem, M. Nakayama, W. Manalastas Jr, J. A. Kilner, R. W. Grimes, T. Kasuga and K. Kanamura, *J. Phys. Chem. C*, 2015, **119**, 20783–20791.

[201] B. Andriyevsky, K. Doll and T. Jacob, *Mater. Chem. Phys*, 2017, **185**, 210–217.

[202] S. G. Kang and D. S. Sholl, *J. Phys. Chem. C*, 2014, **118**, 17402–17406.

[203] K. Santosh, R. C. Longo, K. Xiong and K. Cho, *Solid State Ionics*, 2014, **261**, 100–105.

[204] R. Jalem, Y. Yamamoto, H. Shiiba, M. Nakayama, H. Munakata, T. Kasuga and K. Kanamura, *Chem. Mater*, 2013, **25**, 425–430.

[205] M. Burbano, D. Carlier, F. Boucher, B. J. Morgan and M. Salanne, *Phys. Rev. Lett.*, 2016, **116**, 135901.

[206] V. Thangadurai, S. Adams and W. Weppner, *Chem. Mater*, 2004, **16**, 2998–3006.

[207] M. Xu, M. S. Park, J. M. Lee, T. Y. Kim, Y. S. Park and E. Ma, *Phys. Rev. B*, 2012, **85**, 052301.

[208] A. Chroneos, R. Vovk, I. Goulatis and L. Goulatis, *J. Alloys Compd.*, 2010, **494**, 190–195.

[209] M. Asghar, J. Zhang, H. Wang and P. Lund, *Renew. Sustain. Energy Rev*, 2017, **77**, 131–146.

[210] M. Konstantakou and T. Stergiopoulos, *J. Mater. Chem. A*, 2017, **5**, 11518–11549.

[211] H. U. Anderson, *Solid State Ionics*, 1992, **52**, 33–41.

[212] S. P. Jiang, *J. Mater. Sci.*, 2008, **43**, 6799–6833.

[213] Y. Sun, P. Guan, Y. Liu, H. Xu, S. Li and D. Chu, *Critical Reviews in Solid State and Materials Sciences*, 2019, **44**, 265–282.

[214] G.-y. Adachi, N. Imanaka and S. Tamura, *Chem. Rev.*, 2002, **102**, 2405–2430.

[215] L. Latie, G. Villeneuve, D. Conte and G. Le Flem, *J. Solid State Chem.*, 1984, **51**, 293–299.

[216] Y. Inaguma, Y. Matsui, Y.-J. Shan, M. Itoh and T. Nakamura, *Solid State Ionics*, 1995, **79**, 91–97.

[217] Y. INAGUMA, Y. MATSUI, J. YU, Y.-J. SHAN, T. NAKAMURA and M. ITOH, *J. Phys. Chem. Solids*, 1997, **58**, 843–852.

[218] Y. Inaguma, C. Liquan, M. Itoh, T. Nakamura, T. Uchida, H. Ikuta and M. Wakihara, *Solid State Commun.*, 1993, **86**, 689–693.

[219] M. Abe and K. Uchino, *Mater. Res. Bull*, 1974, **9**, 147–155.

[220] Y. Inaguma, T. Katsumata, M. Itoh and Y. Morii, *J. Solid State Chem.*, 2002, **166**, 67–72.

[221] M. Yashima, M. Itoh, Y. Inaguma and Y. Morii, *J. Am. Chem. Soc*, 2005, **127**, 3491–3495.

[222] J. Ibarra, A. Varez, C. León, J. Santamarıa, L. Torres-Martınez and J. Sanz, *Solid State Ionics*, 2000, **134**, 219–228.

[223] Y. Zou and N. Inoue, *Ionics*, 2005, **11**, 333–342.

[224] J. Fourquet, H. Duroy and M. Crosnier-Lopez, *J. Solid State Chem.*, 1996, **127**, 283–294.

[225] T. Katsumata, Y. Inaguma, M. Itoh and K. Kawamura, *J. Ceram. Soc. Jpn.*, 1999, **107**, 615–621.

[226] T. Katsumata, Y. Inaguma, M. Itoh and K. Kawamura, *Chem. Mater*, 2002, **14**, 3930–3936.

[227] S. Stramare, V. Thangadurai and W. Weppner, *Chem. Mater*, 2003, **15**, 3974–3990.

[228] M. Itoh, Y. Inaguma, W.-H. Jung, L. Chen and T. Nakamura, *Solid State Ionics*, 1994, **70**, 203–207.

[229] V. Thangadurai and W. Weppner, *Ionics*, 2000, **6**, 70–77.

[230] Y. Zhao and L. L. Daemen, *J. Am. Chem. Soc*, 2012, **134**, 15042–15047.

[231] Y. Zhang, Y. Zhao and C. Chen, *Phys. Rev. B*, 2013, **87**, 134303.

[232] M. Braga, J. A. Ferreira, V. Stockhausen, J. Oliveira and A. El-Azab, *J. Mater. Chem. A*, 2014, **2**, 5470–5480.

[233] A. Emly, E. Kioupakis and A. Van der Ven, *Chem. Mater*, 2013, **25**, 4663–4670.

[234] R. Mouta, M. A. B. Melo, E. M. Diniz and C. W. A. Paschoal, *Chem. Mater*, 2014, **26**, 7137–7144.

[235] J. A. Dawson, T. S. Attari, H. Chen, S. P. Emge, K. E. Johnston and M. S. Islam, *Energy Environ. Sci.*, 2018, **11**, 2993–3002.

[236] J. A. Dawson, P. Canepa, T. Famprikis, C. Masquelier and M. S. Islam, *J. Am. Chem. Soc*, 2018, **140**, 362–368.

[237] E. Ahiavi, J. A. Dawson, U. Kudu, M. Courty, M. S. Islam, O. Clemens, C. Masquelier and T. Fam-

prikis, *J. Power Sources*, 2020, **471**, 228489.

[238] Y. Wang, Q. Wang, Z. Liu, Z. Zhou, S. Li, J. Zhu, R. Zou, Y. Wang, J. Lin and Y. Zhao, *J. Power Sources*, 2015, **293**, 735–740.

[239] Y. Sun, Y. Wang, X. Liang, Y. Xia, L. Peng, H. Jia, H. Li, L. Bai, J. Feng, H. Jiang *et al.*, *J. Am. Chem. Soc*, 2019, **141**, 5640–5644.

[240] J. Boilot, G. Collin and P. Colomban, *Mater. Res. Bull*, 1987, **22**, 669–676.

[241] J.-P. Boilot, G. Collin and P. Colomban, *J. Solid State Chem.*, 1988, **73**, 160–171.

[242] E. Vogel, R. Cava and E. Rietman, *Solid State Ionics*, 1984, **14**, 1–6.

[243] O. Tillement, J. Angenault, J. Couturier and M. Quarton, *Solid State Ionics*, 1991, **44**, 299–303.

[244] Q. Ma, M. Guin, S. Naqash, C.-L. Tsai, F. Tietz and O. Guillon, *Chem. Mater*, 2016, **28**, 4821–4828.

[245] D. Chen, F. Luo, W. Zhou and D. Zhu, *J. Alloys Compd*, 2018, **757**, 348–355.

[246] A. G. Jolley, D. D. Taylor, N. J. Schreiber and E. D. Wachsman, *J. Am. Ceram. Soc*, 2015, **98**, 2902–2907.

[247] F. Lalère, J.-B. Leriche, M. Courty, S. Boulineau, V. Viallet, C. Masquelier and V. Seznec, *J. Power Sources*, 2014, **247**, 975–980.

[248] Z. Jian, L. Zhao, H. Pan, Y.-S. Hu, H. Li, W. Chen and L. Chen, *Electrochem. commun.*, 2012, **14**, 86–89.

[249] Z. Jian, W. Han, X. Lu, H. Yang, Y.-S. Hu, J. Zhou, Z. Zhou, J. Li, W. Chen, D. Chen *et al.*, *Adv. Energy Mater.*, 2013, **3**, 156–160.

[250] K. Saravanan, C. W. Mason, A. Rudola, K. H. Wong and P. Balaya, *Adv. Energy Mater.*, 2013, **3**, 444–450.

[251] X. Rui, W. Sun, C. Wu, Y. Yu and Q. Yan, *Adv. Mater*, 2015, **27**, 6670–6676.

[252] S. Li, Y. Dong, L. Xu, X. Xu, L. He and L. Mai, *Adv. Mater*, 2014, **26**, 3545–3553.

[253] Y. Fang, L. Xiao, X. Ai, Y. Cao and H. Yang, *Adv. Mater*, 2015, **27**, 5895–5900.

[254] P. P. Kumar and S. Yashonath, *J. Phys. Chem. B*, 2002, **106**, 7081–7089.

[255] P. P. Kumar and S. Yashonath, *J. Am. Chem. Soc*, 2002, **124**, 3828–3829.

[256] S. Roy and P. P. Kumar, *Phys. Chem. Chem. Phys.*, 2013, **15**, 4965–4969.

[257] S. Roy and P. P. Kumar, *Solid State Ionics*, 2013, **253**, 217–222.

[258] K. M. Bui, V. A. Dinh, S. Okada and T. Ohno, *Phys. Chem. Chem. Phys.*, 2016, **18**, 27226–27231.

[259] X. He, Y. Zhu and Y. Mo, *Nat. Commun.*, 2017, **8**, 1–7.

[260] Z. Zhang, Z. Zou, K. Kaup, R. Xiao, S. Shi, M. Avdeev, Y.-S. Hu, D. Wang, B. He, H. Li *et al.*, *Adv. Energy Mater.*, 2019, **9**, 1902373.

[261] Z. Zou, N. Ma, A. Wang, Y. Ran, T. Song, Y. Jiao, J. Liu, H. Zhou, W. Shi, B. He *et al.*, *Adv. Energy Mater.*, 2001486.

[262] D. Petit, P. Colomban, G. Collin and J. Boilot, *Mater. Res. Bull*, 1986, **21**, 365–371.

[263] F. Sudreau, D. Petit and J. Boilot, *J. Solid State Chem.*, 1989, **83**, 78–90.

[264] A. Martinez-Juarez, J. M. Rojo, J. E. Iglesias and J. Sanz, *Chem. Mater*, 1995, **7**, 1857–1862.

[265] M. Subramanian, R. Subramanian and A. Clearfield, *Solid State Ionics*, 1986, **18**, 562–569.

[266] J.-M. Winand, A. Rulmont and P. Tarte, *J. Solid State Chem.*, 1991, **93**, 341–349.

[267] K. Arbi, M. Ayadi-Trabelsi and J. Sanz, *J. Mater. Chem.*, 2002, **12**, 2985–2990.

[268] A. Martinez-Juarez, R. Jimenez, P. Duran-Martin, J. Ibañez and J. M. Rojo, *J. Phys. Condens. Matter*, 1997, **9**, 4119.

[269] A. Martinez-Juarez, C. Pecharromán, J. E. Iglesias and J. M. Rojo, *J. Phys. Chem. B*, 1998, **102**, 372–375.

[270] E. R. Losilla, M. A. Aranda, M. Martinez-Lara and S. Bruque, *Chem. Mater*, 1997, **9**, 1678–1685.

[271] M. Alami, R. Brochu, J. Soubeyroux, P. Gravereau, G. Le Flem and P. Hagenmuller, *J. Solid State Chem.*, 1991, **90**, 185–193.

[272] M. A. París, A. Martínez-Juárez, J. M. Rojo and J. Sanz, *J. Phys. Condens. Matter*, 1996, **8**, 5355–5366.

[273] M. Catti, S. Stramare and R. Ibberson, *Solid State Ionics*, 1999, **123**, 173–180.

[274] M. Catti and S. Stramare, *Solid State Ionics*, 2000, **136**, 489–494.

[275] H. Aono, E. Sugimoto, Y. Sadaoka, N. Imanaka and G.-y. Adachi, *Solid State Ionics*, 1991, **47**, 257–264.

[276] H. Aono, E. Sugimoto, Y. Sadaoka, N. Imanaka and G.-y. Adachi, *J. Electrochem. Soc*, 1993, **140**, 1827.

[277] D. T. Qui, S. Hamdoune, J. Soubeyroux and E. Prince, *J. Solid State Chem.*, 1988, **72**, 309–315.

[278] K. Arbi, M. Lazarraga, D. Ben Hassen Chehimi, M. Ayadi-Trabelsi, J. Rojo and J. Sanz, *Chem. Mater*, 2004, **16**, 255–262.

[279] K. Arbi, M. Hoelzel, A. Kuhn, F. García-Alvarado and J. Sanz, *Inorg. Chem*, 2013, **52**, 9290–9296.

[280] K. Arbi, M. Hoelzel, A. Kuhn, F. Garcia-Alvarado and J. Sanz, *Phys. Chem. Chem. Phys.*, 2014, **16**, 18397–18405.

[281] K. Arbi, W. Bucheli, R. Jiménez and J. Sanz, *J. Eur. Ceram. Soc.*, 2015, **35**, 1477–1484.

[282] M. Pérez-Estébanez, J. Isasi-Marín, D. Többens, A. Rivera-Calzada and C. León, *Solid State Ionics*, 2014, **266**, 1–8.

[283] H. Aono, E. Sugimoto, Y. Sadaoka, N. Imanaka and G.-y. Adachi, *J. Electrochem. Soc*, 1990, **137**, 1023.

[284] M. Monchak, T. Hupfer, A. Senyshyn, H. Boysen, D. Chernyshov, T. Hansen, K. G. Schell, E. C. Bucharsky, M. J. Hoffmann and H. Ehrenberg, *Inorg. Chem*, 2016, **55**, 2941–2945.

[285] H. Aono, E. Sugimoto, Y. Sadaoka, N. Imanaka and G.-y. Adachi, *Bull. Chem. Soc. Jpn.*, 1992, **65**, 2200–2204.

[286] P. Hartmann, T. Leichtweiss, M. R. Busche, M. Schneider, M. Reich, J. Sann, P. Adelhelm and J. Janek, *J. Phys. Chem. C*, 2013, **117**, 21064–21074.

[287] Y. Liu, Q. Sun, Y. Zhao, B. Wang, P. Kaghazchi, K. R. Adair, R. Li, C. Zhang, J. Liu, L.-Y. Kuo *et al.*, *ACS Appl. Mater. Interfaces*, 2018, **10**, 31240–31248.

[288] E. Zhao, F. Ma, Y. Guo and Y. Jin, *RSC Adv.*, 2016, **6**, 92579–92585.

[289] H. El-Shinawi, A. Regoutz, D. J. Payne, E. J. Cussen and S. A. Corr, *J. Mater. Chem. A*, 2018, **6**, 5296–5303.

[290] Y. Zhang, K. Chen, Y. Shen, Y. Lin and C.-W. Nan, *Ceram. Int.*, 2017, **43**, S598–S602.

[291] V. Ramar, S. Kumar, S. Sivakkumar and P. Balaya, *Electrochimica Acta*, 2018, **271**, 120–126.

[292] B. Lang, B. Ziebarth and C. Elsasser, *Chem. Mater*, 2015, **27**, 5040–5048.

[293] Y. Noda, K. Nakano, M. Otake, R. Kobayashi, M. Kotobuki, L. Lu and M. Nakayama, *APL Mater.*, 2018, **6**, 060702.

[294] Y. Noda, K. Nakano, H. Takeda, M. Kotobuki, L. Lu and M. Nakayama, *Chem. Mater*, 2017, **29**, 8983–8991.

[295] M. A. Evstigneeva, V. B. Nalbandyan, A. A. Petrenko, B. S. Medvedev and A. A. Kataev, *Chem. Mater*, 2011, **23**, 1174–1181.

[296] K. Sau and P. P. Kumar, *J. Phys. Chem. C*, 2015, **119**, 1651–1658.

[297] K. Sau and P. P. Kumar, *J. Phys. Chem. C*, 2015, **119**, 18030–18037.

[298] F. Bianchini, H. Fjellvåg and P. Vajeeston, *J. Phys. Chem. C*, 2019, **123**, 4654–4663.

[299] Y. Li, Z. Deng, J. Peng, E. Chen, Y. Yu, X. Li, J. Luo, Y. Huang, J. Zhu, C. Fang *et al.*, *Chem. Eur. J*, 2018, **24**, 1057–1061.

[300] Z. Deng, J. Gu, Y. Li, S. Li, J. Peng, X. Li, J. Luo, Y. Huang, C. Fang, Q. Li *et al.*, *Electrochimica Acta*, 2019, **298**, 121–126.

[301] A. K. Bera and S. M. Yusuf, *J. Phys. Chem. C*, 2020, **124**, 4421–4429.

[302] J.-F. Wu, Z.-Y. Yu, Q. Wang and X. Guo, *Energy Stor. Mater.*, 2020, **24**, 467–471.

[303] Y. Li, Z. Deng, J. Peng, J. Gu, E. Chen, Y. Yu, J. Wu, X. Li, J. Luo, Y. Huang *et al.*, *ACS Appl. Mater. Interfaces*, 2018, **10**, 15760–15766.

[304] Y. Wang, W. D. Richards, S. P. Ong, L. J. Miara, J. C. Kim, Y. Mo and G. Ceder, *Nat. Mater.*, 2015, **14**, 1026–1031.

[305] P. Padma Kumar and S. Yashonath, *J. Phys. Chem. B*, 2002, **106**, 3443–3448.

[306] A. Taskin, A. Lavrov and Y. Ando, *Appl. Phys. Lett*, 2005, **86**, 091910.

[307] A. Taskin, A. Lavrov and Y. Ando, *Prog. Solid. State Ch.*, 2007, **35**, 481–490.

[308] D. Parfitt, A. Chroneos, A. Tarancón and J. A. Kilner, *J. Mater. Chem.*, 2011, **21**, 2183–2186.

[309] H. Shiiba, C. L. Bishop, M. J. Rushton, M. Nakayama, M. Nogami, J. A. Kilner and R. W. Grimes, *J. Mater. Chem. A*, 2013, **1**, 10345–10352.

[310] S. H. Jacobson, M. A. Ratner and A. Nitzan, *Phys. Rev. B*, 1981, **23**, 1580.

[311] N. Holzwarth, N. Lepley and Y. A. Du, *J. Power Sources*, 2011, **196**, 6870–6876.

[312] A. Ivanov-Shitz, *Crystallogr. Rep.*, 2007, **52**, 302–315.

[313] Z. Deng, Y. Mo and S. P. Ong, *NPG Asia Mater.*, 2016, **8**, e254–e254.

[314] G. Åvall, J. Mindemark, D. Brandell and P. Johansson, *Adv. Energy Mater.*, 2018, **8**, 1703036.

[315] A. A. Franco, A. Rucci, D. Brandell, C. Frayret, M. Gaberscek, P. Jankowski and P. Johansson, *Chem. Rev.*, 2019, **119**, 4569–4627.

CHAPTER 2

THEORETICAL BACKGROUND

2.1 Introduction

It was only since post world war II computers became available for general scientific research work. The first problem addressed with atomistic computer simulation was that of a dense liquid, by Metropolis et al. (1953) at Los Alamos National Laboratory, employing Monte Carlo (MC) method [1]. Several other seminal works came out in the following years. However, to investigate the dynamical properties at the atomic-scale, a different approach was needed and this lead to evolution of molecular dynamics (MD) technique. The first MD simulation was performed by Alder and Wainwright in 1956 to study the dynamics of collection of hard spheres [1, 2]. In 1964, Rahman employed MD to study the correlated motion of atoms in liquid argon [3]. This marked the first MD investigation of a realistic system, and is acclaimed for its systematicity, thus playing a major role in popularizing the technique. More than a decade later, in 1978, MD was used to study α-AgI, the first fast ion conductor to be examined computationally [4]. Soon molecular dynamics approach was widely recognized as one the most powerful methods to address a wide range of problems requiring atomic-scale 'resolution'. The investigations on fast ion conducting solids presented in this thesis are based on extensive use of molecular dynamics (MD) and metadynamics (MTD) techniques. The theoretical background of these techniques are described below.

2.2 Molecular Dynamics

The core of Molecular Dynamics (MD) simulation is to numerically solve the Newton's equations of motion for a collection of atoms, ions or molecules where analytical solution is not possible. Calculation of the inter-atomic interaction is the starting point of such iterations. Two different types of approaches are available for such calculations - *(1)* classical molecular dynamics, which relies on predefined empirical interatomic potentials, and *(2) ab initio* molecular dynamics (AIMD) in which the interatomic interaction is calculated *on the fly* by incorporating the first principle-based solution of the electronic structure of the system [1, 2, 5–9]. It is to mention that, in both cases, the dynamics of the *atoms/ions/molecules* strictly follows Newton's equation irrespective of how the inter-atomic interactions are calculated.

2.2.1 Classical MD

In *classical* MD simulation, *predefined* inter-atomic potential is used for the calculation of the force, and the second order differential equation is solved to obtain the evolution of the coordinates and velocities in real time [1, 2, 9],

$$\vec{F}_I\left(\vec{R}_I\right) = -\vec{\nabla}_I V\left(\vec{R}_I\right), \tag{2.1}$$

$$M_I \frac{d^2\vec{R}_I}{dt^2} = \vec{F}_I\left(\vec{R}_I\right), \tag{2.2}$$

The force ($\vec{F}_I$) is calculated from the negative gradient of interaction potential $V(\vec{R})$. In eq. (2.2), M_I and $\vec{R}_I$ ($\{\vec{r}_1, \vec{r}_2, \vec{r}_3, ..., \vec{r}_N\}$) are respectively mass and coordinates of the I^{th} atom, in a system of N atoms/ions. The standard algorithm begins with the initial set of atomic coordinates of the system of interest (usually obtained from experimental data) and their velocities (usually generated from a Maxwellian distribution). The desired temperature of simulation can be achieved through different ways depending upon the statistical ensemble used. In the following sections, the essential ingredients for a MD simulation, namely integration scheme, periodic boundary condition, inter-atomic potentials, various aspects related to ensembles, are discussed in some detail.

2.2.1.1 Integration Scheme

Among different available integration schemes (such as Runge-Kutta, Euler etc.) velocity verlet algorithm is perhaps one of the most popular choice for MD. This algorithm is a modification of the simple 'velocity' verlet scheme, and handles positions, velocities, and accelerations of all the particles simultaneously. The algorithm is of the form of,

$$\vec{R}(t+\Delta t) = \vec{R}(t)+\vec{v}(t)\Delta t+\frac{1}{2}\frac{\vec{F}(t)}{M}\Delta t^2 \tag{2.3a}$$

$$\vec{v}(t+\Delta t) = \vec{v}(t)+\frac{\Delta t}{2M}\left(\vec{F}(t+\Delta t)+\vec{F}(t)\right), \tag{2.3b}$$

Elaborately,

- Move the velocity by *half* time-step using the initial velocity and acceleration,

$$\vec{v}(t+\frac{\Delta t}{2}) = \vec{v}(t)+\frac{\vec{F}(t)}{2M}\Delta t \tag{2.4}$$

- Move the positions as,

$$\vec{R}(t+\Delta t) = \vec{R}(t)+\vec{v}(t+\frac{\Delta t}{2})\Delta t \tag{2.5}$$

- Calculate the new accelerations $\vec{a}(t+\Delta t)$ from the new positions $\vec{R}(t+\Delta t)$
- Move the velocities to full time step using,

$$\vec{v}(t+\Delta t) = \vec{v}(t+\frac{\Delta t}{2})+\frac{1}{2}\vec{a}(t+\Delta t)\Delta t \tag{2.6}$$

As the new set of positions and velocities of the atoms are available, new iterations are performed to generate the trajectory.

2.2.1.2 Periodic Boundary Condition (PBC)

The number of atoms that can be handled within a reasonable computational expenditure lies typically between 1000-10000. But, as any real *bulk* system consists of much larger number of atoms, of the order of 10^{23}, calculations limiting to this low number of atoms gives rise to spurious '*surface effects*'. This problem arises as large number of atoms resides at boundaries in comparison with the real bulk system. As a result these large number of surface atoms feels a completely different environment than the atoms residing at the central region.

Imposing periodic boundary condition (PBC) is an effective way to eliminate this so called 'surface effects' during simulation. This method allows an atom to re-enter from the opposite boundary of the simulation box in case it is leaving the simulation box from one boundary. In other words, one boundary of the simulation box, under PBC, always '*feels*' the opposite boundary of the box. In practice, this phenomena is realized by considering adjacent '*images*' of the simulation box in all direction as follows,

$$x' = x_{box} + n_x L_x \tag{2.7a}$$

$$y' = y_{box} + n_y L_y \tag{2.7b}$$

$$z' = z_{box} + n_z L_z \tag{2.7c}$$

where x_{box}, y_{box}, z_{box} are position coordinates of the particle inside the simulation cell, n_x, n_y, n_z are integer numbers representing the number of images in each direction, L_x, L_y, L_z are the lattice vectors. In case the simulation box is non-orthogonal, the *real* coordinates of the atoms are usually transformed into what is called 'scaled' coordinates through a matrix multiplication. This matrix is termed as '*h-matrix*' and looks like,

$$h = \begin{pmatrix} a_x & b_x & c_x \\ 0 & b_y & c_y \\ 0 & 0 & c_z \end{pmatrix} \tag{2.8}$$

where the matrix elements are different components of the lattice vectors, $\vec{a}$, $\vec{b}$ and $\vec{c}$ of the *simulation box*. The '*scaled*' coordinates is obtained by,

$$\vec{s} = h^{-1}\vec{r} \tag{2.9}$$

which will provide a orthogonal box with unit dimensions. The PBC can be applied in standard way, following equations (2.7) but for a cubic box of unit dimensions. Then all the coordinates are transformed back to real coordinates by,

$$\vec{r} = h\vec{s} \tag{2.10}$$

2.2.1.3 Inter-atomic Potential

The accuracy of the results produced from classical MD majorly depends on the inter-atomic potential form and parameters used for the simulation. Some of the popular functional forms for inter-atomic potential available in the literature are, Lennard-Jones, Vashistha Rahman, Born Mayer etc.

Lennard-Jones potential is given as,

$$V = 4\epsilon[(\frac{\sigma}{r_{ij}})^{12} - (\frac{\sigma}{r_{ij}})^{6}] \tag{2.11}$$

where ϵ is the depth of the potential at the equilibrium distance for a pair of atom, σ is the diameter of atom and r_{ij} is the distance between two atoms. The first term in the bracket represents the Pauli repulsion originating from the electron cloud overlapping and the second term represents the attractive part originating from the instantaneous dipole-dipole interactions. Lennard-Jones potential is extensively used to simulate inert gas systems, such as, argon, but can be extended to simulate certain ionic solids by adding the Coulombic term to the potential.

The functional form of Born Mayer (Buckingham) potential[10] is given as,

$$V = \frac{q_i q_j}{r_{ij}} + A_{ij}\exp(\frac{r_{ij}}{\rho}) - \frac{D_{ij}}{r_{ij}^{8}} - \frac{C_{ij}}{r_{ij}^{6}} \tag{2.12}$$

where q is the charge, A_{ij} and ρ are respectively the strength and range of the overlap repulsive term, D_{ij}, C_{ij} are respectively the dipole-quadrupole interaction term and the dipole-dipole interaction term. This potential has widely been employed to simulate inorganic solids, molten salts and many fast ion conductors such as β-alumina, Li_3N, CaF_2 etc.

The Vashistha Rahman potential [4] is given as,

$$V = \frac{q_i q_j}{r_{ij}} + A_{ij}\frac{(\sigma_i + \sigma_j)^{n_{ij}}}{r_{ij}^{n_{ij}}} - \frac{P_{ij}}{r_{ij}^{4}} - \frac{C_{ij}}{r_{ij}^{6}} \tag{2.13}$$

where q is the charge, σ is ionic radius, A_{ij}, P_{ij}, C_{ij} are respectively the overlap repulsive term, charge dipole interaction and the dispersion energy terms. n_{ij} is usually taken as 11, 9 and 7 for *cation-cation*, *cation-anion* and *anion-anion* pairs respectively. This potential form was first proposed for the study of fast ion conductor AgI. Later on, it has been implemented to study several other fast ion conductors as well.

While calculating the interaction potentials under PBC, if all the '*real atoms*' and the '*images*' are considered, the computational expenditure will be too high and such calculations may be unnecessary as well. For ionic systems, the potential usually consists of two parts, the *short range* term and the *long range Couloumbic* term. To minimize the computational expenditure, often a *cut off* distance (R_c) is incorporated beyond which the potential energy contributions from the short-range interactions are neglected. The implementation of *cut off* distance is pretty straightforward for the *short range* term, and is incorporated in such a way that an atom will either interact with another atom or it's image, whichever is nearer – but not both. This is known as *minimum image convention* in which the *cut off* is usually chosen as half the box length ($R_c \leq L/2$).

2.2.2 Ewald Summation

But when Coulombic interaction comes into the scenario, special care is needed as this long range interaction doesn't converge within the *cut off*. To deal with this difficulty, a well known technique, known as '*Ewald summation*', is implemented.

Under periodic boundary condition (PBC), the Coulombic contribution from all the periodic images has to be considered. For a 'N' particle system, thus, the total potential for the Coulombic part is given as,

$$U = \frac{1}{8\pi\epsilon_o} \sum_n \sum_{i=1}^{N} \sum_{j=1}^{N} \frac{q_i q_j}{|\vec{r}_{ij} + n\vec{L}|} \tag{2.14}$$

where $\vec{L}$ (L_x, L_y, L_z) are the lattice vectors and n is the number of periodic images. To begin with, Ewald summation method assumes a Gaussian charge distribution of opposite sign but same magnitude around each and every charge q_i so that the total charge of this distribution precisely cancels the q_i out. Another Gaussian charge distribution same as the original charge is also assumed to compensate the Gaussian distributions mentioned earlier. The contributions from the parts of this arrangement can be split into a short range and a long range part.

2.2.2.1 Short range part

The Gaussian charge distribution of opposite signs screen the neighboring ion's interaction and the screened interactions become short ranged. The Gaussian charge is given as,

$$\rho(r) \ = \ -q_j (\frac{\alpha}{\pi})^{\frac{3}{2}} \exp(-\alpha r^2) \tag{2.15}$$

where α is the width of the Gaussian. The potential at some distance r due to this distribution is given as,

$$\phi_s \ = \ -\frac{q_j}{r} \operatorname{erf}\sqrt{(\alpha r)} \tag{2.16}$$

here 'erf' is known as *error function* and defined as,

$$\operatorname{erf}(z) \ = \ \frac{2}{\sqrt{\pi}} \int_0^z e^{-t^2}\, dt \tag{2.17}$$

So, the potential due to the screened charge at some distance r is given as,

$$\phi_{\text{screened}} = \phi_p + \phi_s = \frac{q_j}{r} - \frac{q_j}{r}\text{erf}\sqrt{(\alpha r)} = \frac{q_j}{r}\text{erfc}(\sqrt{\alpha r}) \tag{2.18}$$

where 'erfc' is known as complimentary error function and given as $\text{erfc}(z) = 1 - \text{erf}(z)$. The total potential coming from this part, thus given as,

$$U_{\text{short}} = \frac{1}{2}\sum_{i\neq j}\frac{q_i q_j\,\text{erfc}(\sqrt{\alpha r})}{\vec{r}_{ij}} \tag{2.19}$$

2.2.2.2 The Self Term

The potential at $r = 0$, arises because of the self interaction between the Gaussian and the corresponding point charge, is to be subtracted . This can be obtained from eq (2.16) as,

$$U_{\text{self}} = (\frac{\alpha}{\pi})^{\frac{1}{2}}\sum_{i=1}^{N}{q_i}^2 \tag{2.20}$$

2.2.2.3 The Long-range Term

The interaction between the compensating Gaussian charge distributions is long range one and in Ewald's method, the potential energy due to these charges is calculated in the reciprocal space and obtained as,

$$U_{\text{long}} = \frac{1}{2V}\sum_{k\neq 0}|\rho(\vec{k})|^2\exp(-\frac{k^2}{4\alpha}) \tag{2.21}$$

where,

$$\rho(\vec{k}) = \sum_{i=1}^{N} q_i\, e^{i\vec{k}.\vec{r}_i} \tag{2.22}$$

Thus, the total potential energy is given as,

$$\begin{aligned} U_{\text{ewald}} &= U_{\text{short}} + U_{\text{long}} - U_{\text{self}} \\ &= \frac{1}{2}\sum_{i\neq j}\frac{q_i q_j\,\text{erfc}(\sqrt{\alpha r})}{\vec{r}_{ij}} + \frac{1}{2V}\sum_{k\neq 0}|\rho(\mathbf{k})|^2\exp(-\frac{k^2}{4\alpha}) - (\frac{\alpha}{\pi})^{\frac{1}{2}}\sum_{i=1}^{N}{q_i}^2 \end{aligned} \tag{2.23}$$

2.2.3 Aspects of Different Ensembles

2.2.3.1 Microcanonical Ensemble (NVE)

Performing MD in a microcanonical ensemble (NVE) is straightforward. Simply integrating the equation of motion, following the steps mentioned in the previous sections, gives us results for a NVE ensemble because of the conservation of the total Hamiltonian of the system.

But the algorithm, discussed so far, does not provide any control over the temperature. So, to perform NVE-MD at a desired temperature, a technique, known as *velocity re-scaling* is employed. The equipartion theorem tells,

$$\frac{3}{2}Nk_BT = \frac{1}{2}M\vec{v}^2 \tag{2.24}$$

From (2.24), the *instantaneous* (T_{in}) and *required* (T_r) temperature can be written as,

$$T_{in} = \frac{\sum_{i=1}^{N} M_i(\vec{v}_i^{in})^2}{3Nk_B} \tag{2.25a}$$

$$T_r = \frac{\sum_{i=1}^{N} M_i(\vec{v}_i^{r})^2}{3Nk_B} \tag{2.25b}$$

From (2.25a) and (2.25b), It can be shown that the required temperature (T_r) for the simulation can be achieved by multiplying the instantaneous velocity ($\vec{v}_i^{in}$) with a *scale factor* and thus re-scale the velocity as,

$$\vec{v}_i^r = \sqrt{\frac{T_r}{T_{in}}}\,\vec{v}_i^{in} \tag{2.26}$$

This *velocity re-scaling* is usually done for certain initial steps and then the production phase is performed without the *scaling*.

2.2.3.2 Canonical Ensemble (NVT)

Unlike NVE-MD, NVT-MD can not be performed by simple integration of the equation of motion as the total energy of the system in the later case is not conserved. The total energy or the Hamiltonian of the system fluctuates and generates a Boltzmann distribution. This happens because of the energy exchange between the system and thermal bath. To simulate a system in contact with a thermal bath, different techniques have been introduced by different groups, like Andersen [11], Nose and Klein [12] etc. In this section we will briefly discuss the extended Hamiltonian approach developed by Nose and Hoover[12–14].

The Hamiltonian of system connected with a thermal bath is written as,

$$H_{nh} = \sum_{i=1}^{N} \frac{\vec{p}_i^2}{2M_i s^2} + U(r) + \frac{p_s^2}{2Q} + gk_BTln(s) \tag{2.27}$$

Here the 3^{rd} and the 4^{th} terms are to introduce a '*Maxwell daemon*' like agent[15], denoted by '*s*', that checks the instantaneous kinetic energy and adjust it to achieve the desired temperature. '*Q*' is a factor that decides the frequency at which the kinetic energy is modulated. $gk_BTln(s)$ is formulated, with the 'g' chosen in a way so that the micro-canonical distribution in $2dN+2$ (where d is spatial dimension, and 2 is added for 's' and p_s) will eventually give canonical distribution in the physical space [15]. It can be shown that in molecular dynamics simulation by implementing this Nose Hamiltonian, H_{nh} will eventually generate a canonical distribution, $e^{-\beta H(\vec{r},\vec{p})}$ for the physical Hamiltonian given that ergodicity is maintained.

2.2.3.3 Isothermal-Isobaric Ensemble (NPT)

From experimental perspective, isothermal-isobaric ensemble is the most realistic one as experiments are majorly done in a constant pressure environment where the cell volume is allowed to fluctuate. This condition can be mimicked in MD simulation by adding another degree of freedom to the Hamiltonian as[15],

$$H_{nh} = \sum_{i=1}^{N} \frac{\vec{p}_i^2}{2M_i s^2} + U(r) + \frac{p_s^2}{2Q} + gk_BTln(s) + \frac{p_v^2}{2W} + P_{ex}V \tag{2.28}$$

where p_v is conjugate momentum of the volume and W is a fictitious mass that decides the time scale at which the volume changes. In NPT-MD simulation the volume of the cell is thus allowed to fluctuate depending on the difference between the internal stress and the external pressure (P_{ex}).

2.2.4 Ab Initio Molecular Dynamics

One of the fundamental shortcomings of classical MD is the availability and accuracy of the interaction potential and their parameters. They are highly non trivial across different systems and the difficulty with parameterization rises as the types of molecules increases in the system. Also, classical MD can not be used for the study of '*chemically active*' systems as it can't account for events like bond breaking or making. These limitations of classical MD is overcome in *first-principles* based approach known as *ab-initio* molecular dynamics (AIMD). In AIMD, the forces between atoms are calculated *on-the-fly* from electronic structure calculation. Although AIMD calculation is computationally very expensive, numerous studies in various fields, over last three decades have exhibited the efficiency and predictive power of the method. In the following sections, the theoretical overview of AIMD simulation is presented.

The Hamiltonian corresponding to a many-body problem can be written as,

$$H = T_N + T_e + V_{ee} + V_{Ne} + V_{NN} \tag{2.29}$$

where, T_N and T_e are respectively nuclear and electronic kinetic energy. V_{ee}, V_{Ne} and V_{NN} are respectively the electron-electron, nucleus-electron and nucleus-nucleus potential energies. Thus,

$$\begin{aligned} H &= -\frac{1}{2}\sum_I \frac{1}{M_I}\vec{\nabla}_I^2 - \frac{1}{2}\sum_i \vec{\nabla}_i^2 + \sum_{i<j}\frac{1}{|\vec{r}_i - \vec{r}_j|} - \sum_{I,i}\frac{Z_I}{|\vec{R}_I - \vec{r}_i|} + \sum_{I<J}\frac{Z_I Z_J}{|\vec{R}_I - \vec{R}_J|} && \text{(2.30a)} \\ &= -\sum_I \frac{\vec{\nabla}_I^2}{2M_I} + H_e(\{\vec{r}_i\},\vec{R}) && \text{(2.30b)} \end{aligned}$$

where $\vec{r}$ and $\vec{R}$ are respectively the electronic and nuclear degrees of freedom. M_I and Z_I represent the mass and atomic number of the I^{th} nucleus respectively. $H_e(\{\vec{r}_i\},\vec{R})$ represents the electronic part of the $H(\{\vec{r}_i\},\vec{R})$. If $\Psi\left(\{\vec{r}_i\},\vec{R};t\right)$ is the total wavefunction, then the time dependent Schrödinger equation, to be solved is,

$$i\hbar\frac{\partial}{\partial t}\Psi\left(\{\vec{r}_i\},\vec{R};t\right) = \hat{H}\Psi\left(\{\vec{r}_i\},\vec{R};t\right) \tag{2.31}$$

The *Born-Oppenheimer approximation* [16–18] allows the motion of the nuclei and the electrons to be treated separately. By considering that the electrons are in instantaneous equilibrium positions with the nuclei, the T_N in (2.30) term can be neglected which brings the many body problem down to a only electronic structure problem. In that case, the Hamiltonian to be considered is the electronic one, *i.e.* $H_e(\{\vec{r}_i\},\vec{R})$ with parametric dependence on the nuclei position $\vec{R}$. The total wave function can then be written as the product of the nuclear and electronic wave functions [18–20],

$$\Psi\left(\{\vec{r}_i\},\vec{R};t\right) = \psi\left(\{\vec{r}_i\};\vec{R}\right) \times \psi_N\left(\vec{R};t\right). \tag{2.32}$$

The time independent many-body Schrödinger equation for the ground state electronic sub-system can be solved from,

$$\hat{H}_e\left(\{\vec{r}_i\};\vec{R}\right)\psi_0(\{\vec{r}_i\}) = \epsilon_0\left(\vec{R}\right)\psi_0(\{\vec{r}_i\}), \tag{2.33}$$

where $\epsilon_0\left(\vec{R}\right)$ represents the ground state eigenvalues. Once the electronic structure problem is solved, the forces on the ions can be computed using,

$$\vec{F}_I = -\nabla_I\langle\psi_0|\hat{H}_e|\psi_0\rangle, \tag{2.34}$$

After obtaining the forces between the ions, the equation of motion can be solved as described in the previous section to get the real time evolution of the system in interest.

Born-Oppenheimer Molecular Dynamics

Born-Oppenheimer Molecular Dynamics (BOMD) is one of the two major approaches to AIMD simulation in which the time-independent Schrödinger equation for electrons is solved for each nuclear configuration $\vec{R}_I$, and the time evolution is incorporated via its parametric dependence on the dynamics of the nuclei [21–24]. The Lagrangian that describes the BOMD dynamics is given as,

$$\mathscr{L}_{\mathrm{BO}} = \frac{1}{2}\sum_I M_I \dot{\vec{R}}_I^2 - \min_{\{\psi_i\}}\langle\Psi_0|\hat{H}_e|\Psi_0\rangle + \sum_{i,j}\Lambda_{ij}\left(\langle\psi_i|\psi_j\rangle - \delta_{ij}\right), \tag{2.35}$$

where the first term represents the kinetic energy of nuclei, the second term (where Ψ_0 is the Slater determinant, and ψ_i is one electron wave function) is the potential energy which is to be minimized at every MD step and the Hermitian Lagrangian matrix is represented by Λ_{ij} which maintain the ortho-normality constraints. Now, as per Euler-Lagrange equations for this case,

$$\frac{d}{dt}\left(\frac{\partial \mathscr{L}}{\partial \dot{\vec{R}}_I}\right) = \frac{\partial \mathscr{L}}{\partial \vec{R}_I} \tag{2.36a}$$

$$\frac{\delta \mathscr{L}}{\delta \psi_i^*} = 0 \tag{2.36b}$$

which gives the equations of motion as,

$$M_I \ddot{\vec{R}}_I(t) = -\vec{\nabla}_I \min_{\{\psi_i\}}\left\{\left\langle\Psi_0\middle|\hat{H}_e\middle|\Psi_0\right\rangle\right\} \tag{2.37}$$

$< \Psi_0\left|\hat{H}_e\right|\Psi_0 >$ is generally solved using density functional theory (DFT). The necessity of solving the electron structure problem at every MD step makes BOMD intrinsically more expensive in terms of computational power.

Car-Parrinello Molecular Dynamics

Roberto Car and Michele Parrinello, in 1985, proposed a new approach to AIMD simulation in which the computational expenditure is significantly reduced [5]. Car-Parrinello Molecular Dynamics (CPMD) [5, 18] is founded on the idea of adiabatic time scale separation between the fast electronic and the slow nucleus degrees of freedom. In CPMD, the problem is dealt as two-component pure classical system with explicit time dependence of the fast electrons. The Lagrangian in this case is given as [5],

$$\mathscr{L}_{\mathrm{CP}} = \frac{1}{2}\sum_I M_I \dot{\vec{R}}_I^2 + \sum_i \mu \left\langle \dot{\psi}_i | \dot{\psi}_i \right\rangle - \langle \Psi_0 | \widehat{H}_e^{\mathrm{KS}} | \Psi_0 \rangle + \sum_{i,j} \Lambda_{ij} \left(\langle \psi_i | \psi_j \rangle - \delta_{ij} \right), \tag{2.38}$$

The second term in the equation adds an artificial kinetic energy to the electrons and μ represents fictitious electronic mass. From the Euler-Lagrange equation [25], as mentioned in Eqs. (2.36a)-(2.36b), the equation of motions for the nuclei and the electrons in CPMD obtained as,

$$M_I \ddot{\vec{R}}_I(t) = -\vec{\nabla}_I \left\langle \Psi_0 | \widehat{H}_e^{\mathrm{KS}} | \Psi_0 \right\rangle \tag{2.39a}$$

$$\mu \ddot{\psi}_i(t) = -H_e^{\mathrm{KS}} \psi_i + \sum_j \Lambda_{ij} \psi_j, \tag{2.39b}$$

where H_e^{KS} is the Kohn-Sham electronic Hamiltonian. The second order time derivative in Eq (2.39b) clearly indicates that, unlike BOMD, the electronic part in this case is a dynamic quantity[ref].

Hellmann-Feynman Forces

A numerical calculation of the force on the nuclei by using $\vec{F}_I = -\vec{\nabla}_I \langle \Psi_0 | \widehat{H}_e | \Psi_0 \rangle$ is very expensive and can be highly inaccurate for simulations. Analytically, the expression can be written as,

$$\begin{aligned} \vec{F}_I &= -\vec{\nabla}_I \langle \Psi_0 | \widehat{H}_e | \Psi_0 \rangle \\ &= -\langle \Psi_0 | \vec{\nabla}_I \widehat{H}_e | \Psi_0 \rangle - \langle \vec{\nabla}_I \Psi_0 | \widehat{H}_e | \Psi_0 \rangle - \langle \Psi_0 | \widehat{H}_e | \vec{\nabla}_I \Psi_0 \rangle \end{aligned} \tag{2.40}$$

For stationary state wavefuctions, the contributions coming from $\vec{\nabla}_I \Psi_0$ vanish and Eq. (2.40) becomes,

$$\vec{F}_I = -\left\langle \Psi_0 | \vec{\nabla}_I \widehat{H}_e | \Psi_0 \right\rangle \tag{2.41}$$

This is the Hellmann-Feynman Theorem (HFT) [26–28] , using which the force calculation becomes simplified.

2.3 Brief Overview of Density Functional Theory

The solution of the time independent, many-body Schrödinger equation is the most complicated and expensive part due to dimensionality of the electronic subsystem. Based on the two papers by Hohenberg, Kohn and Sham [7, 8], density functional theory (DFT) is an magical tool to reduce the complexity. The two fundamental theorems of DFT are,

Theorem 1. *The ground state energy is a unique functional of the electronic density*

Theorem 2. *The electron density that minimizes the total energy is the exact ground-state density [7].*

Use of electron density instead of wave function reduces the degrees of freedom of the many-body problem from $3N_e$ to 3. The energy functional, thus can be expressed as,

$$E[n] = T[n] + U[n] + \int V_{\text{ext}}(\vec{r})n(\vec{r}) \tag{2.42}$$

The third term in Eq (2.42) is the external potential, the first and the second terms are respectively electronic kinetic energy and electron-electron interaction energy. This energy functional takes minimum value for the exact ground state density, and hence the ground state can be obtained by minimizing it:

$$E_0 = E^{\text{DFT}}[n_0] = \min_{\psi}\langle\psi|\widehat{H}_e|\psi\rangle = \min_{\rho}\langle\psi[\rho]|\widehat{H}_e[\rho]|\psi[\rho]\rangle = \min_{\rho} E^{\text{DFT}}[n_0], \tag{2.43}$$

The $T[n]$, $U[n]$ terms in Eq (2.42) is unknown quantity which prevents exact solution of the problem , so, physically sound approximations are required. In *Thomas-Fermi approximation*[29] the electron-electron interaction energy is approximated by the *Hartree energy*[30],

$$U \approx U_H\left[n(\vec{r})\right] = \frac{1}{2}\iint d\vec{r}\, d\vec{r}'\, \frac{n(\vec{r})n\left(\vec{r}'\right)}{|\vec{r}-\vec{r}'|} \tag{2.44}$$

which is basically the classical electrostatic interaction energy between the electron densities $n(\vec{r})$ and $n\left(\vec{r}'\right)$. Handling the electronic kinetic energy term (T) is more tricky as it contains a $\vec{\nabla}^2$-term. As per Kohn-Sham (KS) scheme, an important approximation is made at this point,

$$n(\vec{r}) = \sum_{i=1}^{N_{\text{occ}}} f_i \phi_i(\vec{r})\phi_i^*(\vec{r}), \tag{2.45}$$

where a fictitious single-particle wave function, known as Kohn-Sham (KS) orbitals [8] is represented as ϕ_i. N_{occ} represents the number of occupied orbitals and f_i is the occupation number for state i and related to the number of electrons (N_e) by the following relation

$$\sum_{i=1}^{N_{\text{occ}}} f_i = N_e, \tag{2.46}$$

Thus the electronic kinetic energy term is approximated as,

$$T \approx -\frac{1}{2}\sum_{i=1}^{N_e}\int \phi_i^*(\vec{r})\vec{\nabla}^2\phi_i(\vec{r})d\vec{r} \;=\; T_s\left[\{\phi_i\left[n(\vec{r})\right]\}\right]. \tag{2.47}$$

Effectively, the actual many particle problem is now reshaped as a non-interacting single-particle problem with the same electron density. With above sets of simplifications, the KS-energy functional becomes,

$$E^{\text{KS}}[\{\phi_i\}] \;=\; T[\{\phi_i\}] + \int V_{\text{ext}}(\vec{r})n(\vec{r})\text{d}\vec{r} + \frac{1}{2}\int U_{\text{H}}(\vec{r})n(\vec{r})\text{d}\vec{r} + E_{\text{xc}}[n], \tag{2.48}$$

where,

$$E_{\text{XC}} \;=\; \left(T[n(\vec{r})] - T_s\left[\{\phi_i\left[n(\vec{r})\right]\}\right]\right) + \left(U[n(\vec{r})] - U_H[n(\vec{r})]\right) \tag{2.49}$$

known as the *exchange and correlation* (XC) functional [7, 8], representing the many-body correlation effect and according to HK theorem, is also a functional of $n(r)$. For practical applications, many approximations are available for E_{XC}, such as Local Density Approximation (LDA), Generalized Gradient Approximation (GGA) etc [31].

To obtain the ground state, $E^{\text{KS}}[\{\phi_i\}]$ is to be minimized w.r.t. electron density. Eventually one obtain the KS equation as follow,

$$\left[-\frac{1}{2}\vec{\nabla}^2 + V^{\text{KS}}(\vec{r})\right]\phi_i(\vec{r}) \;= \epsilon_i\phi_i(\vec{r}) \tag{2.50a}$$

$$H_e^{\text{KS}}\phi_i(\vec{r}) \;= \epsilon_i\phi_i(\vec{r}), \tag{2.50b}$$

Pseudopotential

The computational cost of DFT calculation can significantly be reduced by explicit consideration of valance electrons and replacing the core potential with a effective one. This effective potential is known as the pseudopotential. For practical purposes in plane-wave electronic structure algorithms the commonly used pseudopotentials are Norm-conserving [32] and Ultra-soft (USP) [33]. First developed by Kleinman and Bylander [34], in norm-conserving pseudo-potentials, the pseudo- and all-electron wave-functions have equal norms inside a cutoff distance r_c. A new *softer* pseudopotential was proposed by Vanderbilt [33] which facilitate the use of smaller cutoff and known as ultra-soft pseudo-potential.

2.4 Metadynamics

MD study of ion diffusion mechanism in various promising electrolyte materials faces one common challenge when dealing with relatively low conducting systems. In such *slow* diffusive systems, the time scale needed to generate ion diffusion through MD is often very large. Given the fact that in standard MD simulation the appropriate time step for the integration of equations of motion is of the order of *femtoseconds*, the required time length for a simulation to study such slow diffusing systems are in general computationally unfeasible.

Such 'rare events' are very common in numerous problems of interest across scientific disciplines, thus posing great computational challenges. Several methods have been proposed in the past to deal with such 'rare events' [15]. Among them, metadynamics(MTD) is perhaps one of the most well reputed techniques that can overcome the above mentioned limitation of MD by 'accelerating' the event. Originally proposed by Laio and Parrinello [35], MTD method applies small *'hills'* (external potential) on the appropriate collective variable (*CV*), and encourage the system to escape the free energy minima. As these *'hills'* keep adding up filling up the local potential energy minima, the system is rather strongly discouraged to revisit the same place in the configuration space. Also, because of the accumulative nature of the '*hills*', MTD technique is able to map the underlying free energy landscape efficiently. Since the method's inception, MTD has underwent several improvements and modifications [36–39]. MTD method so far proved to be extremely useful in different fields of studies, such as chemical reactions, bond breaking etc.

The external bias potential, in its basic form can be written as,

$$V(\vec{s},t) = \sum_{t_g<t} H_0 \exp[\sum_i \frac{(s_i - s_i(t_g))^2}{2\sigma^2}] \tag{2.51}$$

where H_0 is the height of the Gaussian, σ is the width of the Gaussian, t_g is the instant at which the potential is applied, s is the appropriate collective variable. As $t \rightarrow \infty$, the underlying free energy landscape can be reconstructed simply from the accumulated bias potential as,

$$F(\vec{s}) = -V(\vec{s},t) + c \tag{2.52}$$

where c is a constant.

A more efficient variant of the MTD simulation, known as 'well-tempered' metadynamics [38] has been adopted in the fourth and fifth chapters of this thesis, where two promising classes of solid electrolytes are examined. The mathematical details of the technique and its implementation are discussed more elaborately in the respective chapters.

2.5 Nudged Elastic Band method

Nudged elastic band method (NEB) is one of the most efficient and popular technique to determine the minimum energy path from an initial state to a final state [40]. The calculation is realized by considering multiple intermediate 'images' between the initial and the final state, which are all connected to each other through what can be considered as an elastic band. The convergence of the arrangement to the minimum energy path is then achieved by minimizing the force acting on each of the images. The total force acting on the images can be written as,

$$\vec{F}_i \;=\; -\nabla V(\vec{R}_i) + \vec{F}_i^{\,\text{spring}} \tag{2.53}$$

where the first term on the right hand side is the force on the i^{th} image due to the potential energy (known as 'true force') and the second term is the spring force, given as,

$$\vec{F}_i^{\,\text{spring}} \;=\; k_{i+1}(\vec{R}_{i+1} - \vec{R}_i) - k_i(\vec{R}_i - \vec{R}_{i-1}) \tag{2.54}$$

k being the spring constant. Now, minimizing eq (2.54) in order to obtain the minimum energy path is what is known as '*plain elastic band*' method, in which the component of the spring force perpendicular to the path and the component of the true force parallel to the path restrict the desired convergence. The simple solution to this problem, achieved through considering out those components. So, in NEB method, eq (2.54) looks like,

$$\vec{F'}_i \;=\; -\nabla V(\vec{R}_i)_\perp + \vec{F}_{i\parallel}^{\,\text{spring}} \tag{2.55}$$

Eliminating the perpendicular component of the spring force completely can results acute kinks in the path in case of some systems. In the original implementation of NEB, solution to this 'kinks' was obtained by introducing a switching function which turns on and off depending on the deviation of the angle between the vectors $(\vec{R}_{i+1} - \vec{R}_i)$ and $(\vec{R}_i - \vec{R}_{i-1})$ [40]. Later on an improved tangent definition technique was introduced with which smooth convergence can be achieved [41].

Another addition to the standard NEB method is known as the climbing image NEB (CI-NEB) [42], in which after the convergence achieved in the regular NEB calculation, the shape of the minimum energy path is preserved and the image with the highest energy is identified and the force on it is redefined as,

$$\vec{F}_{i=max} = -\nabla V(\vec{R}_{i=max})_{\perp} + \nabla V(\vec{R}_{i=max})_{\parallel} \tag{2.56}$$

which means, the total force it feels is only due to the potential energy with the component along the tangent 'inverted'. This causes the image with maximum energy to climb up along the band to reach the saddle point (it is to note that the image is allowed to climb down the energy, but only perpendicular to the band). Thus a rigorous convergence to the exact saddle point is achieved.

2.6 Basic Analysis

2.6.1 Radial Distribution Function

Calculation of radial distribution function (RDF) is similar to the XRD technique in experiment from which the structural information can be obtained. It provides the probability of finding an atom as a function of the distance from a reference atom. The dynamic RDF is calculated by averaging over the frames in MD-trajectory. Usually dynamic RDF shows some broadening around the static RDF depending on diffusivity of the atom. The RDF is defined as,

$$g(r) = \frac{V}{4\pi r^2 \Delta r N^2} \sum_{i=1}^{N} n_i(r, \Delta r) \tag{2.57}$$

where, V is the volume of the simulation box, N is total number of atom, n is the number of atom in a spherical shell defined by two spheres of radius r and Δr. Running coordination number, which essentially provides the number neighboring atoms as a function of distance from a reference atom, can be obtained from integrating $g(r)$ as following,

$$C(n) = 4\pi \int_0^r r^2 n g(r) dr \tag{2.58}$$

where n is the global density of atoms.

2.6.2 Diffusivity and Conductivity

Diffusivity and conductivity are two important quantities in the study of solid state ionics. The mean squared displacement of an *ion* can be calculated simply from,

$$MSD = < |r(t) - r(0)|^2 > \tag{2.59}$$

In practice, multiple time origins are considered for averaging in eq (2.59). The diffusivity (D) of the *ion*, then can be calculated from the slop of the MSD-time plot using the Einstein's equation, given as

$$D = \lim_{t' \to \infty} \frac{< |r(t+t') - r(t)|^2 >}{6t'} \tag{2.60}$$

Then by using Nernst-Einstein equation, the conductivity σ calculated as,

$$\sigma = \frac{nq^2 D}{H_r k_B T} \tag{2.61}$$

where n is the number density of the ion, q is the charge, H_r is Haven ratio, k_B is the Boltzmann constant and D is the self diffusivity at temperature T.

Activation energy (E_a) is another essential quantity which tells the energy barrier associated. Arrhenius's equation gives,

$$D = D_0 \exp[-\frac{E_a}{k_B T}] \tag{2.62}$$

So,

$$\sigma = \frac{nq^2 D_0}{k_B T} \exp[-\frac{E_a}{k_B T}] = \sigma_0 \frac{\exp[-\frac{E_a}{k_B T}]}{T} \tag{2.63}$$

Or,

$$\log(\sigma T) = \log(\sigma_0) - \frac{E_a}{k_B T} \tag{2.64}$$

$\log(\sigma_0)$ in eq (2.64) being a constant, the slope of $log(\sigma T)\, vs.\, \frac{1}{T}$ plot gives the activation energy E_a.

Apart from the above mentioned standard analyses of the MD-trajectories, spatial distribution function (SDF) calculation that provides the three dimensional density distribution has also been employed in the works presented in this thesis. The rest of the problem specific analysis were done using in house developed programs.

BIBLIOGRAPHY

[1] M. P. Allen and D. J. Tildesley, *Computer simulation of liquids*, Oxford university press, 2017.

[2] D. Frenkel and B. Smit, *Understanding molecular simulation: From algorithms to applications*, Elsevier (formerly published by Academic Press), 2002, vol. 1, pp. 1–638.

[3] A. Rahman, *Physical review*, 1964, **136**, A405.

[4] P. Vashishta and A. Rahman, *Phys. Rev. Lett.*, 1978, **40**, 1337.

[5] R. Car and M. Parrinello, *Phys. Rev. Lett.*, 1985, **55**, 2471.

[6] D. Marx and J. Hutter, *Modern methods and algorithms of quantum chemistry*, John von Neumann Institute for Computing (NIC), 2000, pp. 301–449.

[7] P. Hohenberg and W. Kohn, *Phys. Rev.*, 1964, **136**, B864.

[8] W. Kohn and L. J. Sham, *Phys. Rev.*, 1965, **140**, A1133.

[9] C. Gray and K. Gubbins, *Fundamentals (Theory of Molecular Fluids)*, Oxford: Clarendon, 1984, vol. 1.

[10] R. A. Buckingham, *Proceedings of the Royal Society of London. Series A. Mathematical and Physical Sciences*, 1938, **168**, 264–283.

[11] H. C. Andersen, *J. Chem. Phys.*, 1980, **72**, 2384–2393.

[12] S. Nosé and M. Klein, *Mol. Phys.*, 1983, **50**, 1055–1076.

[13] S. Nosé, *J. Chem. Phys.*, 1984, **81**, 511–519.

[14] W. G. Hoover, *Phy. Rev. A*, 1985, **31**, 1695.

[15] M. Tuckerman, *Statistical mechanics: theory and molecular simulation*, Oxford university press, 2010.

[16] M. Born and R. Oppenheimer, *Ann. Phys.*, 1927, **389**, 457–484.

[17] R. M. Martin, *Electronic structure: basic theory and practical methods*, Cambridge university press, 2004.

[18] D. Marx and J. Hutter, *Ab initio molecular dynamics: basic theory and advanced methods*, Cambridge University Press, 2009.

[19] W. Kolos, *Adv. Quantum Chem.*, 1970, **5**, 99.

[20] W. Kutzelnigg, *Mol. Phys.*, 1997, **90**, 909–916.

[21] A. Szabo and N. S. Ostlund, *Modern quantum chemistry: introduction to advanced electronic structure theory*, Courier Corporation, 2012.

[22] R. McWeeny, *Methods of molecular quantum mechanics*, Academic press, 1992.

[23] R. G. Yang and W. Yang, *Density Functional Theory of Atoms and Molecules*, Oxford University Press, Oxford, 1989.

[24] R. M. Dreizler and E. K. Gross, *Density–Functional Theory*, Springer, 1990.

[25] H. Goldstein, C. P. Poole and J. L. Safko, *Classical Mechanics: Pearson New International Edition*, Pearson Higher Ed, 2014.

[26] H. Hellmann, *Z. Phys*, 1933, **85**, 180–190.

[27] R. P. Feynman, *Phys. Rev.*, 1939, **56**, 340.

[28] I. N. Levine, D. H. Busch and H. Shull, *Quantum chemistry*, Prentice Hall Upper Saddle River, NJ, 2000, vol. 5.

[29] N. March, *Adv. Phys.*, 1957, **6**, 1–101.

[30] T. D. Kühne, M. Krack, F. R. Mohamed and M. Parrinello, *Phys. Rev. Lett.*, 2007, **98**, 066401.

[31] K. Burke and L. O. Wagner, *Int. J. Quantum Chem*, 2013, **113**, 96–101.

[32] D. Hamann, M. Schlüter and C. Chiang, *Phys. Rev. Lett.*, 1979, **43**, 1494.

[33] D. Vanderbilt, *Phys. Rev. B*, 1990, **41**, 7892–7895.

[34] L. Kleinman, *Phys. Rev. Lett.*, 1982, **48**, 1425.

[35] A. Laio and M. Parrinello, *Proc. Natl. Acad. Sci. U.S.A*, 2002, **99**, 12562–12566.

[36] C. Micheletti, A. Laio and M. Parrinello, *Phys. Rev. Lett.*, 2004, **92**, 170601.

[37] G. Bussi, A. Laio and M. Parrinello, *Phys. Rev. Lett.*, 2006, **96**, 090601.

[38] A. Barducci, G. Bussi and M. Parrinello, *Phys. Rev. Lett.*, 2008, **100**, 020603.

[39] A. Laio and F. L. Gervasio, *Rep. Prog. Phys*, 2008, **71**, 126601.

[40] H. Jónsson, G. Mills and K. W. Jacobsen, 1998.

[41] G. Henkelman and H. Jónsson, *J. Chem. Phys.*, 2000, **113**, 9978–9985.

[42] G. Henkelman, B. P. Uberuaga and H. Jónsson, *J. Chem. Phys.*, 2000, **113**, 9901–9904.

CHAPTER 3

ROLE OF FRAMEWORK FLEXIBILITY ON ION TRANSPORT: MOLECULAR DYNAMICS STUDY OF $LiM_2(PO_4)_3$

3.1 Introduction

Since their inception in 1976 [1, 2] NASICON-type solids have attracted rigorous experimental and theoretical research. Detailed in chapter 1, along with various other inorganic Li^+/Na^+ conductors, the advances in the research and development of NASICON type materials have been discussed. This includes the wide range of cationic substitutions in the polyhedral framework [3], to efforts to device an *all*-NASICON battery [4]. Li substituted NASICONs, $LiM_2(PO_4)_3$, where M is Zr, Hf, Sn, Ti and Ge, have also gained wide spread attention over the years. The $LiTi_2(PO_4)_3$, which retains the rhombohedral structure at room temperature and exhibits high conductivity with aliovalent substitutions, faces the hurdle of reactivity with Li-anode [5, 6]. On the other hand, $LiZr_2(PO_4)_3$ shows better stability against Li-anode, but has a low conducting triclinic structure at room temperature [7]. The effect of different M-ions on the framework flexibility, and thus on the ionic conductivity is also a subject of interest for quite a long time. All these challenges and curious structural properties have kept the series exciting and worthy of active research [8, 9].

The present chapter details molecular dynamics (MD) study of the rhombohedral

Table 3.1: Inter-ionic potential parameters for different ion pairs

Species(X)	$\mathbf{q_x}$	$\sigma_\mathbf{x}$	$\mathbf{A_{xo}}$	$\mathbf{C_{xo}}$	$\mathbf{n_{xo}}$
Li	0.7020	0.86	0.1716	0	9
M = Zr	2.808	0.86	1.2126	11.917	9
M = Hf	2.808	0.85	1.2126	11.917	9
M = Sn	2.808	0.83	1.2126	11.917	9
M = Ti	2.808	0.745	1.2126	11.917	9
P	3.510	0.31	3.6158	9.279	9
O	-1.404	1.21	0.4484	47.999	7

A_{Na-Na}= 5 eV; n_{Na-Na}=11

phases of LiM$_2$(PO$_4$)$_3$, where M is Zr, Hf, Sn or Ti. The study examines the role of structural and dynamical correlations, between the mobile ion and the host lattice, on ion transport for different M-ion substitutions.

3.2 Simulation Details

The isobaric-isothermal (NPT) as well as microcanonical (NVE) molecular dynamics (MD) simulation has been carried out (using LAMMPS) [10] employing the Vashishta-Rahman form of the inter-atomic potential form [11].

$$V = \frac{1}{4\pi\epsilon_o}\frac{q_i q_j}{r_{ij}} + A_{ij}\frac{(\sigma_i+\sigma_j)^{n_{ij}}}{r_{ij}^{n_{ij}}} - \frac{C_{ij}}{r_{ij}^6} \tag{3.1}$$

where q_i is the charge and σ_i is the ionic radii of the i^{th} atom. A_{ij} and C_{ij} controls respectively the overlap-repulsive energy and dispersion energy between i^{th} and j^{th} atom respectively. The potential parameters are based on previous studies for the 'true' NASICON solid-solution, namely, Na$_{1+x}$Zr$_2$P$_{3-x}$Si$_x$O$_{12}$ [12, 13]. However, in view of the smaller Li radius the Li−Li and Li−O parameters are tuned to get the conductivity of LiZr$_2$(PO$_4$)$_3$ in agreement with the previously experimental reports [14–16]. Also, the A_{ij} for the O-O pair is slightly modified, as found required for the high temperature stability of the LiM$_2$(PO$_4$)$_3$ system. The ionic radii of the framework cations, M = Zr, Hf, Sn and Ti, are chosen from previous estimates [17]. The list of parameters used in the present study are listed in Table 4.1. The initial positions of the ions are taken from the XRD-studies on $LiZr_2(PO_4)_3$ by Petit *et al.* [15]. The initial cell parameters for the NPT-MD are chosen as $a = b = 8.847$ Å and $c = 22.24$ Å, and $\alpha = \beta = 90^o$ and $\gamma = 120^o$, as reported experimentally [15], for all the $LiM_2(PO_4)_3$ systems investigated. The simulation super cell consists of 3 × 3 × 1 unit cells, of rhombohedral ($R\bar{3}C$) symmetry, involving a total 972 atoms (54 Li, 108 M, 162 P and 648 O). Simulations on $LiZr_2(PO_4)_3$ employing larger supercell of 5 × 5 × 2 unit cells (consisting 5400 atoms) showed excellent convergence of structural and dynamical properties, confirming the adequacy of the system size. Periodic boundary conditions are imposed to eliminate the surface effect. The time step for the integration of the equation of motion is taken as 2 fs for all the simulations. Starting from the above mentioned cell parameters, 6 ns long NPT-MD simulations are performed for all four compositions. An initial 2 ns were dedicated for equilibration additionally, during which the atomic positions as well as the lattice parameters relax to thermodynamic equilibrium. Further, in order to demonstrate the role of framework flexibility on ion transport, 20 ns long microcanonical (NVE-MD) simulations are carried out at 1000 K on $LiZr_2(PO_4)_3$ with a frozen-in framework, that is, treating only Li^+ to have their degrees of freedom. The three natural choices of the rigid, frozen-in, frameworks considered are,

- the ideal (symmetry-imposed) structure with experimental lattice parameters as reported by Petit *et al* [15].
- ideal (symmetry-imposed) structure, but with the lattice parameters relaxed (based on their average from a well equilibrated NPT-MD simulations at 1000 K)
- an instantaneous framework structure (taken from a well equilibrated NPT-MD simulations at 1000 K, with the dynamical distortions of the framework frozen-in).

Comparison of ion transport in these frozen-in frameworks against the dynamical framework demonstrates the role of framework flexibility on ion transport.

3.3 Results and Discussions

Figure 3.1 shows a single unit cell of the Rhombohedral structure of $LiM_2(PO_4)_3$. The structure consists of corner shared $M-O_6$ octahedra and PO_4 tetrahedra. Each P-O tetrahedron is connected to four M-O octahedra and each M-O octahedron connected to six P-O tetrahedra, thus giving rise to a three-dimensional covalently bonded framework. This framework facilitate migration channels for small alkali ions, such as Li^+ and Na^+.

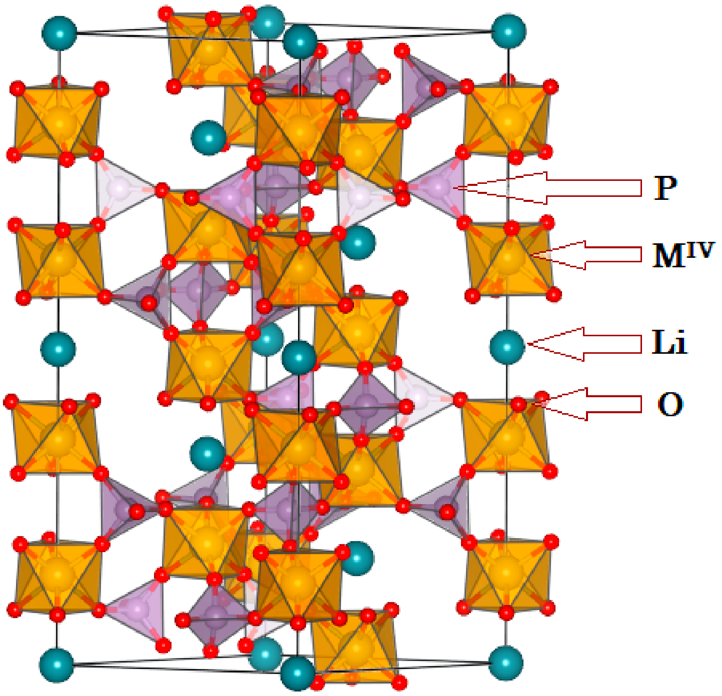

Figure 3.1: Single unit cell of LiM$_2$(PO$_4$)$_3$, where M = Zr, Hf, Sn and Ti.

Table 3.2: Bond length of different M-O pairs from NPT- MD simulations of LiM$_2$(PO$_4$)$_3$ at 500K

M	$M-O$ in Å(MD)	$M-O$ in Å(expt.)
Zr	2.06	2.06 [15]
Hf	2.05	2.029 [18]
Sn	2.02	-
Ti	1.93	1.94 [19]

To validate the proposed inter-atomic function, structural parameters, such as, the bond lengths, lattice parameters, radial distribution functions, etc. computed from the present MD simulations are compared with experimentally reported structure. The average M-O bond lengths (given in Table 3.2) show a systematic reduction with the size of the M ion. These are consistent with the experimental reports [15, 18, 19]. The average P-O bond lengths measures about 1.52 Åand the shortest O-O separation about 2.49 Å, for all the four systems, in agreement with the experimental values.

Table 3.3 lists the average lattice parameters of LiM$_2$(PO$_4$)$_3$ systems from the NPT-

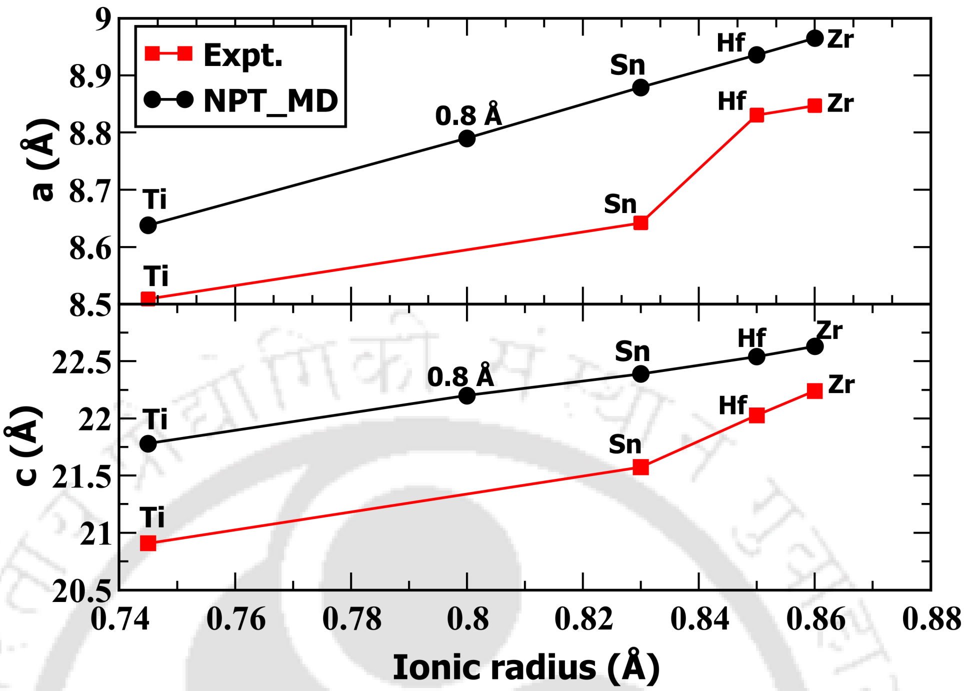

Figure 3.2: Change in lattice parameters as a function of M-ion radius, where M = Zr, Hf, Sn and Ti, at a temperature of 500K.

Table 3.3: Lattice parameters (in Å) of LiM$_2$(PO$_4$)$_3$ from NPT-MD simulations at 500K. The difference in the averaged cell angles α, β and γ were less than 0.03^o of their respective experimental values.

Material	Expt.	NPT-MD	Δ%
$LiZr_2P_3O_{12}$	$a = b = 8.84$, $c = 22.240$ [15]	$a = b = 8.96$, $c = 22.631$	1.35, 1.75
$LiHf_2P_3O_{12}$	$a = b = 8.83$, $c = 22.027$ [18]	$a = b = 8.93$, $c = 22.540$	1.13, 2.32
$LiSn_2P_3O_{12}$	$a = b = 8.64$, $c = 21.574$ [20]	$a = b = 8.87$ $c = 22.390$	2.66, 3.78
$LiTi_2P_3O_{12}$	$a = b = 8.50$, $c = 20.90$ [21]	$a = b = 8.63$, $c = 21.770$	1.52, 4.16

MD simulation at 500K along with the corresponding experimental reports for the rhombohedral phase. The average cell angles (not listed), α, β and γ were found to be well within 0.03^o of their respective values for the rhombohedral cell. Also, the a and c parameters when plotted against the M-ion radii (Figure 3.3) suggest monotonic increase, consistent with the experimental reports [15, 21, 22]. An additional data point, corresponding to a fictitious M-ion of radius 0.8 Å is examined, to bridge the relatively large gap in the ionic radii of Sn and Ti ions. The increasingly higher value of the lattice parameters down the series (especially the 'c' parameter) compared to the experimental

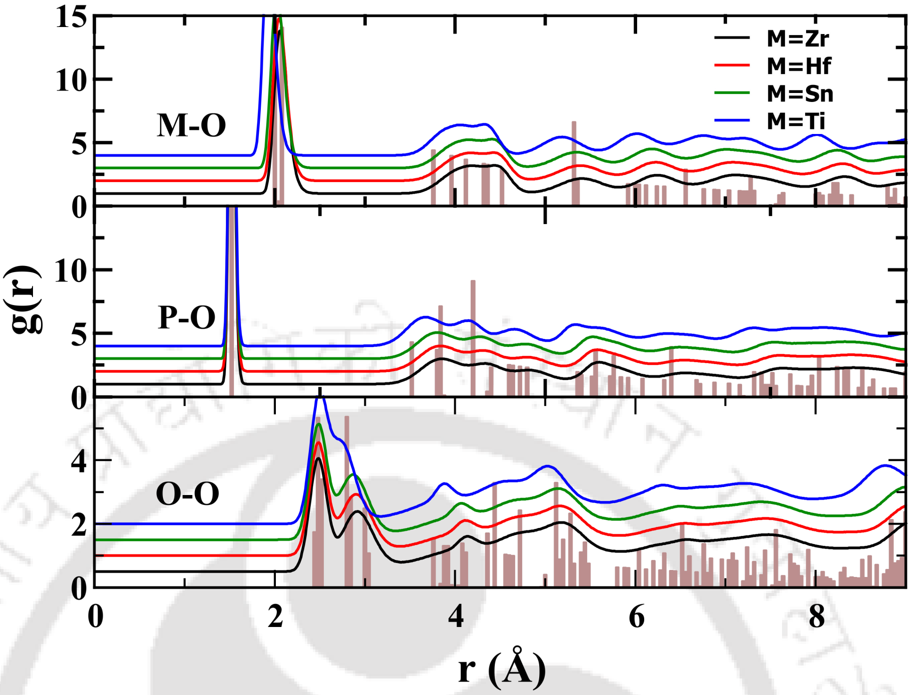

Figure 3.3: Radial distribution functions of selected ion pairs from NPT-MD simulations at 500 K. The functions are uniformly shifted along the y-axis for clarity. The vertical bars are the corresponding distributions based on the X-ray structure of the Zr system, on an arbitrary y-scale.

ones perhaps is the result of the deteriorating quality of the potential parameters, which were tuned for the 'Zr' case. It is interesting to note that the substitution of larger alkali ion, A, in $AZr_2(PO_4)_3$ though produces an increase in the c-parameter, the a-parameter was found to decreases in stark contrast with the present case of M substitution. This behavior was discussed in detail in one of previous simulation studies [23].

Shown in Figure 3.3 are the radial distribution functions (rdf) of M-O, P-O and O-O pairs for all the four systems, with Zr, Hf, Sn and Ti substituted at the M sites (see figure3.1) computed at 500K. The corresponding static rdfs based on the X-ray structure [15] are shown for $M = Zr$ case (as brown bars) for comparison. The stability of the framework structure, in all the four cases, are evident from the correspondence between the dynamic radial distribution functions with the static one. The broadening of the peaks in the dynamical rdf are due to the thermal vibration of the framework atoms about their equilibrium position. The reduction in M-O bond lengths with the size of the M ion are reflected in the radial distribution functions (shown in Figure 2). Even though the PO_4 tetrahedra are of nearly the same size the next neighbor distances of P-O and

O-O pairs reduce across the series, from Zr to Ti, due to the smaller size of the $M-O_6$ octahedron, and the reduction in the unit cell dimensions. These observations confirm the satisfactory reproduction of the structural stability of the simulated $LiM_2(PO_4)_3$ system.

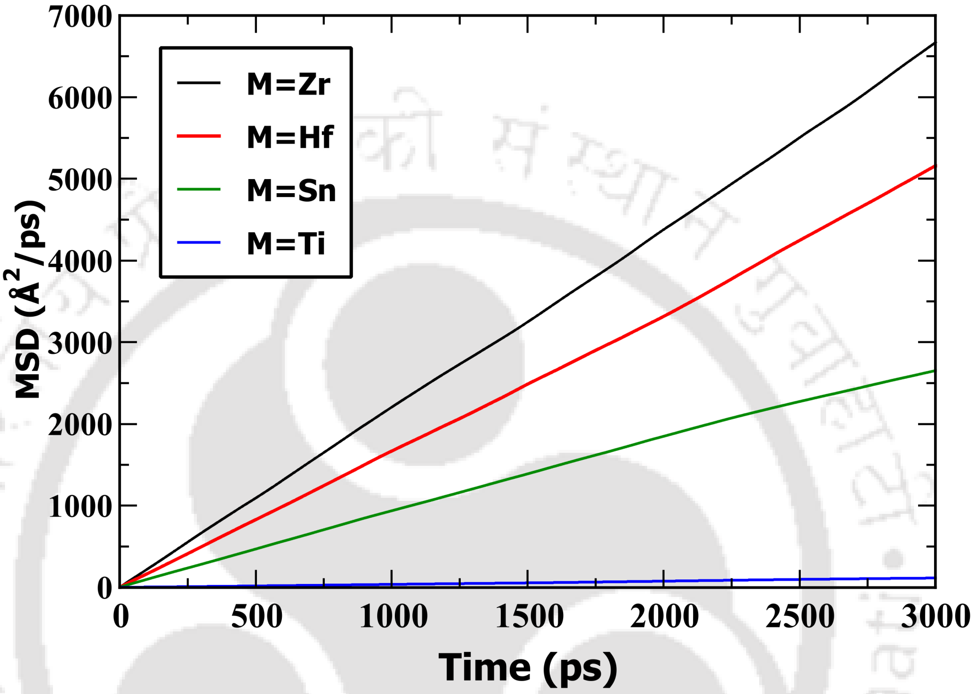

Figure 3.4: Mean square displacements of Li ions at 1000 K for $LiM_2(PO_4)_3$, where M = Zr, Hf, Sn and Ti.

Having confirmed the structural stability of the simulated systems, the dynamical properties related to the Li ion transport are examined. The mean square displacements (MSD) of Li-ion for the $LiM_2(PO_4)_3$ are calculated over the range of 700 − 1100K. Figure 3.4 shows the MSD at an elevated temperature of 1000 K. The self-diffusivities of the Li ions in these systems are deduced using Einstein's relation,

$$D = \lim_{t'\to\infty} \frac{<[\vec{r}(t+t') - \vec{r}(t)>}{6t'} \qquad (3.2)$$

As seen in Figure 3.4 the Li^+ diffusion is found to increases with the unit cell dimension, and is significantly higher in $LiZr_2(PO_4)_3$ compared to $LiTi_2(PO_4)_3$. This observation is in qualitative agreement with Martinez-Juarez *et al.* [22] There are some contradictions about this trend in the existing literature. Some experimental studies have reported higher Li conductivity for M = Ti, and attributed the behavior to an optimal cell volume for Li-ion transport [7, 24, 25]. However, the present simulations do

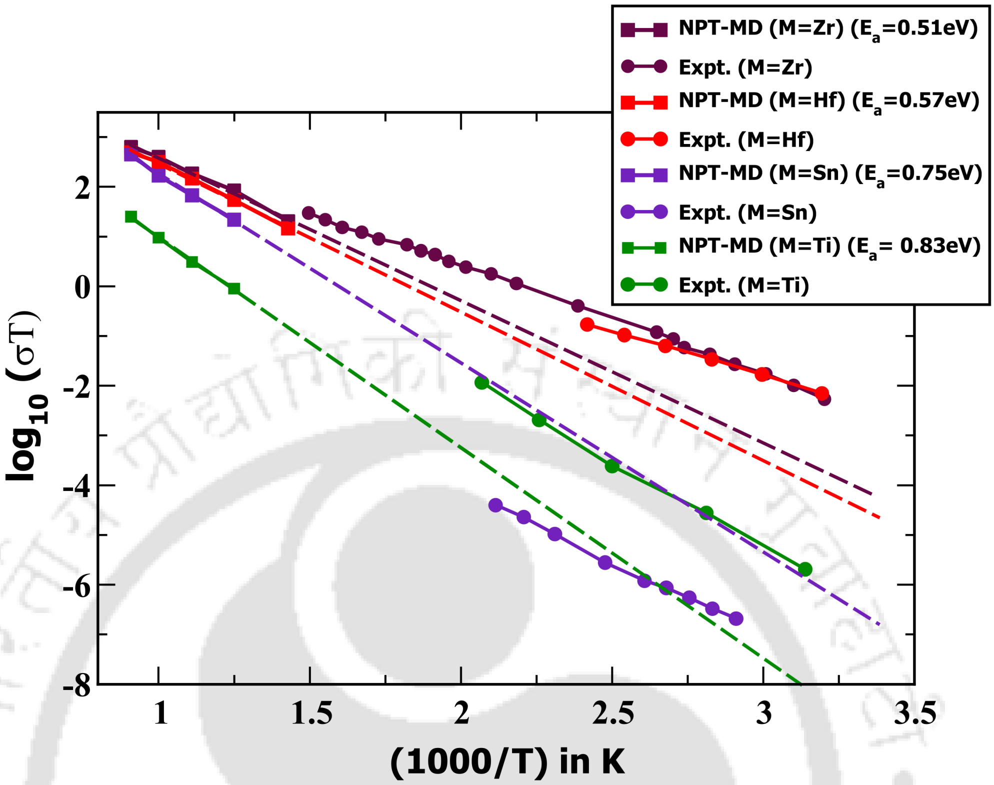

Figure 3.5: Arrhenius plot of Li$^+$ conductivity in LiM$_2$(PO$_4$)$_3$, where M = Zr, Hf, Sn and Ti. Previous experimental reports [16, 20–22] are also reproduced for comparison. The dashed lines are extrapolations to room temperature.

not support this observation. Figure 3.5 shows the plot of log(σT) versus 1000/T, where σ is the conductivity obtained from the Nernst-Einstein equation,

$$\sigma = \frac{nq^2D}{H_r k_B T} \tag{3.3}$$

where n is the number density of Li-ions, q is the electronic charge, k_B is the Boltzmann's constant, D is the self-diffusivity at temperature, T, and H_r is the Haven ration which is assumed to be unity. Previously reported experimental reports [16, 20–22] are also included in the plot. It shall be noted that our simulation could not probe for Li$^+$ transport at lower temperatures as over the length of the typical MD simulations (6 ns, in the present study) the Li-ions hardly make a successful jump to a nearby favorable site, on an average, leading to poor statistics in the estimation of self-diffusivity. A contradicting nature of trend in the conductivities for M = Sn, Ti systems between our simulation and available experimental reports [20, 21] is obvious from the Arrhenius plot (Figure 3.5). Due to the unavailability of other experimental reports on the Sn-system, we could not investigate this further.

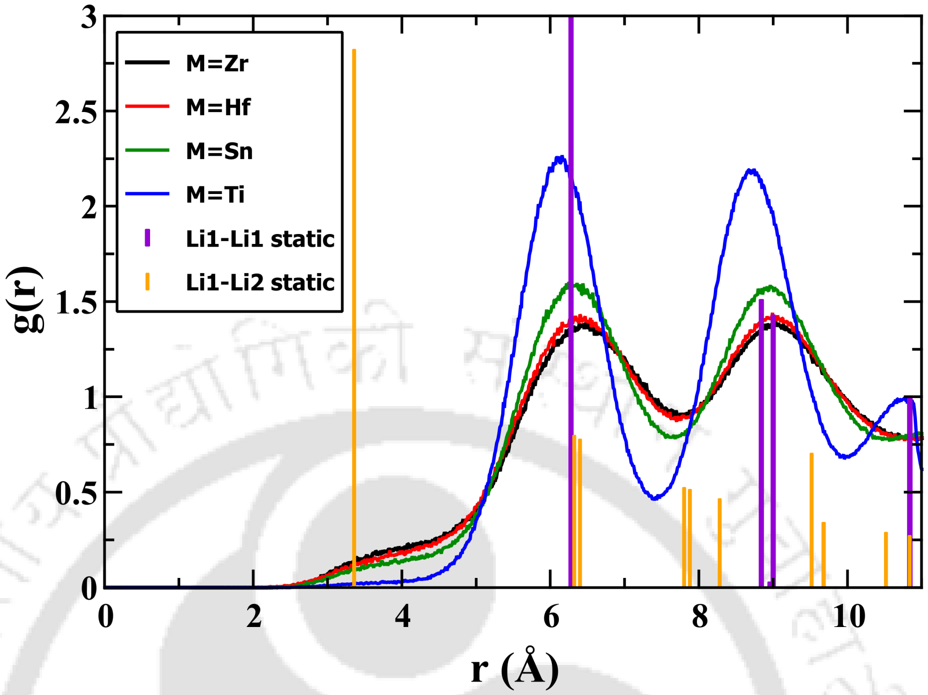

Figure 3.6: Li-Li dynamic radial distribution functions at 1000 K for LiM$_2$(PO$_4$)$_3$, where M = Zr, Hf, Sn and Ti. The vertical bars are the corresponding distributions of Li sites, on an arbitrary scale.

Atomic-scale insights:

Detailed analysis of the MD trajectories are carried out for better understanding of the Li transport in the system, and factors that influence it. Previous experimental [26] and simulation studies [13] have suggested three prominent sites for the mobile ions in the NASICON type structure, Li1 ($6b$ sites of $R\overline{3}c$), Li2 ($18e$) and $mid-Li$ ($36f$). Figure 3.6 shows the Li$-$Li dynamic radial distribution functions at 1000 K, along with the Li1-Li2 and Li1-Li2 static radial distribution functions, based on the X-ray structure of the Zr-system [15]. The first prominent peak of the dynamic rdf for all four cases are found to be at a distance of 6.3 Å. This corresponds to the distance of one Li1 site from another nearest Li1 site. The second prominent peak is at a distance of 9.1 Åwhich corresponds to the second nearest Li1 site. A relatively low intensity develops around the distance of 3.3 Å which corresponds to the Li1-Li2 nearest neighbor separation. This essentially signaling that a small population of Li ions are located at the Li2 sites. This is consistent with the fact that the conduction channel connects two neighboring Li1 sites through an Li2 site, as proposed in earlier studies on Na-NASICONs [12, 26–28]. It is evident that in all the four systems Li ions preferentially occupy the Li1 sites.

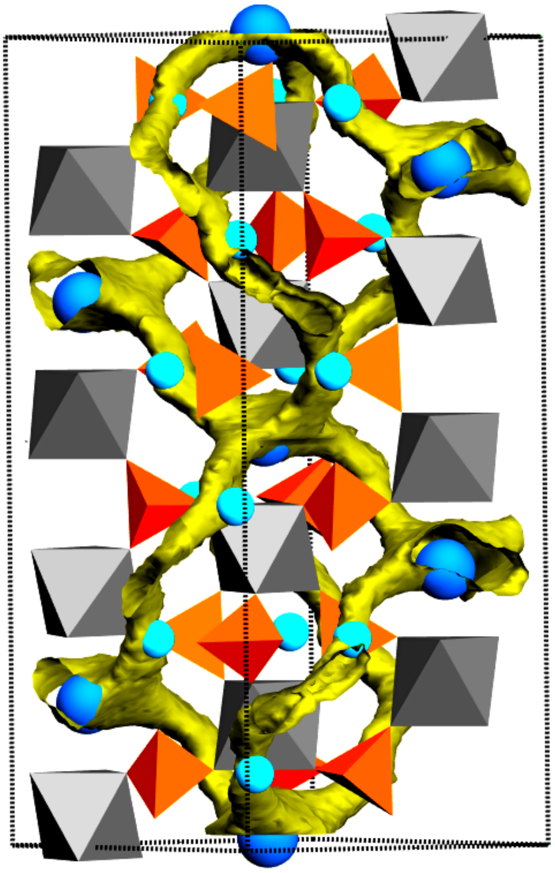

Figure 3.7: Three-dimensional diffusion pathway of Li ions in rhombohedral LiZr$_2$(PO$_4$)$_3$ from the present MD simulation at 1000 K. The large blue “balls” represent the Li1 sites, and the smaller balls in “cyan” are the Li2 sites.

Early literature also suggests that in pure LiM$_2$(PO$_4$)$_3$ structure the Li-ions tends to occupy the six coordinated Li1 sites [15, 29]. However, the Ti-system which measured significantly lower conductivity relative to the rest results more pronounced intensity at the Li1-Li2 distances, indicative of stronger Li localization at the Li1 site. Essentially, higher the diffusivity of the Li ions the more diffuse are the nature of the Li – Li rdfs. Three dimensional pathway of Li-ion transport through the LiM$_2$(PO$_4$)$_3$ framework is shown in Figure 3.7, taking the Zr system as a representative. This is generated by “folding back” all the coordinates of Li-ion spread across the simulation super cell into a single unit cell, and for the entire trajectory stored. As noted earlier, the Li diffusion channels connect the Li1 sites to a neighboring Li1 site through the Li2 sites. It shall be seen in Figure 3.7 that there are six conduction channels emerging from a given Li1 site (shown as blue balls) leading to six of its neighboring Li1 sites, through

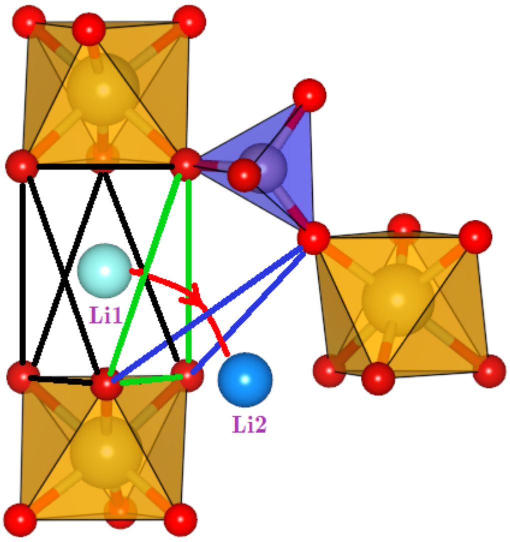

Figure 3.8: Schematic diagram showing the pathway of migration from Li1 to Li2. One pair of the bottlenecks,BN1 and BN2, are highlighted in green and blue respectively (see text for details).

Li2 sites (shown as cyan balls). Figure 3.8 shows an enlarged view of the framework around the Li1 and Li2 sites. The *oxygen* (red balls) forming the vortices of the six triangular faces of the Li_1-O_6 octahedra are marked by thicker lines. The six conduction channels emerging from a given Li1 site are through these triangular faces of the Li_1-O_6 octahedra. X-ray diffraction studies by Kohler and Schultz [28, 30] had proposed two geometrical bottlenecks for alkali ions in the Li1-Li2 migration channel. The first of this kind (referred to as BN1) are the six isosceles triangles of the Li_1-O_6 octahedra. The other bottleneck proposed, BN2, shares a common edge with the bottleneck BN1, and one vortex-oxygen from the neighboring $M-O_6$ octahedron. One pair of these bottlenecks, BN1 and BN2, are highlighted in figure 8 by blue lines. Some of earlier studies, both experimental and simulations [22, 31, 32], have attempted to understand the alkali ion transport in NASICONs based on the size of these two bottlenecks in the Li1-Li2 channel. We are discussing an in-depth analysis of the effect of these bottlenecks on the Li transport in $LiM_2(PO_4)_3$ for the rest of the discussion. Activation energy for Li ion transport in these systems is calculated from the slope of Arrhenius plots (Figure 3.5). The size of the bottlenecks (BN1 and BN2) are calculated as the radius of the circumcircle of the triangles made of *oxygens*. The variation of activation energy with the bottleneck size is shown in Figure 3.4. The radii of the bottlenecks, BN1 and BN2, in

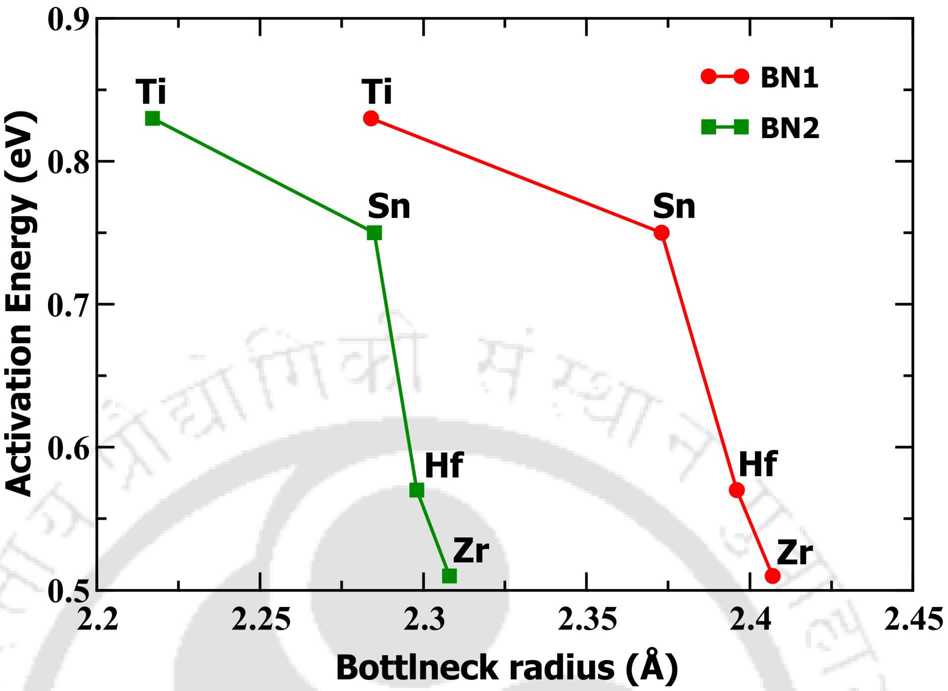

Figure 3.9: Variation of activation energy with bottleneck radii, BN1 and BN2, for different M ion sizes.

LiM$_2$(PO$_4$)$_3$ and the corresponding activation energies from the present MD simulations are listed in Table 3.4. The BN1 radii are well in agreement with previous report [22]. Experimental values of BN2 radii were not available in the literature. As expected, the Zr substituted system has the largest bottleneck radius by virtue of the larger Zr$-$O$_6$ octahedra, and results lower activation energy for Li transport. The size of the bottlenecks essentially reduces across the series, with Ti -system measuring the smallest. The present simulation results suggest a monotonic increase in activation energy with a decrease in the bottleneck size. A few studies in the past have drawn similar conclusions on the role of bottlenecks on the measured activation energies for ionic conduction [22, 31, 32]. It shall be noted that the experimental values of activation energies are somewhat scattered for these systems. The simulation results are agreeing with these only qualitatively. Figure 3.10 shows the potential energy profile of Li-ion from one Li1 site to a neighboring Li1 site at 1000 K for all four LiM$_2$(PO$_4$)$_3$ systems. The interesting fact is that the potential energy is highest around the Li2 site which is at around a distance of 3.3 Åfrom Li1 site. It supports the fact that the Li-ions tend to occupy the Li1 site as they are energetically most preferable, consistent with the Li$-$Li rdf discussed earlier. The M = Ti composition shows the highest potential energy barrier,

Table 3.4: Radii of bottleneck-1 (BN1) and bottleneck-2 (BN2) of the LiM$_2$(PO$_4$)$_3$ systems from present MD simulations. Also, the calculated activation energy for $Li+$ conduction is compared with available experimental reports.

M-ion radius(Å)	**BN1(Å)** NPT-MD	**BN2(Å)** NPT-MD	E_a**(eV) NPT-MD**	E_a**(eV) Expt.**
0.86 (Zr)	2.407	2.308	0.51	0.45 [14], 0.44[15]
0.85 (Hf)	2.396	2.298	0.57	0.44 [7, 33], 0.33 [22]
0.83 (Sn)	2.373	2.285	0.75	0.35 [22], 0.56 [34]
0.745 (Ti)	2.284	2.217	0.83	0.48 [22], 0.39 [25], 0.67 [21]

Figure 3.10: Potential energy profiles of Li ions as a function of distance between two Li1 sites at 1000 K for M = Zr, Hf, Sn and Ti.

in agreement with their lower Li$^+$ diffusivity. To summarize the key observations this far, it is concluded that unit cells as well as bottleneck radii decreases with size of the M-ion. The activation energy for conduction is found to increase with the decreasing bottleneck size, reducing the Li$^+$ diffusivity. It is however noted that the potential energy profile does not indicate any direct evidence of energetic bottlenecks at the locations where the geometrical bottlenecks are reported. Instead, the energy barrier that limits the mobility of the Li$^+$ ions is observed at the Li2 sites (3.3 Å). This is rather surprising, prompting us to investigate the role possible cooperative mechanism of Li ions with the geometrical bottlenecks, BN1 and BN2. Effect of framework dynamics on the mobility of Li-ion: In pursuit of the plausible correlation between the framework and mobile ions, the instantaneous dimensions of individual bottlenecks were calculated as a function of distance of the approaching Li-ion. Having known the triplets of oxygen forming the triangular bottlenecks, BN1 and BN2, their instantaneous radii are calculated as that of the circumcircle employing the entire trajectory from MD simulations at 1000 K. These instantaneous radii are plotted in figure 3.11 versus the distance (measured from the center for the respective bottlenecks) of an approaching Li$^+$ ion (essentially of the closest Li$^+$ under periodic boundary conditions).

It shall be noted in Figure 3.11 that, when the Li-ion is at large distance from the center of a bottleneck, the radius of the bottlenecks tend to converge to the statistically averaged values for the different M-systems as listed in Table 4. As the Li-ion comes

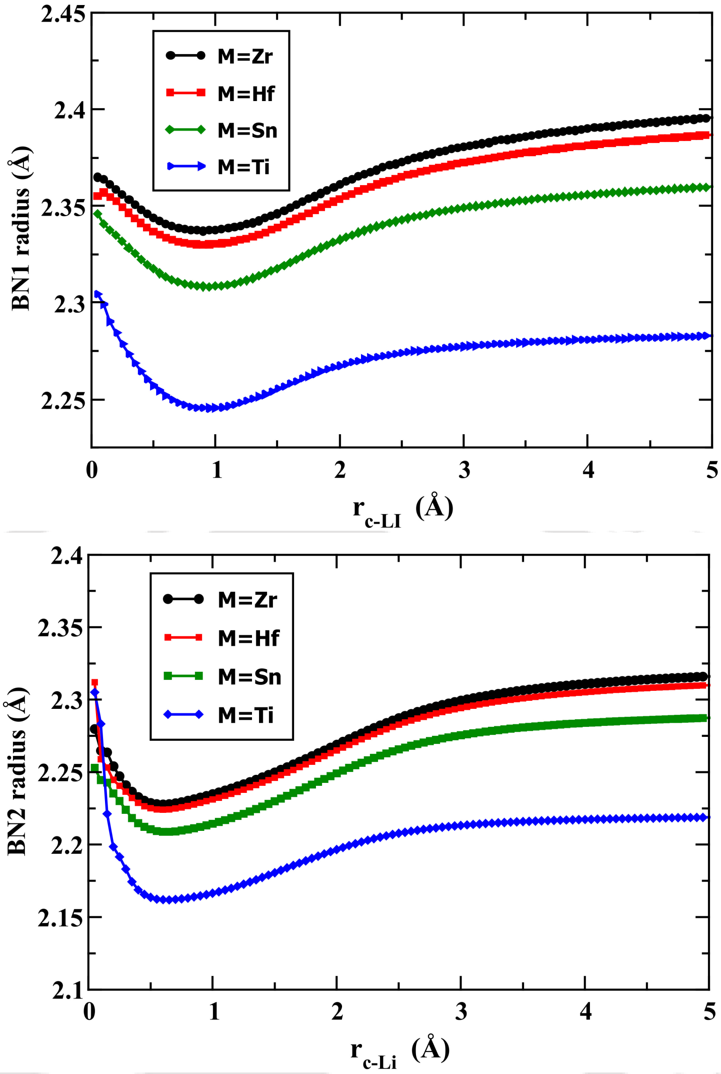

Figure 3.11: Instantaneous radii of the bottlenecks, BN1 (top panel) and BN2 (bottom panel), as a function of the distance to an approaching Li$^+$ ion for LiM$_2$(PO$_4$)$_3$ systems at 1000 K.

closer, initially the bottleneck radius decreases and then increases rather sharply as the ion is within about half an angstrom from the center of the bottlenecks. Having averaged over long MD trajectories, the smooth nature of the graph clearly establish that Li$^+$ motion is highly correlated with framework oxygen, that pronounces well above the thermal 'randomness' even at 1000 K. In order to understand further, the curious nature of this correlation, the Li – O distances are calculated, as where r_{BN} and r_{C-Li} are respectively the instantaneous bottleneck radii and distance of the Li$^+$ from the center of the bottlenecks (see schematic illustration in figure 3.12). The calculated Li – O distances for BN1 and BN2 are shown as insets in the Li – O rdf shown in Figure 3.13. The first

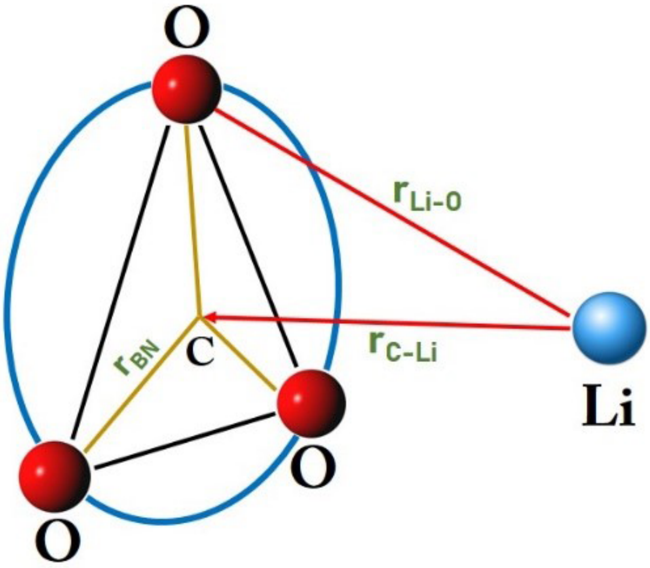

Figure 3.12: Schematic representation of the triangular bottleneck (black line) in the presence of an approaching Li^+ ion. The circumcircle (blue line), circumcenter, C, and other relevant distance of interest are marked (see text for details).

peak position of Li – O rdf for all four compositions, which signifies the most favorable distance between the Li^+ and oxygen of the framework measures around 2.20 – 2.25 Å. As seen in the inset figures, the Li – O distance estimated from the bottleneck analysis tend to converge to this favorable Li – O distance for all four cases. From this, the observed trend can be explained in terms of Li – O interaction. When Li^+ are at longer distances the bottleneck oxygen coming closer to their center helps reducing the Li – O distance towards their favorable distance. But as the Li^+ comes further close, the bottlenecks relaxes back to the favorable the Li – O distance (2.25 Å). Thus the framework oxygen, despite being part of a strong-covalent framework, is sensitive to the motion of the mobile ion. To examine the role of this correlated dynamics, between the Li^+ ion with the polyhedral framework of the NASICONs, on transport properties another set of NVE simulations has been carried out for 20 ns at 1000 K on $LiZr_2(PO_4)_3$ keeping the framework rigid. Li^+ motion is monitored under three different frozen models of the framework, as described in the method's section and the *msd* for each cases are shown in Figure 3.14. The frozen structure of $LiZr_2(PO_4)_3$ with experimental lattice parameter [15], marked 'XRD-lattice', shows practically no Li diffusion. The 'NPT-MD relaxed' structure which employs NPT-MD averaged lattice parameters at 1000 K shows Li^+ diffusion but several orders of magnitude lower than the standard dynamic framework

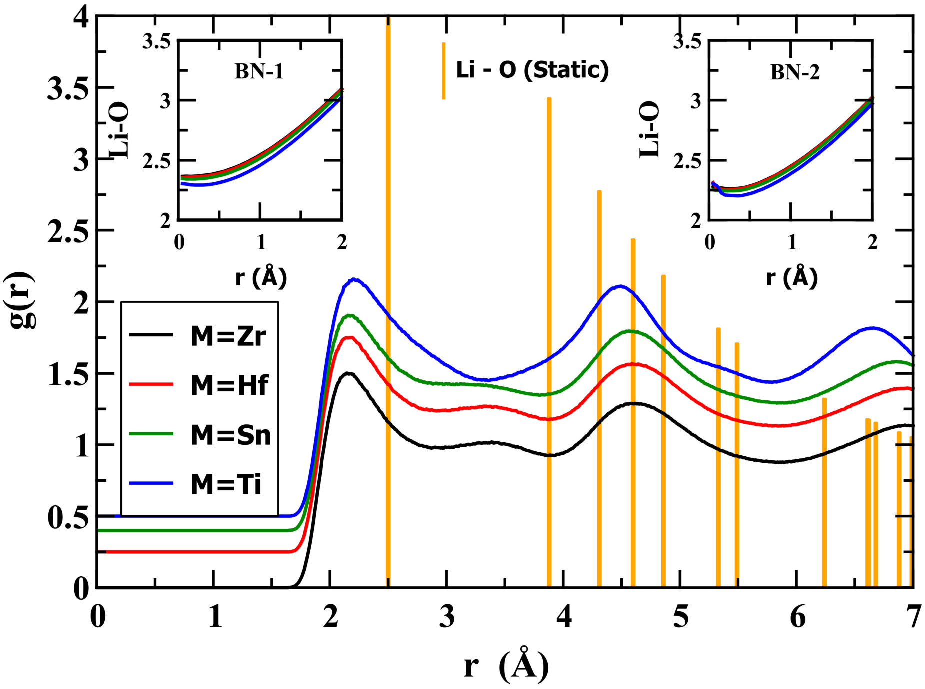

Figure 3.13: Li-O radial distribution function and Li-O distances calculated as a function of distance between Li and the center of the bottleneck at 1000 K. The vertical bars indicate the static Li-O radial distribution function calculated from the XRD structure for LiZr$_2$(PO$_4$)$_3$.

results shown in figure 3.4. For the dynamically distorted frozen framework, which is an instantaneous frame from an NPT-MD at 1000 K (marked 'Distorted Framework'), Li$^+$ diffusivity is intermediate. The relative difference in the Li$^+$ diffusivity across these three frozen framework is not significant here, rather what is important is the fact that these values orders of magnitude lower than the dynamic framework. This result indicates a strong influence of the framework motion on Li$^+$ mobility in these systems.

3.4 Conclusions

A series of classical molecular dynamics simulations in the isothermal-isobaric ensemble (NPT-MD) is carried on LiM$_2$(PO$_4$)$_3$, where M = Zr, Hf, Sn and Ti, primarily to investigate the Li$^+$ motion in these systems. It is noted that with the decrease in the ionic radii of the M-ion the a and c–lattice parameters of the rhombohedral cell decreases monotonically, in agreement with experimental reports. The decrease in lattice parameter results in a contraction of the geometrical bottlenecks for ion migration, previously identified based X-ray diffraction studies. The activation energy for conduction increases as the size of M-

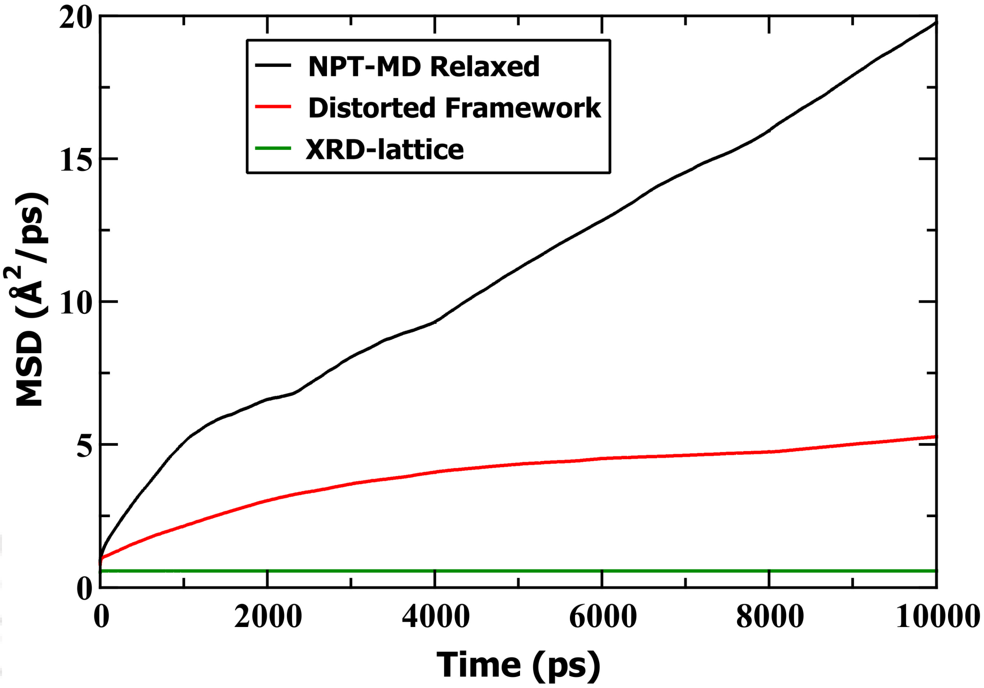

Figure 3.14: Mean square displacement of Li ions in $LiZr_2(PO_4)_3$ at 1000 K for frozen-in frameworks from three different initial structures.

ion decreases, and consequently the Li^+ diffusivity drops. Analysis of the potential energy landscape, however suggest that the rate-determining microscopic energy barrier for Li^+ migration do not correspond to the proposed bottlenecks, rather at the 18*e* Li sites of the rhombohedral structure. This prompted a closer examination of the proposed bottlenecks, to find that the triangular arrangement of oxygens forming the bottlenecks are very sensitive to an approaching Li^+. Depending on the distance to the approaching Li^+ ion, the bottlenecks dynamically shrinks or opens-up (around their respective statistically averaged dimensions in all of the substituted systems). This helps to improve the Li-O interaction favorably. Thus, the oxygens, despite being part of a strong covalently bonded ($P^{5+}-O^{2-}-M^{4+}$) framework, is sensitive to the Li^+ motion. Hence, it is concluded that ion transport in these solids involves correlated motion of the mobile species with the framework. In order to examine the role of this dynamical correlation on ion transport a series of microcanonical (NVE) molecular dynamics (MD) simulations has been carried out under frozen-in framework assumption. It is noted that Li^+ mobility in frozen-in frameworks are significantly lower (by more than three orders of magnitude) than that in the dynamical framework. This establishes, within the scope of the present model, that framework flexibility can be one of the key factors in facilitating fast ion transport, among other factors previously realized, such as, the availability of energetically favorable sites (in excess of the mobile species), and with low-barrier migration channels connecting them spanning the matrix, etc.

BIBLIOGRAPHY

[1] H.-P. Hong, *Mater. Res. Bull.*, 1976, **11**, 173–182.

[2] J. B. Goodenough, H.-P. Hong and J. Kafalas, *Mater. Res. Bull.*, 1976, **11**, 203–220.

[3] N. Anantharamulu, K. K. Rao, G. Rambabu, B. V. Kumar, V. Radha and M. Vithal, *J. Mater. Sci.*, 2011, **46**, 2821–2837.

[4] F. Lalère, J.-B. Leriche, M. Courty, S. Boulineau, V. Viallet, C. Masquelier and V. Seznec, *J. Power Sources*, 2014, **247**, 975–980.

[5] M. Kotobuki, Y. Suzuki, H. Munakata, K. Kanamura, Y. Sato, K. Yamamoto and T. Yoshida, *Electrochimica Acta*, 2011, **56**, 1023–1029.

[6] P. Knauth, *Solid State Ionics*, 2009, **180**, 911–916.

[7] M. Subramanian, R. Subramanian and A. Clearfield, *Solid State Ionics*, 1986, **18**, 562–569.

[8] E. Zhao, F. Ma, Y. Guo and Y. Jin, *RSC Adv.*, 2016, **6**, 92579–92585.

[9] H. Xie, J. B. Goodenough and Y. Li, *J. Power Sources*, 2011, **196**, 7760–7762.

[10] S. Plimpton, *Fast parallel algorithms for short-range molecular dynamics*, Sandia national labs., albuquerque, nm (united states) technical report, 1993.

[11] P. Vashishta and A. Rahman, *Phys. Rev. Lett.*, 1978, **40**, 1337.

[12] P. P. Kumar and S. Yashonath, *J. Phys. Chem. B*, 2002, **106**, 7081–7089.

[13] P. P. Kumar and S. Yashonath, *J. Am. Chem. Soc.*, 2002, **124**, 3828–3829.

[14] M. Barj, H. Perthuis and P. Colomban, *Solid State Ionics*, 1983, **9**, 845–850.

[15] D. Petit, P. Colomban, G. Collin and J. Boilot, *Mater. Res. Bull.*, 1986, **21**, 365–371.

[16] F. Sudreau, D. Petit and J. Boilot, *J. Solid State Chem.*, 1989, **83**, 78–90.

[17] J. E. Huheey, E. A. Keiter, R. L. Keiter and O. K. Medhi, *Inorg. Chem.: principles of structure and reactivity*, Pearson Education India, 2006.

[18] E. R. Losilla, M. A. Aranda, M. Martinez-Lara and S. Bruque, *Chem. Mater.*, 1997, **9**, 1678–1685.

[19] K. Arbi, M. Hoelzel, A. Kuhn, F. García-Alvarado and J. Sanz, *Inorg. Chem.*, 2013, **52**, 9290–9296.

[20] A. Martinez-Juarez, J. M. Rojo, J. E. Iglesias and J. Sanz, *Chem. Mater.*, 1995, **7**, 1857–1862.

[21] M. Pérez-Estébanez, J. Isasi-Marín, C. Díaz-Guerra, A. Rivera-Calzada, C. León and J. Santamaría, *Solid State Ionics*, 2013, **241**, 36–45.

[22] A. Martinez-Juarez, C. Pecharromán, J. E. Iglesias and J. M. Rojo, *J. Phys. Chem. B*, 1998, **102**, 372–375.

[23] S. Roy and P. P. Kumar, *J. Mater. Sci.*, 2012, **47**, 4946–4954.

[24] K. Takada, *Acta Mater.*, 2013, **61**, 759–770.

[25] J.-M. Winand, A. Rulmont and P. Tarte, *J. Solid State Chem.*, 1991, **93**, 341–349.

[26] J. Boilot, G. Collin and P. Colomban, *Mater. Res. Bull.*, 1987, **22**, 669–676.

[27] S. Roy and P. P. Kumar, *Phys. Chem. Chem. Phys.*, 2013, **15**, 4965–4969.

[28] H. Kohler and H. Schulz, *Mater. Res. Bull.*, 1985, **20**, 1461–1471.

[29] K. Arbi, M. Ayadi-Trabelsi and J. Sanz, *J. Mater. Chem.*, 2002, **12**, 2985–2990.

[30] H. Kohler and H. Schulz, *Mater. Res. Bull.*, 1986, **21**, 23–31.

[31] M. Guin and F. Tietz, *J. Power Sources*, 2015, **273**, 1056–1064.

[32] E. R. Losilla, M. A. Aranda, S. Bruque, M. A. Paris, J. Sanz and A. R. West, *Chem. Mater.*, 1998, **10**, 665–673.

[33] B. Taylor, A. English and T. Berzins, *Mater. Res. Bull.*, 1977, **12**, 171–181.

[34] A. Martinez-Juarez, R. Jimenez, P. Duran-Martin, J. Ibañez and J. M. Rojo, *J. Phys. Condens. Matter*, 1997, **9**, 4119.

CHAPTER 4

ACCESSING SLOW DIFFUSION IN SOLIDS EMPLOYING METADYNAMICS SIMULATION

4.1 Introduction

Molecular dynamics (MD) simulations comes in two flavours, namely classical and *ab-initio* [1–5]. In Chapter 2, the utility of these techniques has been discussed with the detailed descriptions of the theoretical background. One of the limitations of MD pertains to the time scales of simulations, and is particularly important in the study of slow processes or 'rare events'. Several methods have been proposed in the past to deal with such 'rare events' [6–12], and as already mentioned in chapter 2, originally proposed by Laio and Parrinello [13], metadynamics (MTD) is arguably one of the most promising approaches in this pursuit. Since its inception MTD approach has been successfully adapted to variety of problems of interest [14–22]. Consequently the technique has evolved, with several improvements and modifications, providing prescriptions for its optimal implementation, balancing both efficiency and accuracy [12, 23–30]. In the investigation of diffusion in condensed matter systems, since Jug *et al.* [31] examining oxide ion transport in rutile (TiO_2), a few studies have employed MTD technique, such as, proton transport in zirconia (ZrO_2) [32], Li transport in garnets ($Li_7La_3Zr_2O_{12}$) [33], Cu diffusion in CuZr-alloys [34], and molecular transport in porous organic network solids [35].

Table 4.1: Inter-ionic potential parameters for different ion pairs taken from previous study [39, 40]

Species(X)	$\mathbf{q}_x$	σ_x	$\mathbf{A}_{\mathbf{xo}}$	$\mathbf{C}_{\mathbf{xo}}$	$\mathbf{n}_{\mathbf{xo}}$
Na	0.7020	1.13	0.1716	0	9
Zr	2.808	0.86	1.2126	11.917	9
Si	2.808	0.40	2.8089	11.529	9
P	3.510	0.31	3.6158	9.217	9
O	-1.404	1.21	0.3252	47.999	7

A_{Na-Na}= 5 eV; n_{Na-Na}=11

The present chapter demonstrates a some-what different implementation of the technique, exploiting Na^+ transport in NASICONs [36, 37] as an example. As discussed in the introduction of the thesis, the intermediate composition of this solid solution with $x = 2$, $Na_3Zr_2Si_2PO_{12}$, exhibits very high Na^+ conductivity, and has been extensively studied, both experimentally as well as employing MD simulations. However, the two end members of the family, $NaZr_2(PO_4)_3$ and $Na_4Zr_2(SiO_4)_3$, exhibits much slower Na^+ diffusion with respect to time-scales of MD simulation, thus serving as good prototypical candidates for the present MTD calculations.

4.2 Simulation Details

Classical MD and MTD simulations on $NaZr_2(PO_4)_3$ and $Na_4Zr_2(SiO_4)_3$ are carried out in the canonical ensemble (NVT) at 500 K, employing the Vashishta-Rahman form of the interaction potential [38],

$$U(r_{ij}) = \frac{1}{4\pi\epsilon_0}\frac{q_i q_j}{r_{ij}} + \frac{A_{ij}(\sigma_i+\sigma_j)^{n_{ij}}}{r_{ij}^{n_{ij}}} - \frac{C_{ij}}{r_{ij}^6}, \tag{4.1}$$

where q_i and q_j are the partial charges, σ_i and σ_j are the ionic radius of i^{th} and j^{th} species respectively. A_{ij} and C_{ij} are respectively the overlap repulsive energy and dispersion energy between i^{th} and j^{th} ions. Listed in Table 4.1, the potential parameters employed are taken from a previous study by Kumar and Yashonath [39, 40].

The initial structure of the NASICONs are taken from the X-ray study of Boilot *et al.* [41]. The simulation box is made from 3 × 3 × 1 unit cells having rhomohedral ($R\bar{3}C$)

symmetry. The simulation super-cell thus includes a total of 972 ions (54-Na, 108-Zr, 162-P and 648-O) for $NaZr_2(PO_4)_3$ and 1134 ions (216-Na, 108-Zr, 162-P and 648-O) for $Na_4Zr_2(SiO_4)_3$. The initial X-ray structures [41] of both systems are relaxed under isothermal-isobaric (NPT) ensemble at 500 K. The dimension of the relaxed simulation box are $a = b = 26.989$ Å, $c = 22.672$ Å for $NaZr_2(PO_4)_3$ and $a = b = 27.680$ Å, $c = 22.379$ Å for $Na_4Zr_2(SiO_4)_3$. At an integration time-step of 2 fs, the production run for $NaZr_2(PO_4)_3$ was 100 ns long, while that for $Na_4Zr_2(SiO_4)_3$ was 200 ns long for better convergence of properties.

Molecular dynamics that powers the MTD calculation, is carried out employing the software LAMMPS (Large-scale Atomic/Molecular Massively Parallel Simulator) [42]. MTD simulation of the system is invoked by interfacing PLUMED [43] with LAMMPS. In chapter 2, a brief description on MTD is given. Now the specific details about the implementation of it in the current study shall be discussed. Our implementation of the techniques for the expedition of the ion transport process in the systems employs coordinates of a single, arbitrarily chosen, Na^+ ion, $\bar{r}_s = (x_s, y_s, z_s)$, as the 'collective variables' (CV). The net external potential imposed on this tagged ion or 'walker' at any instant, t, is the sum of the Gaussian 'hills' deposited at regular intervals (100 MD steps in the present work), during the period of $t = 0$ to $t = t'$, and is given by,

$$V(\bar{r}_s, t) = \sum_{t'}^{t' \leq t} H(t') \exp\left(-\frac{\left(\bar{r}_s(t) - \bar{r}_s(t')\right)^2}{2w^2} \right), \tag{4.2}$$

where w is the width of the Gaussian, kept constant at a value of 0.35 Å. $H(t')$ is the height of the Gaussian imposed at an MTD step, $t = t'$. In the 'well tempered' MTD formalism [25] the Gaussian heights are tuned as,

$$H(t') = H_0 \exp\left(-\frac{V(\bar{r}_s, t')}{k_B \Delta T} \right), \tag{4.3}$$

where T is the instantaneous temperature of the system, and $\Delta T = (\gamma - 1)T$. The initial height H_0 is chosen as 0.006 eV, and $\gamma = 6$ following Barducci *et al.* [25] However, to validate the choice of γ we have carried out additional runs – with $\gamma = 3$ and with $\gamma = 9$. These additional results are presented in the **Appendix A**.

Free Energy Calculation: One of the most useful information from MTD simulation is the mechanism of the process and its underlying free energy landscape. It shall be noted that the free energy of a 'process' (except for an *insignificant additive term* due to the reference state) as a function of CV (in the present case, the position of the tagged particle, $\bar{r}_s$), is given by [25],

$$F(\bar{r}_s) = -\lim_{t'\to\infty} \frac{T+\Delta T}{\Delta T} V(\bar{r}_s, t'). \tag{4.4}$$

In the present work the free energy profile for the Na^+ along the migration channel is calculated by mapping the $F(\bar{r}_s)$, as a function of the distance of the location, $\bar{r}_s$, with respect to *any two* of its nearest Na1-sites, λ, under periodic boundary conditions. Note that the mapping of the $F(\bar{r}_s)$, from space coordinates, $\bar{r}_s$, to $F(\lambda)$, is in the spirit of introducing a 'reaction coordinate', which reduces the dimensionality of the information, and helps to visualize the free energy profile along the migration channel.

Below we shall note certain technicalities of the mapping procedure:
The separation between two neighboring $Na1$ sites (~ 6.4 Å), is divided into fine bins (of size 0.1 Å). The distance $\bar{r}_{s1}(i) = \bar{r}_s - \bar{r}_1(i)$, where $\bar{r}_1(i)$ is the location of i^{th} $Na1$ site, is searched over all Na1 sites in the simulation cell. Whenever this distance is less than 6.4 Å under PBC, the $F(\bar{r}_s)$ is cumulated in an appropriate bin, say indexed j, which spans the reaction coordinate, λ. The quantity is then averaged over the counts registered in each bin. That is,

$$F(\lambda_j) = < F(PBC(\bar{r}_{s1}(i))) >_j, \qquad if \;\; \bar{r}_{s1}(i) < \; 6.4\mathring{A} \tag{4.5}$$

where $< \cdots >_j$ represent the average over the trajectory in a given bin j. It shall be noted that, the migration channel being the one connecting two neighboring $Na1$ (which shall be demonstrated in the later sections), for every hill-drop locations, $\bar{r}_s$, there would be two i values (that is, $Na1$ sites) which would meet the above criterion. It shall be remarked further that the above mapping procedure is not unique and any other method of *mining* the $F(\bar{r}_s)$ data onto repeating segments of trajectories may also be employed.

The free-energy profile from MTD simulation is compared with other compatible quantities, such as the potential energy profile of individual Na^+ ions, and potential energy barrier employing nudged-elastic-band (NEB) calculations, detailed as bellow:

1. The potential energy profile: the average potential energy of individual Na^+ ions at a given location, $\bar{r}_i$, due to *all* the rest of the ions in the system,

$$U(\bar{r}_i) = \sum_{j=1, j\neq i}^{N} U(\bar{r}_{ij}) \tag{4.6}$$

where N is the *total* number of ions (including mobile as well as those of the framework) in the system and $U(\bar{r}_{ij})$ is the pair-wise interaction potential as in eq. (4.1). The quantity, $U(\bar{r}_i)$, computed from the MTD trajectory, is mapped on to reaction coordinate, λ_i (under periodic boundary conditions), as discussed earlier. The $U(\lambda_i)$, thus calculated is averaged over all the Na^+ ions and over the entire MD trajectory.

2. From *climbing-image nudged elastic band* (CI-NEB) [44, 45] for a single Na^+ ion crossing over from one $Na1$ site to its neighbouring site.

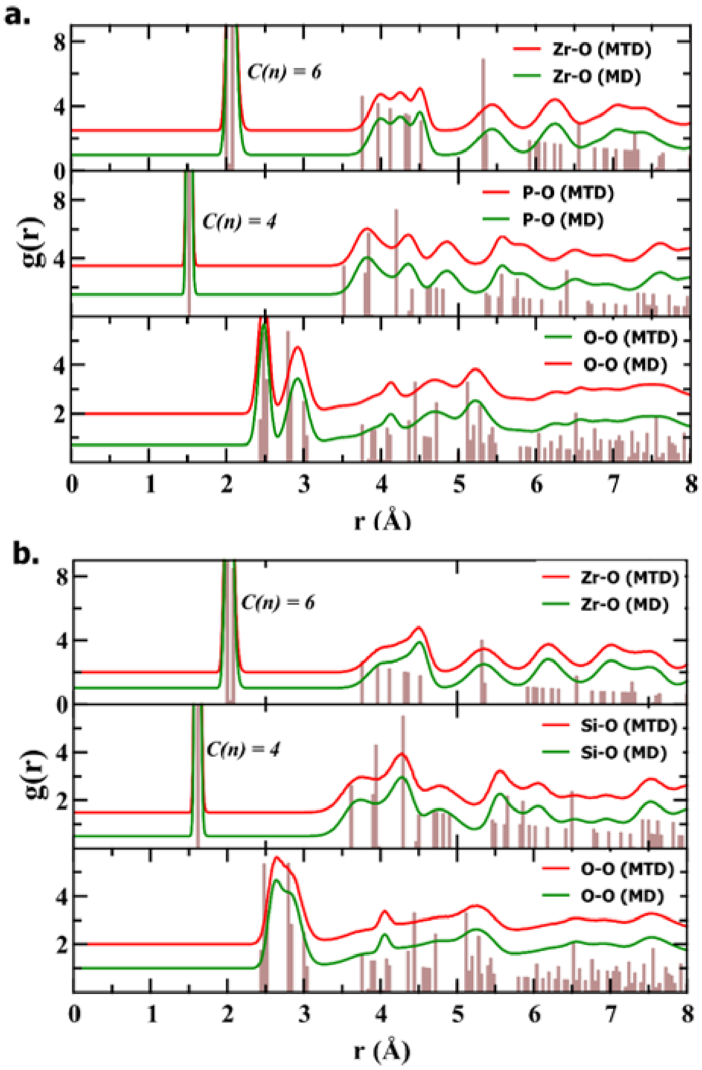

Figure 4.1: Dynamic RDFs (g(r)) of select ion pairs are shown along with that of the corresponding X-ray structure (bars) from both MTD and MD simulations at 500 K. Top panel: for $NaZr_2(PO_4)_3$. Bottom panel: for $Na_4Zr_2(SiO_4)_3$. The nearest-neighbour coordination numbers, C(n), of Zr-O, P-O, and Si-O are also marked in the respective, sub-panels. The plots are systematically shifted-up, along the y- axis, for clarity.

4.3 Results and Discussions

Structural stability: Radial distribution functions (RDFs) for Zr−O, P/Si−O, O−O pairs have been calculated to check the stability of the framework, during the MTD as well as MD simulations at 500 K. Figure 4.1 shows the dynamic RDFs for $NaZr_2(PO_4)_3$ (top panel) and $Na_4Zr_2(PO_4)_3$ (bottom panel), along with the corresponding static RDFs calculated from the X-ray structure.[41] The first peak positions of Zr−O are around 2.09 Å for both $NaZr_2(PO_4)_3$ and $Na_4Zr_2(SiO_4)_3$ systems. For the RDFs of P−O (top panel) and Si−O pairs (bottom panel) these are around 1.52 Å and 1.61 Å, respectively. These distances essentially corresponds to their respective bond lengths, and are in good agreement with experimental reports. [41, 46, 47] The nearest-neighbour coordination numbers, C(n), for Zr−O are 6, while that of P−O and Si−O are 4, as expected of the polyhedral structure of NASICONs involving ZrO_6 octahedra and $(P/Si)O_4$ tetrahedra. These observations confirms the structural stability of NASICON framework during MD and MTD simulation at 500 K. Having confirmed the structural stability, we shall demonstrate how the MTD simulations accelerate the ion transport facilitating access to relevant microscopic insights, where the standard MD fails. The results on NASICON systems, $NaZr_2(PO_4)_3$ and $Na_4Zr_2(SiO_4)_3$, chosen for these demonstrations shall be discussed separately in the next two sub-sections.

4.3.1 $NaZr_2(PO_4)_3$

Figure 4.2 (top) shows the distribution of Na^+ -ions in the simulation super-cell (consisting of 3 × 3 × 1 rhombohedral unit cells) sampled over 100 ns of standard MD simulations. Evidently, the Na^+ ions are exhibiting only thermal vibrations about their equilibrium positions without making any visible jump to neighbouring sites. Thus, weighed down by the timescale of ion hops the standard MD simulation does not yield any practical insights on the nature or mechanism of ions transport. On the other hand, the MTD trajectory of the 'tagged' Na^+ ion (Figure 4.2, bottom), on which the external potential has been applied, explores nearly the entire simulation cell gradually over the 100 ns of simulation. The external potential or 'hills', gradually deposited at locations, already visited by the ions, builds up over the period and compensates for the underlying local minimum enabling the ions to migrate to other favorable sites. A more quantitative measure of this 'accelerated dynamics' is presented in Figure 4.3, where the mean square

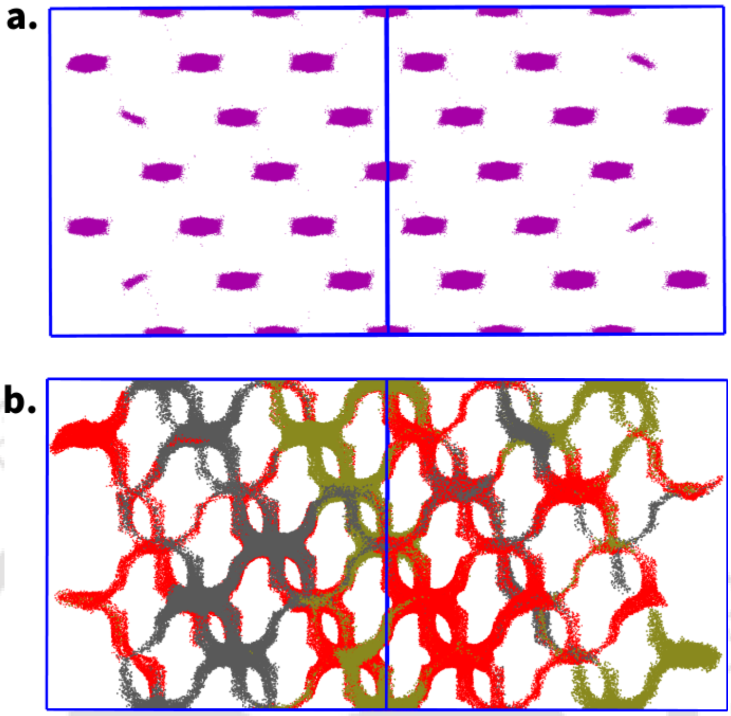

Figure 4.2: Top: Distribution of *all* the Na^+ -ions in the simulation super-cell sampled over 100 ns of standard MD simulations of $NaZr_2(PO_4)_3$ at 500 K. Bottom: Distribution of the single 'tagged' Na^+ ion in the system from 100 ns of MTD simulation at 500 K. The trajectory of the ion is shown in different colors to highlight the progress over time (olive green: 0-20 ns, gray: 20-40 ns, Red: 40-100 ns). The framework ions are not shown for the sake of clarity.

displacement (MSD) of Na^+ ions,

$$\text{MSD}(t) = \langle [\vec{r}(t) - \vec{r}(0)]^2 \rangle, \tag{4.7}$$

where $\vec{r}(t)$ is the position vector of an ion at time t, and $\langle \ldots \rangle$ indicate averaged over all ions of the same species and over several time-origins, are compared. However, to note a disadvantage, tough in typical MD studies the self-diffusion coefficient can be estimated directly, by the Einstein's relation, $D = \frac{MSD(t)}{6t}$, the same does not apply in MTD simulations as the process is 'artificially' accelerated.

The $Na^+ - Na^+$ RDF (Figure 4.4), calculated from the MTD trajectory, offer insights on the ion transport in the system. The first peaks of the RDF appears at around 6.3 Å which measures the distance between two neighbouring Na1 sites (6b positions of $R\bar{3}c$ space group). The second peak is at around 9.1 Å corresponds to the next-neighbour distance between two Na1 sites. This reflects the fact that in $NaZr_2(PO_4)_3$ all the Na^+ ions prefers to occupy the Na1 sites, and also the Na^+ hops occurs from one Na1 to the

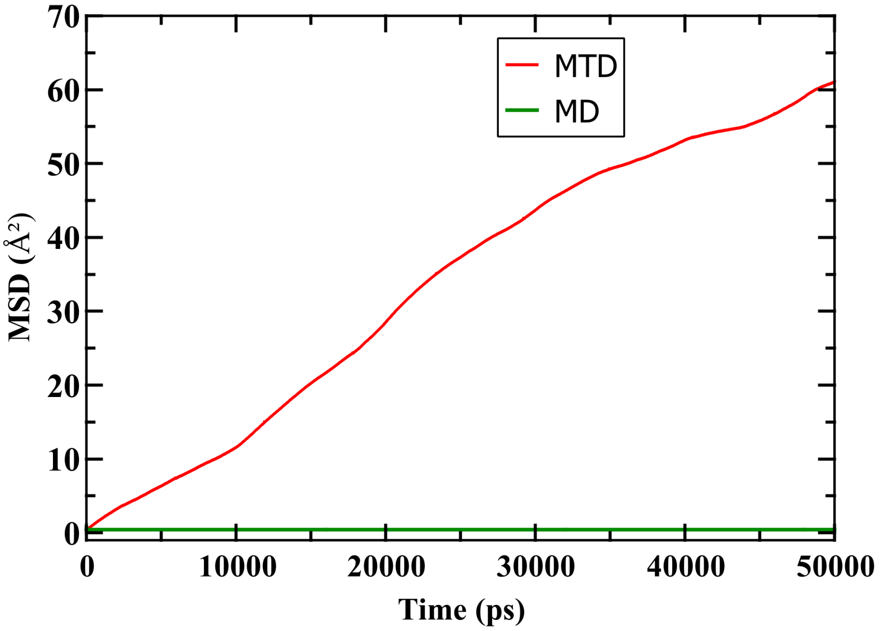

Figure 4.3: Mean squared displacement (MSD) of Na^+ ions, averaged over *all* Na^+ ions, from MTD and MD simulations of $NaZr_2(PO_4)_3$ at 500 K.

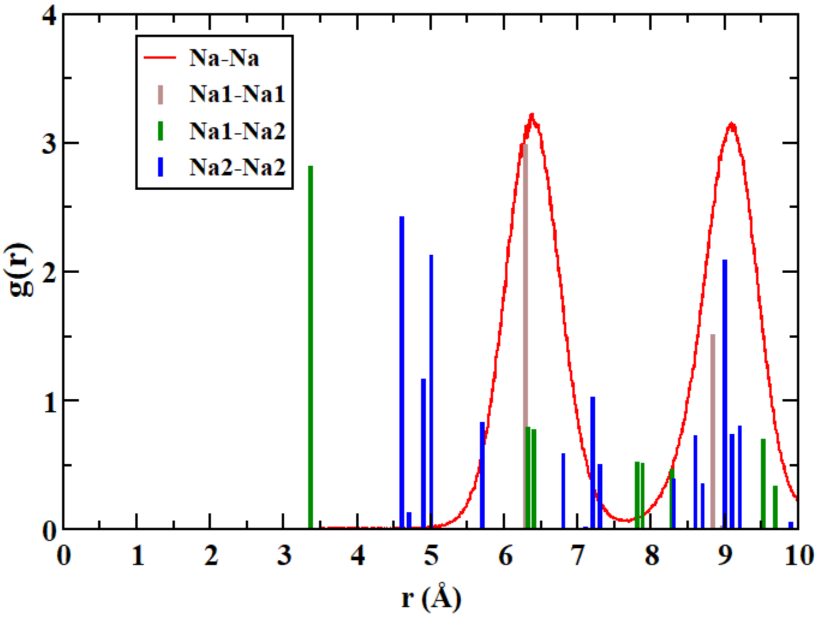

Figure 4.4: The radial distribution function (RDF) between the Na^+ ions calculated from MTD simulation of $NaZr_2(PO_4)_3$ at 500 K. The bars indicates the static RDF between Na1-Na1, Na1-Na2 and Na2-Na2 sites.

nearest Na1 site. Most experimental and computer simulation studies on this material have suggested this mechanism earlier [39–41, 48, 49].

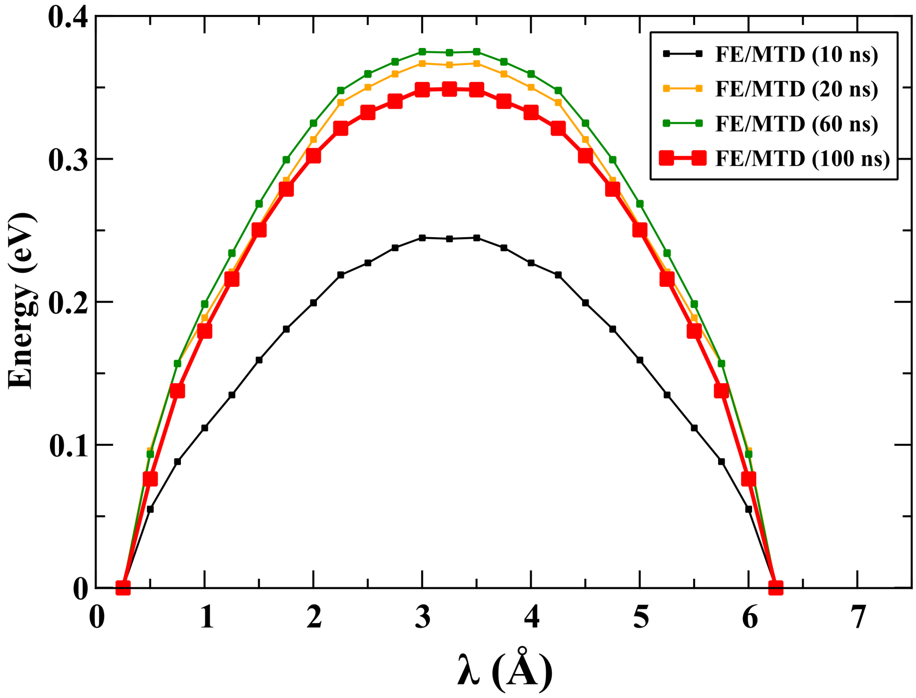

Figure 4.5: Evolution of the free energy profiles (calculated using (4.5)) as a function of λ, chosen as the reaction coordinate, during the MTD simulation of $NaZr_2(PO_4)_3$ at 500 K.

For better convergence of the free energy profile the 'tagged' particle need to sample a significant fraction of the individual local minima and the saddle points connecting them. For instance, in Figure 4.5, the free energy barrier measures 0.24 eV after 10 ns, while from 20 ns onward the barrier starts converging, and settles to the value of 0.34 eV over the period of 100 ns.

Figure 4.6 shows the free energy (Eqs. (4.4) and (4.5)) and potential energy profiles (Eq. (4.6)) calculated from the entire MTD trajectory of 100 ns, along with that from NEB calculations. The barriers calculated from different profiles show comparable values ranging between $\sim 0.35 - 0.4$ eV. It shall be noted that all the energy profiles indicates energy minimum at $Na1$ sites, and the saddle point is located at the $Na2$ site. This is in agreement with the Na^{+}-Na^{+} dynamic rdf shown in figure 4.4, that the Na^{+} ions preferentially occupy the $Na1$ sites $NaZr_2(PO_4)_3$. The calculated values of the microscopic barriers are also in good agreement previous studies [50, 51].

The ion migration channel connecting two $Na1$-sites and the built-up external potential along it is illustrated in Figure 4.7. The observed migration channel is consistent with the previous MD simulations on the high conducting $Na_3Zr_2Si_2PO_{12}$ system [40, 48, 49].

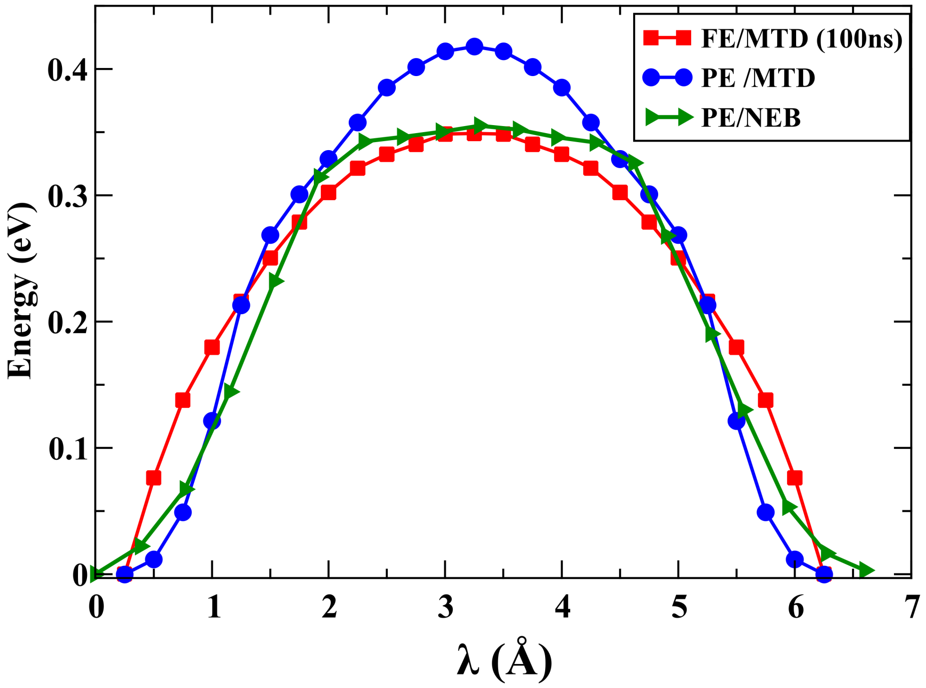

Figure 4.6: The converged free energy profile (FE) as a function of λ from 100 ns of MTD simulation of $NaZr_2(PO_4)_3$ is compared with the individual potential energy profile of Na^+ ions (averaged over all the ions and over the entire MTD trajectory), and with potential energy profile calculated from NEB calculated.

Figure 4.7(*left*) shows the minimum energy path (MEP) of Na^+ from one $Na1$-site to the neighbouring $Na1$ site obtained from the NEB calculation. This compares well with the profile of external potential deposited over the 100 ns long MTD run on select plane containing two neighbouring $Na1$-sites and the $Na2$-site in the channel, shown in Figure 4.7(right). It can be seen that the 'hills' are developed at the two energetically favorable $Na1$-sites, with a low-ridge connecting the two, depicting the migration channel. The nature of the channel is qualitatively very similar to that of the minimum energy path from NEB calculations, and the absence of any local maximum in the channel is indicative of fact that $Na2$-sites are energetically not favorable.

Having examined the utility of MTD simulations for ion transport in $NaZr_2(PO_4)_3$, we shall demonstrate the same for $Na_4Zr_2(SiO_4)_3$, where the results are less direct, or more intriguing on a primary inspection.

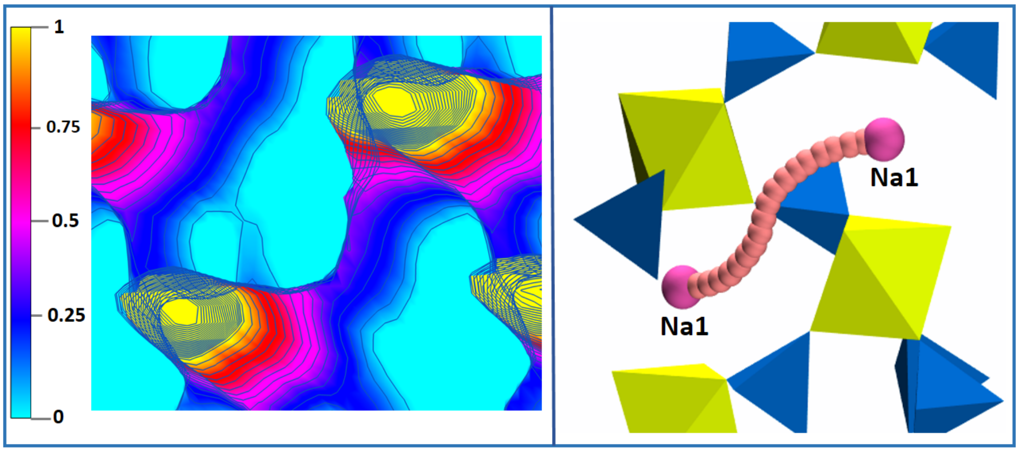

Figure 4.7: Left: The three dimensional distribution hills deposited between two $Na1$ sites over the MTD simulation of $NaZr_2(PO_4)_3$ at 500 K. The color-map (in arbitrary scale) helps to compare the relative intensities of regions. Right: The minimum energy path for Na^+ ion between two neighbouring $Na1$-sites calculated from NEB.

4.3.2 $Na_4Zr_2(SiO_4)_3$

The silicate end member of NASICONs, $Na_4Zr_2(SiO_4)_3$, shares the same structural feature as its phosphate counterpart, $NaZr_2(PO_4)_3$, discussed above. However, the former packs-up four times Na^+ ions in about the same volume. This high 'packing ratio' makes it much harder for the Na^+ ions move in the lattice. Figure 4.8 (top) shows the distribution of Na^+ ions in the simulation cell, consisting of $3 \times 3 \times 1$ rhombohedral unit cells, sampled from 100 ns of standard MD run. As in the previous case, standard MD simulations observe only the thermal vibrations of Na^+ about their equilibrium positions during the period. Thus the Na^+ transport remains inaccessible due to the long times scales of the process. Figure 4.8 (bottom) shows the MTD trajectory of the single Na^+ ion on which the external potential is applied. Due slower transport, the Na^+ ion could not explore the simulation box sufficiently during 100 ns of time (shown in red), initially dedicated. Hence, the simulation is continued for another 100 ns of MTD-simulation (shown in olive green). The mean squared displacement of Na^+ ions calculated from the MTD trajectory (averaged over *all* Na^+ ions and over several time-origins, as in the previous case) is presented in Figure 4.9.

Figure 4.10 shows the Na^+-Na^+ RDF calculated from MTD trajectory, along with the X-ray distributions of the sites, Na1-Na1 (brown), Na1-Na2 (green) and Na2-Na2 (blue). The first peak of the dynamic RDF corresponds to the Na1-Na2 distance (3.4 Å), the second peak to the Na2-Na2 distance (4.9 Å), and the third and fourth peaks

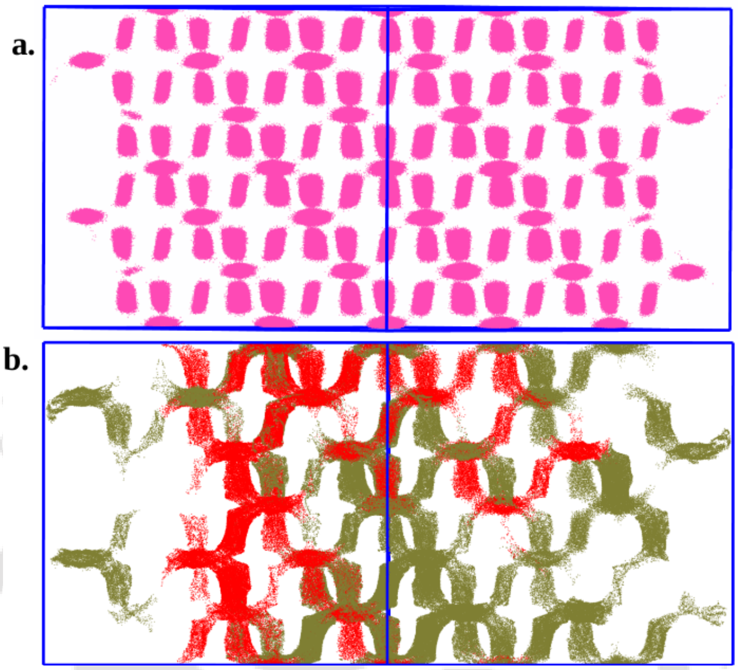

Figure 4.8: Top: Distribution of all the Na^+ ions in the simulation super-cell sampled from standard MD simulation of $Na_4Zr_2(SiO_4)_3$ at 500 K. Bottom: The progress of the tagged Na^+ ion in the super-cell during the MTD simulation of $Na_4Zr_2(SiO_4)_3$ at 500 K highlighted for first 100 ns in red, and that during the next 100-200 ns in olive green.

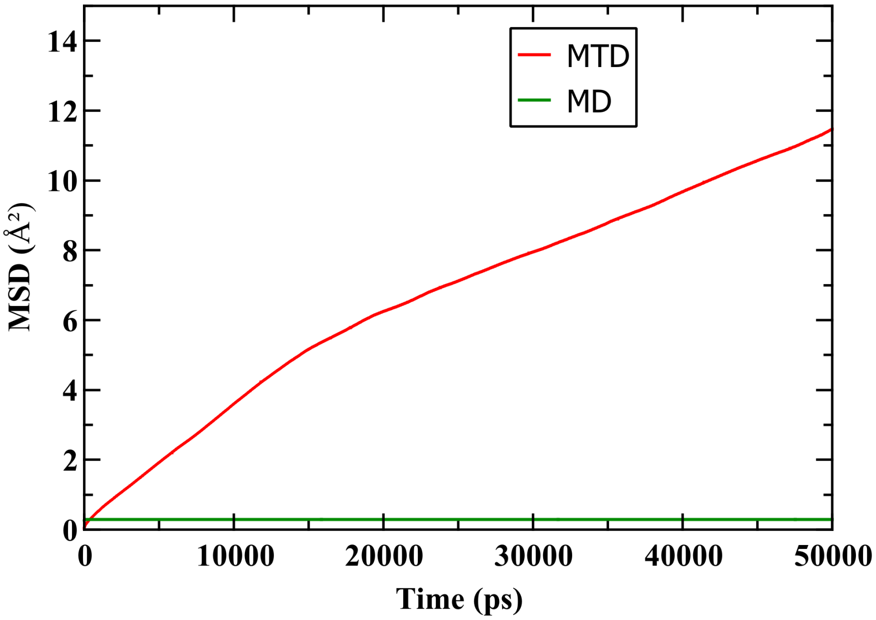

Figure 4.9: MSD of Na^+ ions from MTD and MD simulations of $Na_4Zr_2(SiO_4)_3$ at 500 K.

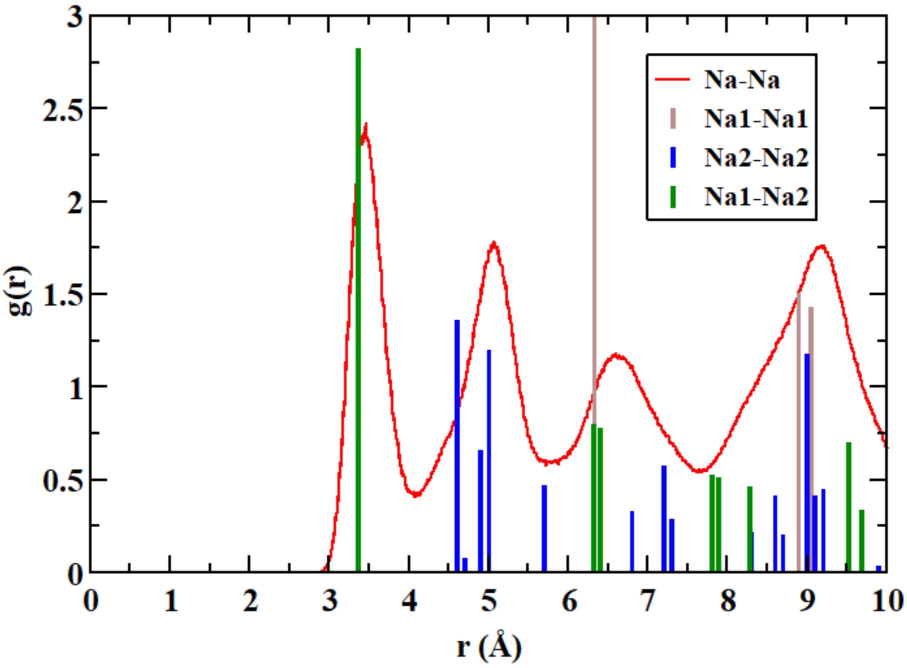

Figure 4.10: The Na^+-Na^+ RDF for $Na_4Zr_2(SiO_4)_3$ at 500 K, along with the distribution of Na sites (shown as bars) due the X-ray structure.

are respectively first and second Na1-Na1 neighbor distances. Thus, as required by the composition all the $Na1$ and $Na2$ sites remain occupied. The diffusion channel of Na^+ revealed by the MTD trajectory also remains the same, as the one connecting $Na1$-$Na2$-$Na1$-sites.

Calculation of the energy profile, F, for $Na_4Zr_2(SiO_4)_3$ has been carried out from the accumulated external potential in a similar fashion as in the previous case. The convergence of the profile (plotted as function of the reaction coordinate, λ_i) with the progress of the MTD run demonstrated in Figure 4.11. As seen, the profile significantly vary for run-lengths of 20 ns, 60 ns and 70 ns. For run-lengths 80 ns and larger, the profile starts converging measuring a barrier of about 0.34 eV. In Figure 4.12 the converged free energy profile, F, from MTD simulation is compared with the average potential energy profiles of individual Na^+ ions sampled from the MTD trajectory, and that from the Nudged Elastic Band (NEB) calculations. The NEB calculations are performed only between two neighboring $Na1$ and $Na2$ sites.

The free energy barriers for Na^+ transport in $Na_4Zr_2(SiO_4)_3$ is observed to be qualitatively different from that of $NaZr_2(PO_4)_3$ in Figure 4.5. Unlike in $NaZr_2(PO_4)_3$, the $Na2$-location is now a local minimum, with the peak of the profile shifting to, roughly,

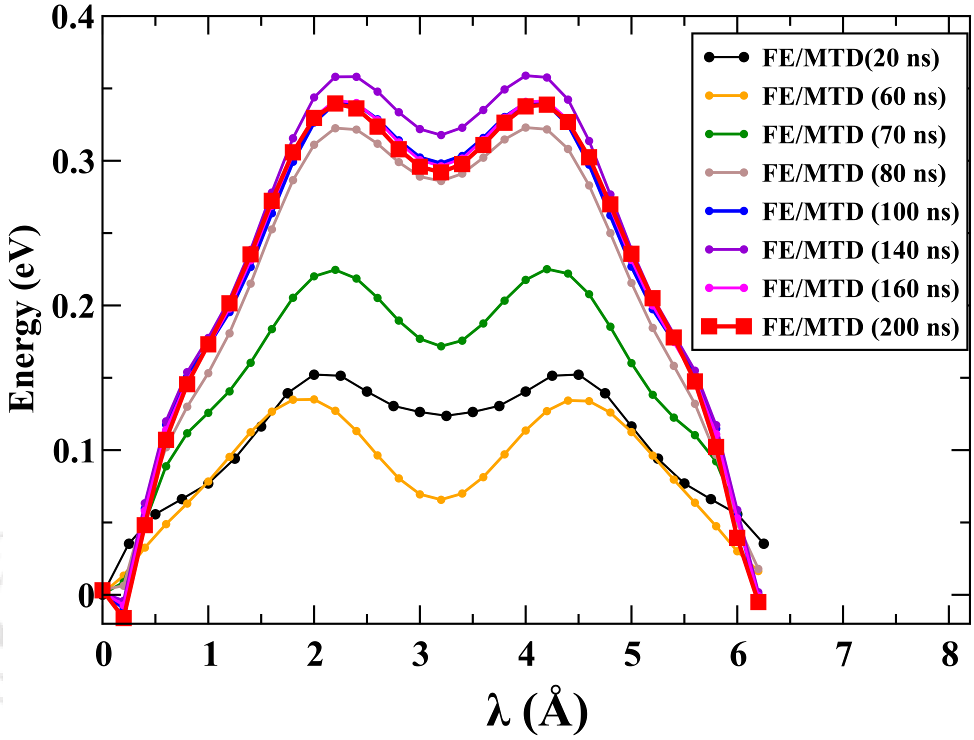

Figure 4.11: Convergence of the free energy profiles (calculated using (4.5)) during the progress of the 200 ns long MTD simulation of $Na_4Zr_2(SiO_4)_3$ at 500 K.

mid-way between the $Na1-Na2$ channel. The free energy barrier of 0.34 eV, from the MTD is in good agreement with experimental activation barrier of 0.347 eV by Tran Qui *et al.* [47].

The most intriguing aspect in Figure 4.12 is that the potential energy profiles of individual Na^+ ions, both from MTD and NEB calculations, are at sharp contrast to the free-energy profiles. The barrier heights of the potential energy profiles are about 0.15 eV which is much lower than the barrier obtained from the free energy profile (~ 0.34 eV) as well as with the experimental activation energy. This behaviour is attributed to the high degree of ion-ion correlation in the system. In the NASICON solid solution $Na_{1+x}Zr_2Si_xP_{3-x}O_{12}$ $(0 \leq x \leq 3.0)$ ion-ion correlations are expected to increase with the concentration of the mobile ions x. It shall be recalled that many studies in the past [41, 52, 53] have attributed the anomalously high conductivity of $Na_3Zr_2Si_2PO_{12}$ to an 'optimal' ion-ion correlation. From a contextual perspective, we shall note that the $Na_4Zr_2(SiO_4)_3$ system contains four times more Na^+ ions compared to $NaZr_2(PO_4)_3$, necessitating that all the $Na1$ and $Na2$-sites in the lattice be occupied. The migration channel in the structure being the one connecting $Na1-Na2-Na1$-sites [40, 48, 49],

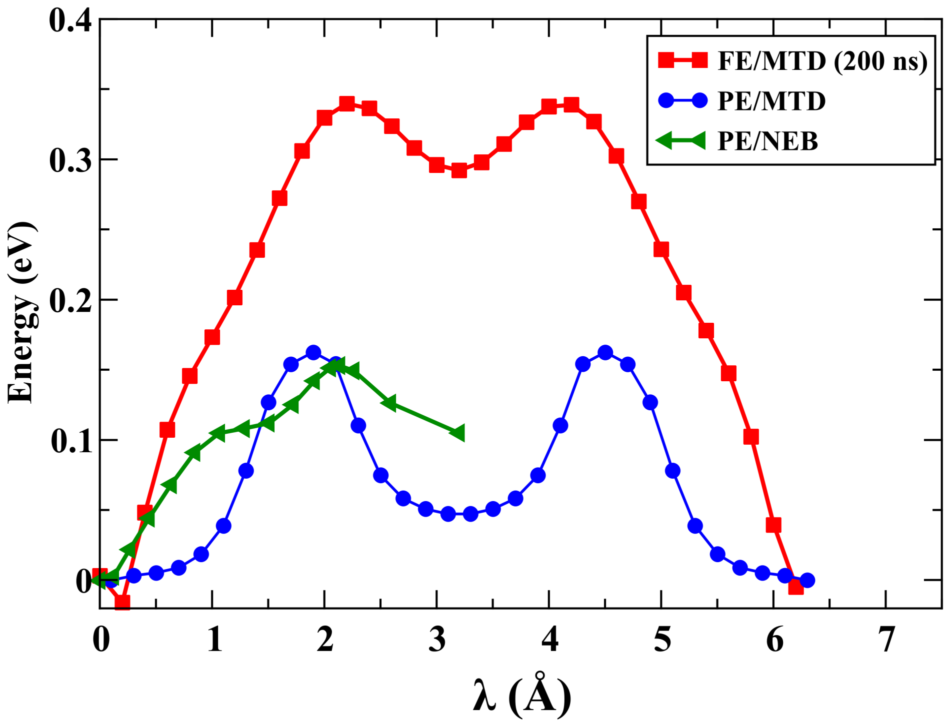

Figure 4.12: The converged free energy profile (FE) of Na^+ migration from 200 ns long MTD simulation of $Na_4Zr_2(SiO_4)_3$ is compared with the individual potential energy profile of Na^+ ions (from MTD trajectory), and that from the NEB calculation.

no Na^+ ions can jump to any of the neighbouring sites independently. Thus, it shall be inferred that the Na^+ transport in the framework involves *correlated* hops of multiple Na^+ ions.

In Figure A.1 (see **Appendix A**) the correlated hops of Na^+ ions are demonstrated using the trajectories of arbitrarily picked ions along with some of their neighbours. In MTD simulations, the tagged Na^+ ion (on which the external potential are imposed) propels all the participating Na^+ ions in this correlated motion, thus the 'total effective cost' of the event is reflected in F, while individual Na^+ ions experience only a 'fractional share' of it. Thus F is the more appropriate measure of the diffusion barrier.

Figure 4.13 demonstrates the MEP for Na^+ from one $Na1$-site to the neighbouring $Na2$ site obtained from the NEB calculation. This is compared with profile of external potential deposited over one segment of the of the conduction channel connecting $Na1-Na2-Na1$-sites. Like the previous case, two neighbouring $Na1$ sites develops maximum external potential, indicating the free-energy minima at $Na1$ sites. However, in contrast, for $Na_4Zr_2(SiO_4)_3$ system there is a local maximum of the external potential formed

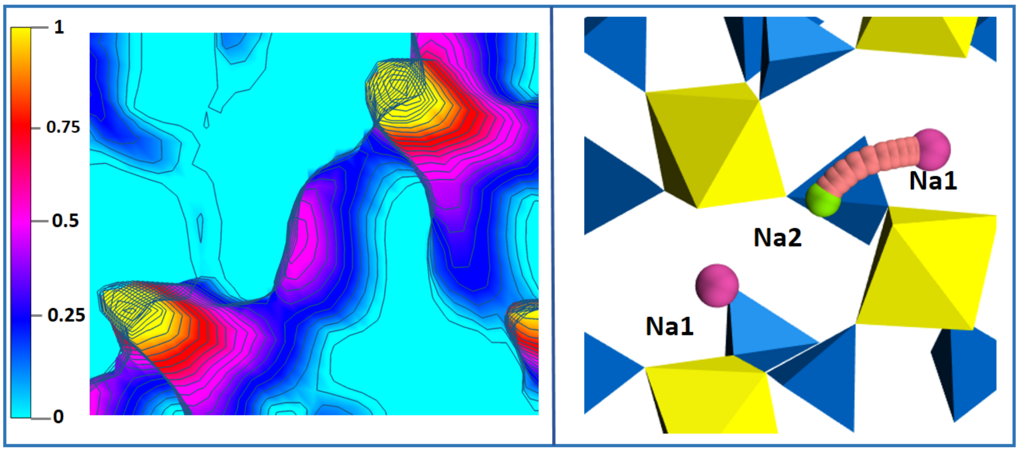

Figure 4.13: Left: Three dimensional map of hills deposited on the tagged Na^+)-ion in $Na_4Zr_2(SiO_4)_3$. The color-map (in arbitrary scale) helps to compare the relative intensities of regions. Right: the corresponding minimum energy path of Na^+ ion between two neighbouring $Na1$-$Na2$-sites obtained from NEB calculation.

between the two $Na1$-sites which corresponds to the local free-energy minima at $Na2$ site.

Before summarizing the results we shall briefly examine the results for different values of the bias factors, namely for $\gamma = 3$ and $\gamma = 9$, relative to $\gamma = 6$, for which the above results are discussed. It shall be noted in figure A.2 (see **Appendix A**) that for $\gamma = 3$ the tagged particle does not explore the configurational space efficiently. In $NaZr_2(PO_4)_3$, for $\gamma = 3$, the tagged particle makes several unsuccessful attempts to hop to its six neighbouring Na1 sites during the 100 ns of simulation, while for $Na_4Zr_2(SiO_4)_3$ the tagged ion successfully hops to one of its neighbouring Na1 sites, but fails to explore any further during the 200 ns of simulation. On the other hand, for bias factor $\gamma = 9$, visually the entire simulation cell is visited by the tagged ion in both the systems, as was the case for $\gamma = 6$.

Demonstrated in Figure A.3 (for $\gamma = 6$) (see **Appendix A**) is the fact that for large enough bias factor the tagged particle attempts several hops to neighbouring sites before being successful. As this process continues in each of the minima (Na-sites) encountered by the tagged ion, the corresponding wells gets filled out evenly by the dropped hills. However, for very large bias factors (not shown), say $\gamma = \infty$ (that is, with out the 'tuning' of the hills), the tagged ion explores the configuration space rather *too fast*, that is, without sampling the local minima sufficiently. This causes *uneven* filling of the minima causing larger errors in the free energy estimates. Thus, for an optimal range of γ values, the tagged ion samples the local minima fairly extensively, while also explores the rest of the accessible configuration space within affordable time scales. And as seen in Figure A.4 (see **Appendix A**) the resulting free energy profile for $\gamma = 9$ is very similar to that of $\gamma = 6$ for both the systems. Thus the choice of γ in the range of 6 to 9 for these systems seem adequate.

It is worthy of mentioning that although NEB is computationally less expensive than MD (more specifically in AIMD), and has been proven to be successful in estimating the migration barrier accurately for several classes of material [54], it has certain disadvantages. Firstly, prior knowledge of initial and final stages of migration is needed which can pose as an obstacle in finding new diffusion mechanisms. Secondly, the necessity of manual incorporation of vacancy for the diffusion species may appear as an artifice, and can effect the accuracy. Further, as noted in our study, for highly correlated motion of ions, MTD technique seems to predict the free energy surface more accurately. Incorporation of such correlation effect in NEB calculation is not straightforward [55]. Nevertheless, further studies would be required ascertain the above.

4.4 Conclusion

The general utility of metadynamics technique in accessing slow diffusion in solid electrolytes is explored for the prototypical phosphate and silicate end members of the 'true' NASICON solid solution, $Na_{1+x}Zr_2Si_xP_{3-x}O_{12}$ (where $0 \leq x \leq 3.0$). We shall note in passing that, in contrast to previous MTD implementations [31–35], where a distance measure from a select origin was chosen as the collective variable, the present simulation employs the Cartesian coordinates of a 'tagged' ion as the collective variables. However, without further investigations it is hard to compare the efficiencies of these two implementations.

The MTD method involves imposition of external Gaussian 'hills' on the tagged ion or the 'walker', at regular intervals following the well-tempered variant of the algorithm. As the hills starts filling out the local energy minimum the ion starts exploring other parts of the configurational space, resulting in the transport of ions across the matrix. The migration channel of the ions in the NASICON structure is found to be the one connecting $Na1-Na2-Na1$-sites, consistent with the previous MD simulations on the high conducting $Na_3Zr_2Si_2PO_{12}$ system. The hills imposed are reconstructed, and mapped on to the separation between two neighbouring Na^+ sites (namely, $Na1$ and

$Na2$) in the conduction channel, chosen as the 'reaction coordinate'. Thus, the microscopic free-energy profile of the ions in the migration channel is constructed. As demonstrated, for better convergence of the free-energy barrier the walker need to explore a significant fraction of the individual local minima and the saddle points connecting them.

In the phosphate end member, $NaZr_2(PO_4)_3$, the free energy profiles from MTD calculations are in agreement with the individual potential energy of ions and with nudged-elastic band (NEB) calculations. And the estimated barrier agrees well with the activation barrier reported in experiments. For the silicate end member, $Na_4Zr_2(SiO_4)_3$, the MTD free energy barrier remains in good agreement with experimental values, however quantitatively different from the potential energy profiles, from MTD as well as from NEB calculations. This has been attributed to the high-degree of correlated hops of Na^+ ions. The situation is analogous to a freight engine pulling several carriages over a mountainous terrine, wherein the engine (akin to the 'walker') accounts for the entire energy expended, while the work done by individual carries (akin to the other ions) measure only the fractional share of the gross.

Thus, the metadynamics approach facilitates investigation of the mechanism and microscopic energetics of diffusion in condensed phases, overcoming to a great extent, the time-scale limitations typical to atomistic simulation studies. We hope that the present study will further stimulate and guide metadynamics studies of atomic/molecular diffusion in condensed states of matter.

BIBLIOGRAPHY

[1] M. P. Allen and D. J. Tildesley, *Computer simulation of liquids*, Oxford university press, 2017.

[2] D. Frenkel and B. Smit, *Understanding molecular simulation: from algorithms to applications*, Elsevier, 2001, vol. 1.

[3] R. Car and M. Parrinello, *Phy. Rev. Lett.*, 1985, **55**, 2471.

[4] D. K. Remler and P. A. Madden, *Mol. Phys*, 1990, **70**, 921–966.

[5] D. Marx and J. Hutter, *Modern methods and algorithms of quantum chemistry*, 2000, **1**, 141.

[6] G. M. Torrie and J. P. Valleau, *J. Comput. Phys*, 1977, **23**, 187–199.

[7] H. Grubmüller, *Phys. Rev. E*, 1995, **52**, 2893.

[8] E. Darve and A. Pohorille, *J. Chem. Phys.*, 2001, **115**, 9169–9183.

[9] S. Park and K. Schulten, *J. Chem. Phys.*, 2004, **120**, 5946–5961.

[10] T. Huber, A. E. Torda and W. F. Van Gunsteren, *J. Comput. aid Mol. Des.*, 1994, **8**, 695–708.

[11] L. C. Pierce, P. R. Markwick, J. A. McCammon and N. L. Doltsinis, *J. Chem. Phys*, 2011, **134**, 174107.

[12] S. Awasthi and N. N. Nair, *Wiley Interdiscip. Rev. Comput. Mol. Sci*, 2019, **9**, e1398.

[13] A. Laio and M. Parrinello, *Proc. Natl. Acad. Sci. U.S.A*, 2002, **99**, 12562–12566.

[14] M. Iannuzzi, A. Laio and M. Parrinello, *Phys. Rev. Lett.*, 2003, **90**, 238302.

[15] A. Stirling, M. Iannuzzi, A. Laio and M. Parrinello, *ChemPhysChem*, 2004, **5**, 1558–1568.

[16] P. Raiteri, A. Laio, F. L. Gervasio, C. Micheletti and M. Parrinello, *J. Phys. Chem. B*, 2006, **110**, 3533–3539.

[17] C. Ceriani, A. Laio, E. Fois, A. Gamba, R. Martoňák and M. Parrinello, *Phys. Rev. B*, 2004, **70**, 113403.

[18] R. Martoňák, D. Donadio, A. R. Oganov and M. Parrinello, *Phys. Rev. B*, 2007, **76**, 014120.

[19] L.-M. Liu, A. Laio and A. Michaelides, *Phys. Chem. Chem. Phys.*, 2011, **13**, 13162–13166.

[20] J. Tóbik, R. Martoňák and V. Cambel, *Phys. Rev. B*, 2017, **96**, 140413.

[21] P. P. Kumar, A. G. Kalinichev and R. J. Kirkpatrick, *J. Chem. Phys*, 2007, **126**, 204315.

[22] N. N. Nair, E. Schreiner and D. Marx, *J. Am. Chem. Soc*, 2006, **128**, 13815–13826.

[23] C. Micheletti, A. Laio and M. Parrinello, *Phys. Rev. Lett.*, 2004, **92**, 170601.

[24] G. Bussi, A. Laio and M. Parrinello, *Phys. Rev. Lett.*, 2006, **96**, 090601.

[25] A. Barducci, G. Bussi and M. Parrinello, *Phys. Rev. Lett.*, 2008, **100**, 020603.

[26] G. Bussi and A. Laio, *Nat. Rev. Phys.*, 2020, 1–13.

[27] O. Valsson, P. Tiwary and M. Parrinello, *Annu. Rev. Phys. Chem*, 2016, **67**, 159–184.

[28] S. Awasthi, V. Kapil and N. N. Nair, *J. Comput. Chem*, 2016, **37**, 1413–1424.

[29] S. Awasthi and N. N. Nair, *J. Chem. Phys*, 2017, **146**, 094108.

[30] B. Ensing, M. De Vivo, Z. Liu, P. Moore and M. L. Klein, *Acc. Chem. Res*, 2006, **39**, 73–81.

[31] K. Jug, N. N. Nair and T. Bredow, *Physical Chemistry Chemical Physics*, 2005, **7**, 2616–2621.

[32] J. Rabone and P. Van Uffelen, *Journal of Nuclear Materials*, 2015, **459**, 30–36.

[33] K. Meier, T. Laino and A. Curioni, *The Journal of Physical Chemistry C*, 2014, **118**, 6668–6679.

[34] Y.-J. Wang, J.-P. Du, S. Shinzato, L.-H. Dai and S. Ogata, *Acta Materialia*, 2018, **157**, 165–173.

[35] E. Jackson, M. Miklitz, Q. Song, G. A. Tribello and K. E. Jelfs, *The Journal of Physical Chemistry C*, 2019, **123**, 21011–21021.

[36] H.-P. Hong, *Mater. Res. Bull.*, 1976, **11**, 173–182.

[37] J. B. Goodenough, H.-P. Hong and J. Kafalas, *Mater. Res. Bull.*, 1976, **11**, 203–220.

[38] P. Vashishta and A. Rahman, *Phys. Rev. Lett.*, 1978, **40**, 1337.

[39] P. P. Kumar and S. Yashonath, *J. Am. Chem. Soc*, 2002, **124**, 3828–3829.

[40] P. P. Kumar and S. Yashonath, *J. Phys. Chem. B*, 2002, **106**, 7081–7089.

[41] J.-P. Boilot, G. Collin and P. Colomban, *J. Solid State Chem.*, 1988, **73**, 160–171.

[42] S. Plimpton, *J. Comput. Phys*, 1995, **117**, 1–19.

[43] G. A. Tribello, M. Bonomi, D. Branduardi, C. Camilloni and G. Bussi, *Comput. Phys. Commun*, 2014, **185**, 604–613.

[44] G. Henkelman, B. P. Uberuaga and H. Jónsson, *J. Chem. Phys.*, 2000, **113**, 9901–9904.

[45] G. Henkelman and H. Jónsson, *J. Chem. Phys.*, 2000, **113**, 9978–9985.

[46] R. Hazen, L. Finger, D. K. Agrawal, H. McKinstry and A. J. Perrotta, *J. Mater. Res.*, 1987, **2**, 329–337.

[47] D. T. Qui, J. Capponi, M. Gondrand, M. Saib, J. Joubert and R. Shannon, *Solid State Ionics*, 1981, **3**, 219–222.

[48] S. Roy and P. P. Kumar, *Phys. Chem. Chem. Phys*, 2013, **15**, 4965–4969.

[49] K. Pramanik, K. Sau and P. P. Kumar, *J. Phys. Chem. C*, 2020, **124**, 4001–4009.

[50] Y. Miyajima, T. Miyoshi, J. Tamaki, M. Matsuoka, Y. Yamamoto, C. Masquelier, M. Tabuchi, Y. Saito and H. Kageyama, *Solid State Ionics*, 1999, **124**, 201–211.

[51] A. Ivanov-Schitz and A. Bykov, *Solid State Ionics*, 1997, **100**, 153–155.

[52] X. He, Y. Zhu and Y. Mo, *Nat. Commun*, 2017, **8**, 15893.

[53] Z. Zhang, Z. Zou, K. Kaup, R. Xiao, S. Shi, M. Avdeev, Y.-S. Hu, D. Wang, B. He, H. Li *et al.*, *Adv. Energy Mater.*, 2019, **9**, 1902373.

[54] F. Meutzner, T. Nestler, M. Zschornak, P. Canepa, G. Gautam, S. Leoni, S. Adams, T. Leisegang, V. Blatov and D. Meyer, *Phys. Sci. Rev.*, 2018, **4**, year.

[55] A. F. Harper, M. L. Evans, J. P. Darby, B. Karasulu, C. P. Koçer, J. Nelson and A. J. Morris, *Johnson Matthey Technol. Rev.*, 2020, **64**, 103–118.

CHAPTER 5

UNDERSTANDING Li^+-ION MIGRATION MECHANISM IN γ-LI$_3$PS$_4$: A FIRST PRINCIPLE BASED STUDY EMPLOYING METADYNAMICS AND *NEB*

5.1 Introduction

In the previous chapter, the utility of metadynamics technique in the study of ion transport in solids has been demonstrated on the NASICON end members. In this chapter, the application is extended to a different material, the low temperature γ-phase of Li_3PS_4, and the migration mechanism of Li^+ is explored. In the discussion of LISICON-type materials in chapter 1, it has been seen that Li_3PS_4 has different phases, namely γ, β, and α corresponds to the low (< 573 K), intermediate (> 573 K) and higher temperature (> 758 K) respectively [1]. The structures of α, β, and γ stabilizes in orthorhombic unit cell but with different space groups and can be differentiated from the arrangements of the $P-S_4$ tetrahedra [2, 3]. The γ-phase shows the lowest conductivity at room temperature (2.61×10^{-7} S/cm), the β-phase shows conductivity of 3.0×10^{-2} S/cm at 573 K but the extrapolated value shows conductivity of 8.93×10^{-7} S/cm at room temperature. Later Liu *et al.* [5] have synthesized nanoporous β-Li_3PS_4 by wet-chemical method and found three orders of magnitude enhancement of conductivity at room temperature (1.64×10^{-4} S/cm) and also good inter-facial stability against metallic lithium. The possible diffusion mechanisms in γ-Li_3PS_4 have been investigated in a couple of earlier studies employing nudged elastic band (NEB) method, along with other important aspects by implementing first principle approach [6, 7]. Also an *ab-inito* MD (AIMD) study at a elevated temperature of 800 K was reported for the γ-phase, but the migration mechanism was not discussed in the study [8]. The present chapter discusses detailed investigation of Li^+ migration mechanism in the low temperature γ-phase of Li$_3$PS$_4$.

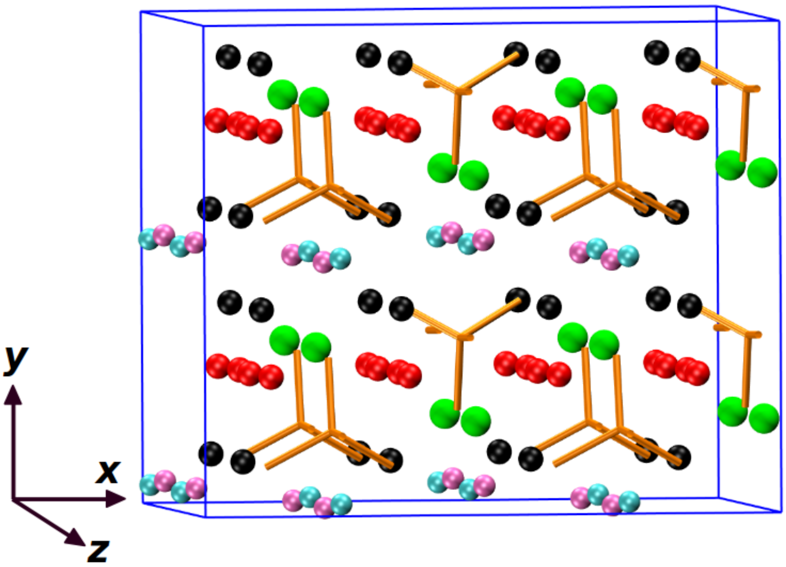

Figure 5.1: Orthorhombic simulation box consisting $2 \times 2 \times 2$ unit cells of γ-Li$_3$PS$_4$. The green balls represents the *'2a'* sites and the black balls represents *'4b'* sites, the red, mauve, and cyan balls represent the interstitial defect sites for Li^+-ions. The orange sticks represent the PS$_4$ tetrahedra.

5.2 Simulation Details

Ab-initio MD incorporated with well tempered metadynamics (MTD) is performed on γ-Li$_3$PS$_4$ at constant cell volume and at a temperature of 400 K using the open source package Quantum ESPRESSO [9–11]. For metadynamics implementation, PLUMED [12] is interfaced with Quantum ESPRESSO. The orthorhombic simulation box is created using $2 \times 2 \times 2$ unit cells with total 128 numbers of atom (48 Li, 16 P and 64 S) based on the X-ray structure reported by Homma et al [3]. The cell parameters are a = 15.636 Å, b = 13.220 Å, c = 12.408 Å and $\alpha = \beta = \gamma = 90^o$. Perdew-Burke-Ernzerhof (PBE) exchange correlation function is used. Optimized normconserving Vanderbilt (ONCV) pseudopotential is employed, and Kohn-Sham orbitals are expanded in plain wave basis with a cut-off of 60 Ry. The relaxed structure after energy minimization is used for the simulation. NVT-MD is carried out for 750 ps, with time steps of 2.0 fs. Well tempered MTD is implemented following the approach of the previous chapter, with initial hill height of 0.001 Ry, and the bias factor $\gamma = 8.0$. A constant hill width of 0.30 Bohr is used through out the simulation. The position of a single Li^+-ion (tagged Li^+) is chosen as the CV.

The overall free energy barrier is computed from the accumulated bias potential of the MTD simulation, as described in chapter 4. The energy barriers for the different pathways of Li^+-ion are also calculated using climbing image nudged elastic band method (CI-NEB) [13] as incorporated in Quantum ESPRESSO.

5.3 Results and Discussions

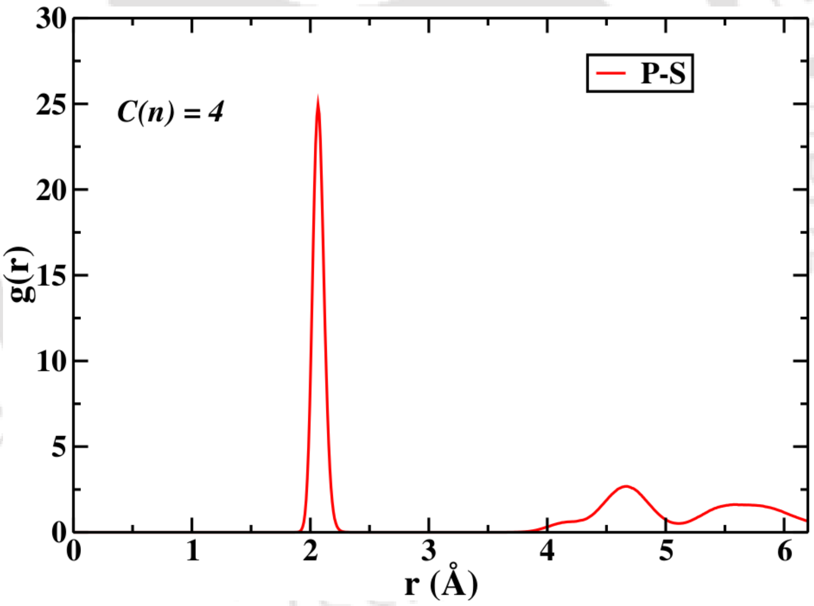

Figure 5.2: Radial distribution function (rdf) of P-S ion pairs calculated from the MTD simulation at 400 K.

One of the primary validations of a simulation is the structural integrity of the system and radial distribution function (RDF) is the general tool to check the same. Figure 5.2 shows the P-S dynamic RDF calculated and averaged over the entire length of the simulation. The first peak of the rdf appears to be at around 2.1 Å and reflects the average bond length of P-S pair which is well in agreement with the experimental

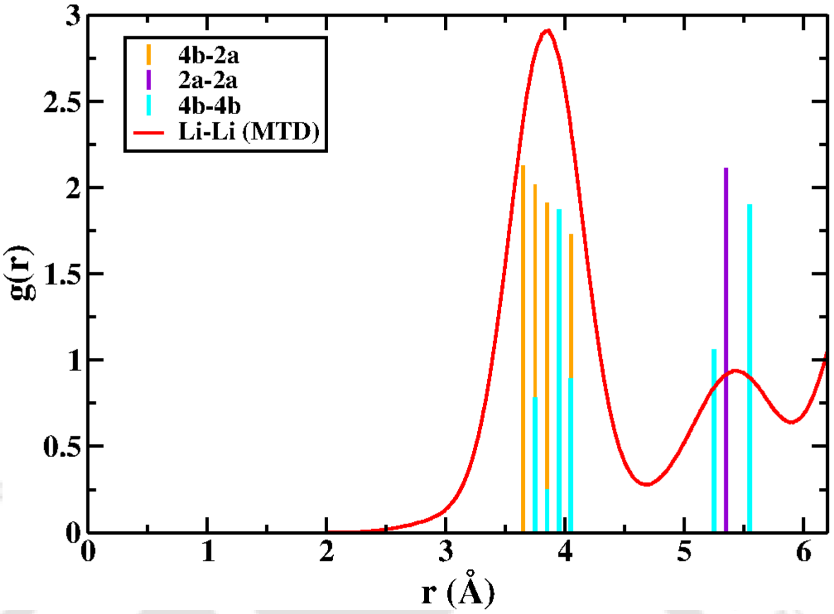

Figure 5.3: Radial distribution function (rdf) of Li^{+}-Li^{+}-ion pairs calculated from the MTD simulation at 400 K.

reports for γ-Li$_3$PS$_4$ [3]. The running coordination number (rcn), which gives the number of nearest neighbours, also found to be four. This confirms the integrity of the framework structure through out the run length of the MTD simulation.

Figure 5.3 shows the dynamic rdf of $Li^{+}-Li^{+}$ pair along with the static rdfs calculated for different static sites. The first peak of the dynamic rdf appears to be around 4.0 Å, which coincide with the static 4*b*-2*a* and 4*b*-4*b* peak. With the given structure, several different jumps are possible between these static Li^{+} sites. In the following section, different jumping mechanisms, responsible for the Li^{+}-ion migration are described by analysing the trajectory obtained from the MTD run.

A comparison of the efficiency of standard AIMD with MTD is shown in Figure5.4. Figure 5.4a shows the simulation box after 15 ps of standard AIMD simulation at 400 K. In this case, the Li^{+}-ions are exhibiting only thermal vibration around their mean positions without making any jump to the neighbouring sites. On the other hand, in case of the MTD simulation, in 15 ps the applied bias potential on a single Li^{+}-ion (tagged Li^{+}) has initiated diffusion mechanism at the same temperature (Figure 5.4b). Over the 750 ps of MTD, the tagged Li^{+} is found to explore a large fraction of the simulation box (Figure 5.4c). Shown in figure (5.4d), the diffusion of the tagged Li^{+} has eventually caused movement of the other Li^{+}-ions in the system as well, and consequently well connected diffusion pathways of the Li^{+}-ions across the simulation box emerges.

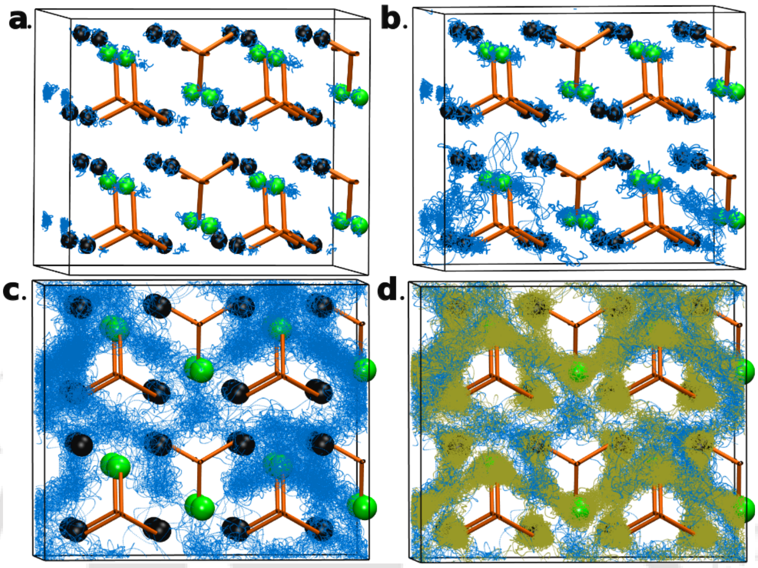

Figure 5.4: ***a.*** Simulation box after 15 ps of standard AIMD. ***b.*** Simulation box after 15 ps of MTD run. ***c.*** Simulation box after 750 ps of MTD run showing only the tagged-Li^{+} in the three-dimensional framework. ***d.*** Same as *c* but with all the Li^{+} in the system.

Table 5.1: Relabeling of the crystallographic sites of orthorhombic ($Pmn2_1$) γ-Li$_3$PS$_4$.

Wyckoff notation	label used in Ref [6, 7]	Color codes
2a	2a	G (green)
4b	4b	B (black)
2a	I, I$_1$	M (mauve)
2a	I$_1$, I$_2$	C (cyan)
4b	II, II	R (red)

5.3.1 Migration mechanism:

Apart from the two previously reported crystallographic sites, Lepley *et al.* [6] and Yang *et al.* [7] have reported three more different interstitial sites in γ-Li$_3$PS$_4$. However, the reports have labelled these Li sites inconsistently[6, 7]. In the absence of standard notations we shall refer to these sites by the color codes listed in Table 5.1 for the ease of description.

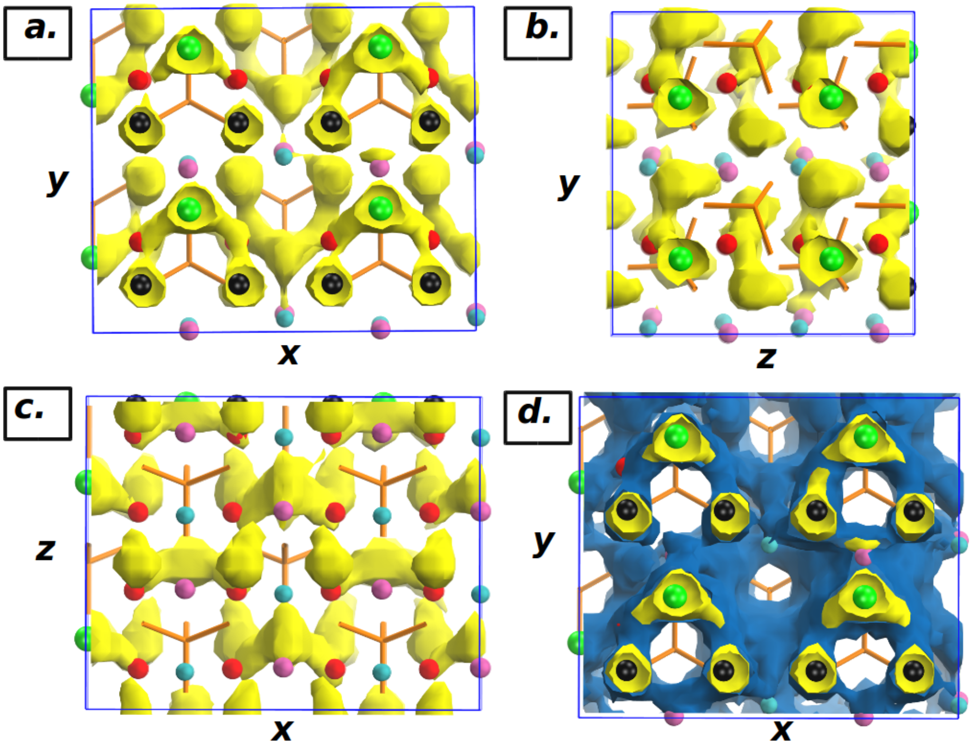

Figure 5.5: Atomic density distribution of Li^+-ion calculated from the trajectory at 400 K is shown for two different iso-values. In panel a, b, and c, in yellow, the higher iso-value is shown for different planes and panel d, in blue, the lower iso-value. The reported Li sites are also shown, *2a* sites-'green balls' (**G**), *4b* - 'black balls' (**B**), I_1-'mauve balls' (**M**), I_2-'cyan balls' (**C**), II-'red balls' (**R**).

The resulting trajectory (Figure 5.4d) of all the Li^+-ions in the system are analysed to investigate the microscopic diffusion mechanism in the system. Atomic densities shown in Figure 5.5 depict the channels connecting these five sites. Two different iso-values are shown, Figure 5.5 **a**, **b**, **c**, in yellow (of higher density) and Figure 5.5 **d** in blue (of lower density).

Based on the atomic density distribution of Li^+ in the system the following observations are noted.

- It is seen that the primary migration pathways have been formed connecting one G-site and two B-sites and thus forming discrete 'V' shaped sections arranged in up and down formation (V+ and V-) predominantly lying on the xy-plane. The distance between the G and B sites in each of these 'V+/V-' shape is found to be 3.6 Å. It is noticeable that in each of the 'V' shaped channels, the path between the G and B sites passes through the interstitial site R, though slightly off reported location.

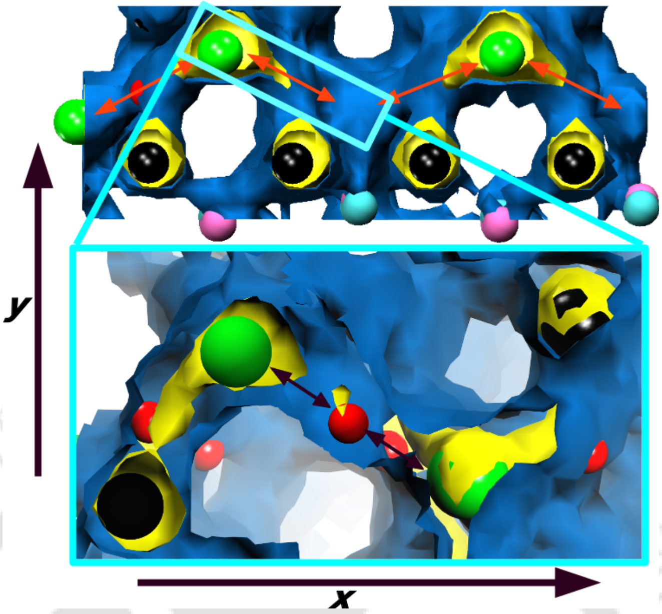

Figure 5.6: Li^{+}-ion pathway spanned over the xz-plane made of the $G(V+)$ - R - $G(V-)$ connectivity as obtained from the atomic density calculated from the trajectory data. The enlarged image is produced by zooming in the density. The some differences in the appearance between the actual and the enlarged image is due to the apparent 'loss' of the top layer of density from the 'visual' range.

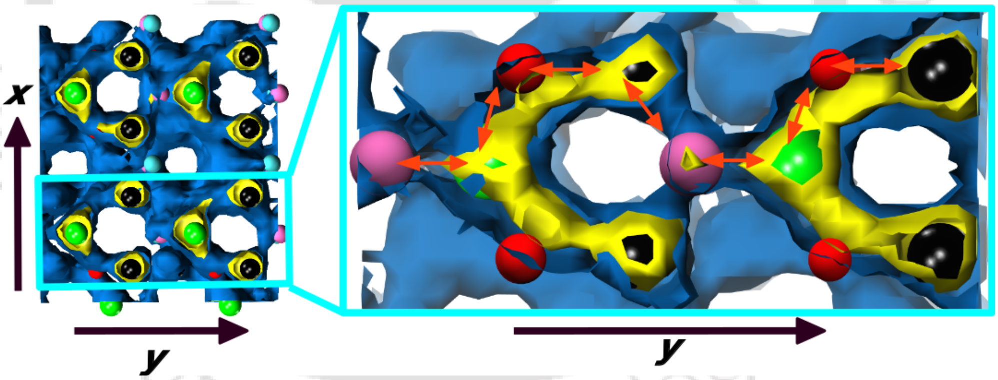

Figure 5.7: Li^{+} migration pathway along y-axis through the $G(V+) - R - B(V+) - M - G(V+)$ connecting two V+ sections along y-axis.

- Depicted in figure 5.6, two neighbouring V+ and V- sites are further connected through the R-sites that is located between the G and B sites of the V-sections. This connectivity (*G(V+)-R-G(V-)*) essentially results a continuous diffusion channel across the xz-plane. Yang *et al.* [7] also suggested this pathway along the x-axis.

- Along y-axis (Figure 5.7), another path is observed, connecting two neighbouring V+ sites through the M sites. The path is connected as *G(V+)-R-B(V+)-M-G(V+)*.

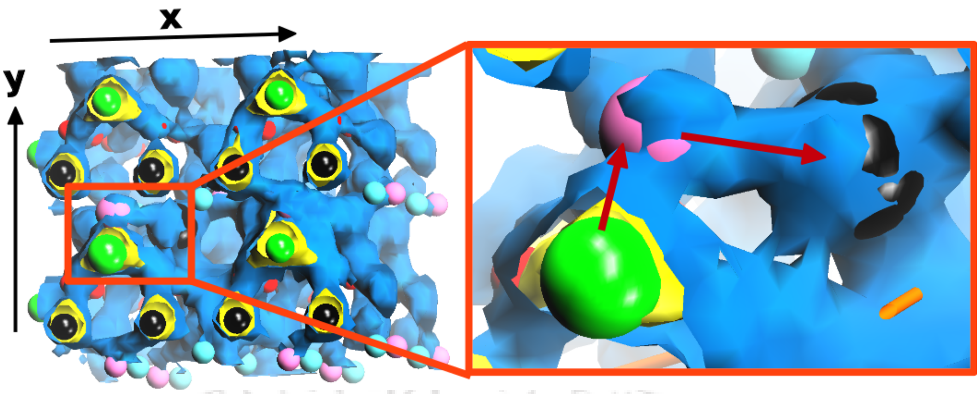

Figure 5.8: Li^+ migration pathway, connecting G-site of a V+ section to the B-site of the neighbouring V- section via $G(V+)$ - M/C - $B(V-)$

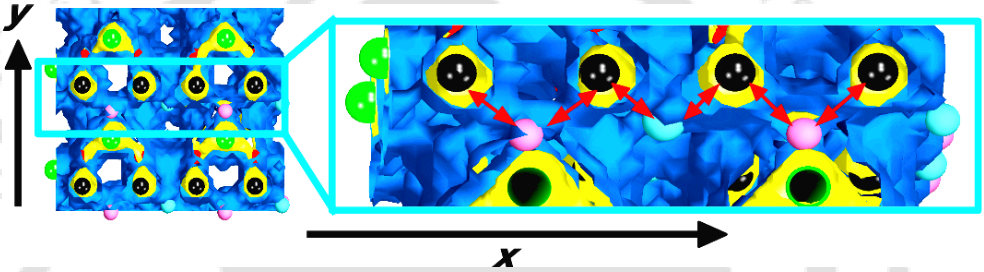

Figure 5.9: Li^+ migration pathway connecting two V+ sections (as shown in figure 5.7) along y-axis via $B(V+)$ - M - $B(V+)$ - C - $B(V+)$.

This pathway along the y-axis was also reported by Yang *et al.* [7].

- Figure 5.8 shows another pathway, connecting the G-site of a V+ to the B-site of the neighbouring V-, via either a M-site or a C-site as M and C appears alternatively. It can be described as *G(V+)-M*/*C-B(V-)* largely on the xz-plane. This particular mechanism is also reported in the previous studies [6, 7].
- Another pathway made of from the sections of the path along the y-axis described earlier has been observed (Figure 5.9). In this case, the two '*B(V+)* - *M* - *B(V+)*' are further connected by another C site, resulting a continuous channel spread over the xz-plane.

Pathway made of direct jumps between any of the interstitial sites are not found within the time length of the simulation which agrees with the observation of Lepley *et al.* [6], although Yang *et al.* [7] have proposed such mechanism.

5.3.2 Energy Landscape

5.3.2.1 NEB :

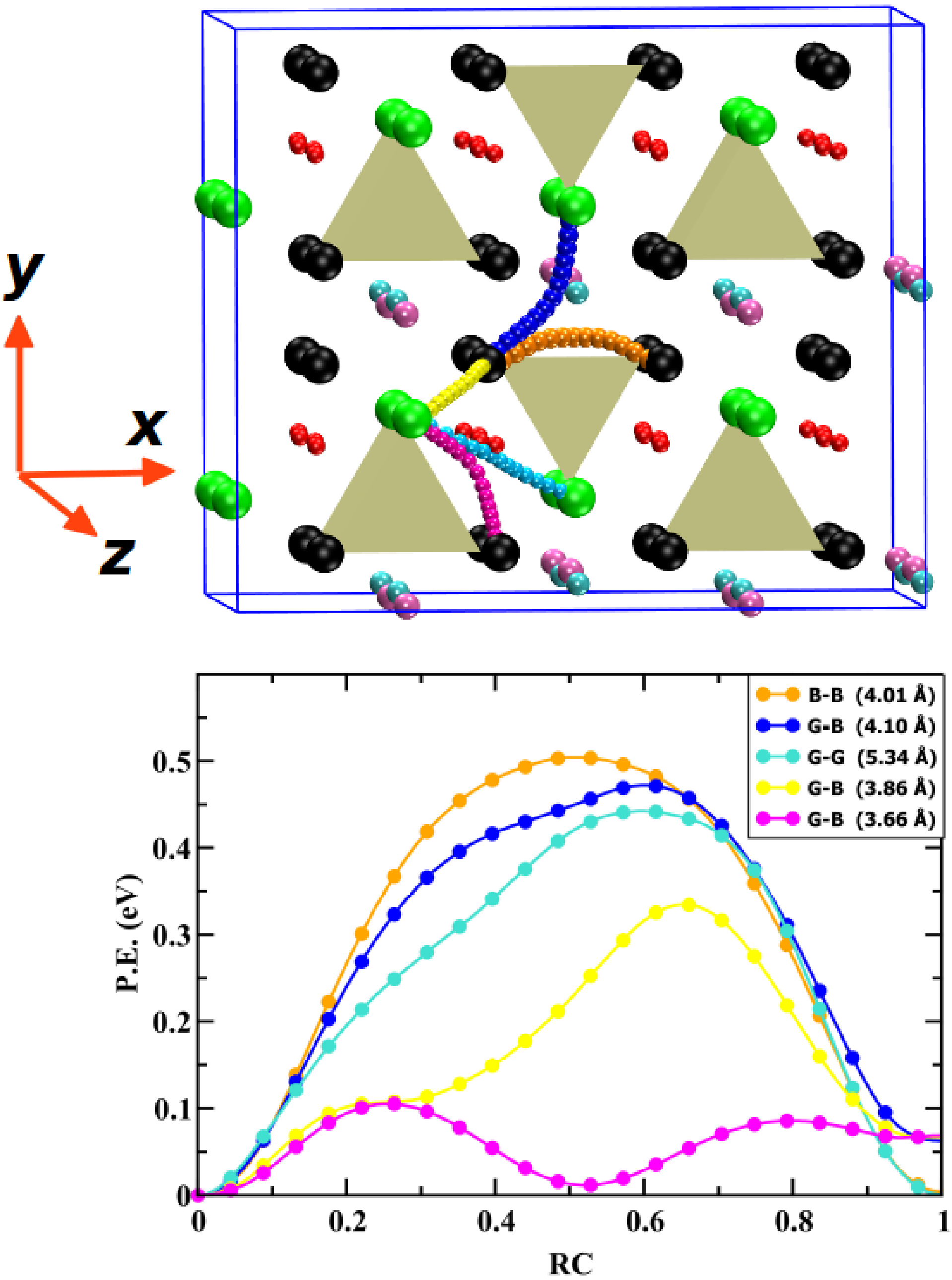

Figure 5.10: *Top*: The minimum energy paths obtained from CI-NEB for different jumps shown in different colors. *Bottom*: The corresponding energy barriers.

The potential energy barrier is calculated for each of the above described pathways employing CI-NEB method. Figure 5.10 shows the different pathways (*above*) and the corresponding potential energy barrier (*below*) in different colors. The barrier between a G-site and a B-site of one of the 'V' shaped section, is found to be 0.1 eV with a depth around the mid distance (shown in pink color). This is the lowest energy barrier among all the pathways which further confirms the previous observation (Figure 5.5, *left*) that the primary migration channels are formed between these sites. Also, the depth around the mid distance indicates the presence of an energetically favourable intermediate site (R). This barrier height is also in agreement with the previous report [7].

Second lowest energy barrier (0.3 eV) is found for the pathway connecting G and B-sites of two consecutive V- and V+ sections (shown in yellow color). It is to note that the minimum energy path obtained from CI-NEB shows a direct connectivity between the G(V+) and B(V-) sites that is not passing through any of the interstitial sites. Although this behaviour is in agreement with previous computational (NEB) reports [6, 7], the trajectory obtained from MTD simulation contradicts this. Shown earlier in figure 5.8, the pathway clearly passes through one of the interstitial sites (M/C). AT this point the reason of such mismatch is unknown.

The other three energy barriers are found to be ranging between 0.4 - 0.5 eV. The G-G pathway along the xz-plane (shown in 'cyan' color), shows a barrier of 0.4 eV. The G-B pathway connecting two V+ sections along y-axis (shown in 'blue') shows a barrier around 0.45 eV. As discussed earlier (Figure 5.7), this particular path is a part of the long connectivity along the y-axis. In this case also, unlike the MTD trajectory, the NEB pathway doesn't (although very close to M/C) passes through any of the interstitial sites. The B-B path along x-axis (shown in 'orange') shows a energy barrier of 0.5 eV, turning out to be of the highest energy barrier.

The observations from the CI-NEB calculation suggest that there are pathways for Li^+-ion with energy barrier as low as 0.1 eV and as high as 0.5 eV, which implies that although discrete channels of Li^+ can form owing to the low energy barriers along some pathways (the V shaped local networks), but to form a three dimensional well percolated diffusion network, the Li^+-ions essentially have to overcome a higher energy barriers ranging up to 0.5 eV. It is to mention here that previous experimental studies also have reported the activation energy for γ-Li$_3$PS$_4$ to be 0.5 eV [3, 14].

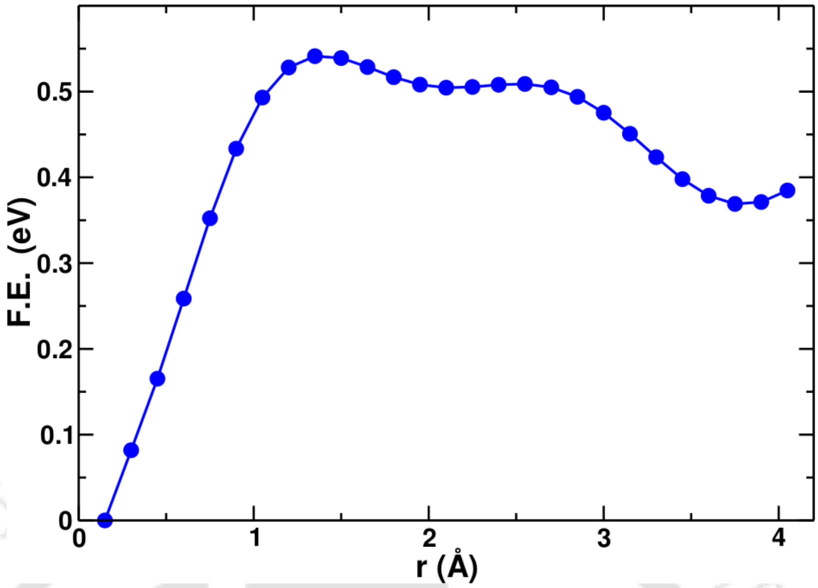

Figure 5.11: Free energy profile calculated from the bias potential obtained from the MTD at 400 K

5.3.2.2 Free Energy:

The underlying free energy barrier is also calculated from the information of the bias potential deposited on the tagged Li^+-ion. The overall barrier height obtained is 0.53 eV (Figure 5.11), which is consistent with the findings from the NEB. It noticeable that the energy minima appears at around 4.0 Å, which corresponds to the first nearest neighbours of a given Li^+-ion as discussed earlier. Here it shall be noted that in $\gamma - Li_3PS_4$, the arrangement of the mobile ion species is more complex than in the NASICONs (discussed in the previous chapter) and consequently, the jumping mechanisms follow a rather complex network involving five different sites. Unlike NASICONs, here multiple neighboring pairs exist with comparable distances (4.0 Å) with different underlying energy barriers. To determine the energy barriers for these different pathways from the information of the bias potential, perhaps a different approach is needed. As for now, only the averaged, overall barrier is shown.

5.3.3 Polyhedral flexibility

In figure 5.12, the top panel shows the same PS$_4$ tetrahedron, picked up from the simulation cell of standard-AIMD (*left*) as well as from MTD (*right*). Shown in red are the dynamic distribution of the S-ion trajectory generated during the simulations. Larger

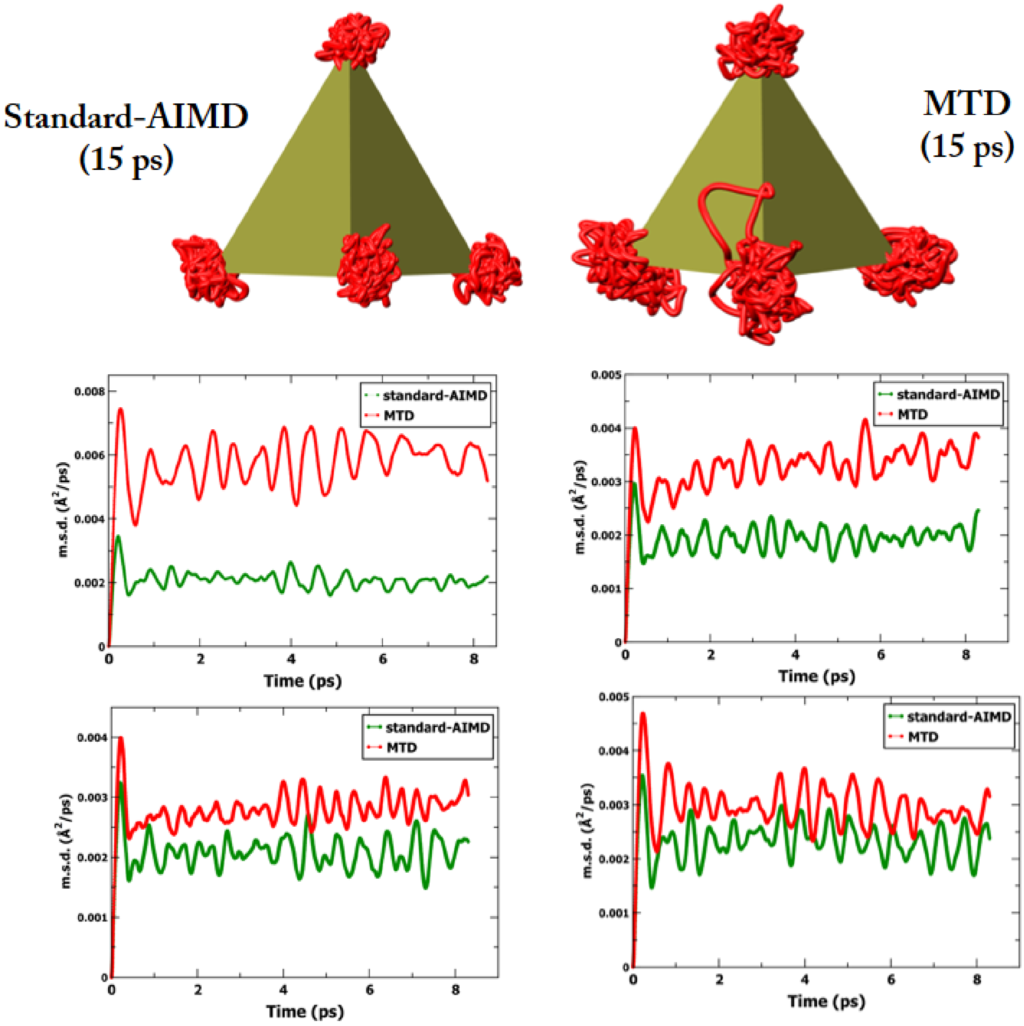

Figure 5.12: *Top panel:* Dynamic distribution of S ion shown for a PS$_4$ tetrahedron, obtained from standard-AIMD and MTD simulations at 400 K over a run-length of 15 ps. *Bottom panel*: The corresponding mean squared displacements of the four S-ion constituting the tetrahedron.

wobbling of PS$_4$-tetrahedra is noticeable in the 15 ps MTD run compared to the same obtained from the same time-length of standard-AIMD. Previously, in figure 5.4, it is shown that with the said simulation length, no Li^+ diffusion is observed in case of the standard-AIMD, whereas the tagged Li^+ in MTD case started diffusing driven by the applied bias potential. It is to mention here, that the PS$_4$ tetrahedron shown here is adjacent to the initial position of the tagged Li^+-ion. This observation points towards the possible existence of a correlation between the Li^+-ion dynamics, and as reflected in the larger wobbling of PS$_4$ tetrahedra, with that of the framework tetrahedra. The second and the third panels of figure 5.12 shows the mean squared displacements (msd),

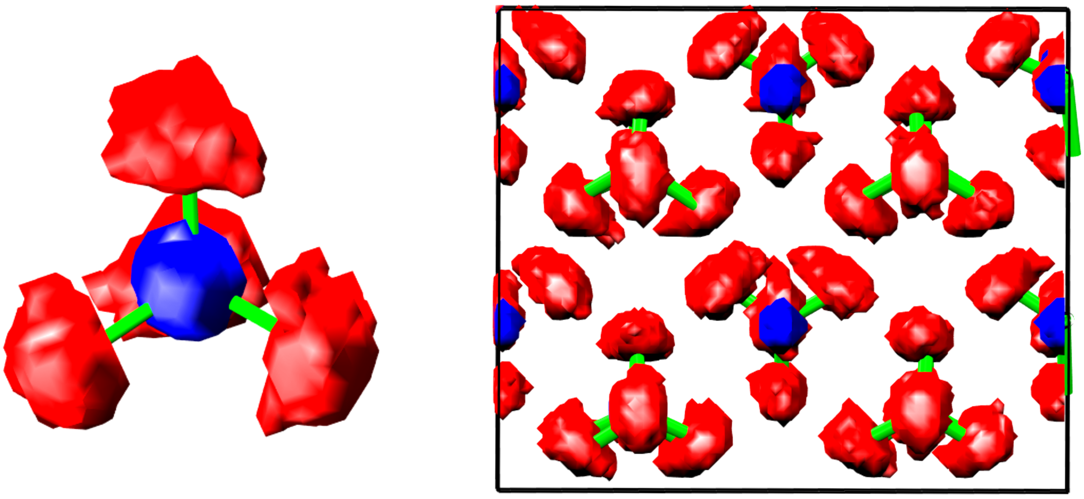

Figure 5.13: Atomic density distribution of both P and S from a PS$_4$ tetrahedron, calculated from the MTD trajectory data of the length of 750 ps, at 400 K. *Left*: the same tetrahedron shown in figure 5.12. *Right*: The entire simulation box.

calculated for standard-AIMD and MTD, of the four S ions that construct the tetrahedra. For all four S, larger msd is observed for the MTD case, where the Li^+ diffusion is accelerated.

Role of Polyhedral rotation on ion transport has gained significant attention in past few years. In many materials, the coupled dynamics of cation-anion is shown to have crucial role in facilitating higher ionic diffusion [15–20]. In β-Li$_3$PS$_4$ similar orientational dynamics of the framework tetrahedra has been observed previously. Further, recently it has also been reported that partial substitution of P with Si can stabilize the ‘rotor phase’ at room temperature [21] in which the P/Si$-$S$_4$ rotation flattens the energy barrier associated with cation diffusion.

Studies have suggested that crystalline γ-Li$_3$PS$_4$ does not have such orientational degrees of freedom for the framework tetrahedra [16, 21]. Yet, intrigued by the comparatively larger wobbling of the framework tetrahedra, we calculated the atomic density distribution of the PS$_4$ tetrahedron from the entire 750 ps trajectory data (Figure 5.13) to show the dynamics of the framework tetrahedra.

5.4 Conclusion

To conclude, following the approach mentioned in chapter 4, metadynamics technique has been employed within AIMD simulation using the position of a single Li^{+} as the collective variable, and the migration mechanism in slow diffusing $\gamma - Li_3PS_4$ at 400 K is investigated. Well percolated migration pathways is obtained, owing to the accelerated diffusion caused by the bias potential. Various jump processes are examined by analysing the trajectory data. Five different diffusion pathways has been identified, and the results are compared with the available literature.

The overall free energy barrier calculated from the information of the applied bias potential is found to be $0.53\, eV$. Using CI-NEB method, the potential energy barrier is calculated for each of the jumping mechanisms and it is found that energy barriers ranging between $0.1 - 0.5\, eV$ exists for different pathways. It is noted that local diffusion networks are easily formed owing to low energy barrier ($0.1\, eV$), however long-range diffusion channels spanning the system costs higher effective energy barriers of $0.5\, eV$.

Further, the dynamics of the framework tetrahedra has also been analysed. The results suggest possible correlation between the Li^{+}-ion mobility in γ-Li$_3$PS$_4$ with the framework tetrahedra.

BIBLIOGRAPHY

[1] Ö. U. Kudu, T. Famprikis, B. Fleutot, M.-D. Braida, T. Le Mercier, M. S. Islam and C. Masquelier, *J. Power Sources*, 2018, **407**, 31–43.

[2] K. Homma, M. Yonemura, M. Nagao, M. Hirayama and R. Kanno, *J. Phys. Soc. Jpn.*, 2010, **79**, 90–93.

[3] K. Homma, M. Yonemura, T. Kobayashi, M. Nagao, M. Hirayama and R. Kanno, *Solid State Ionics*, 2011, **182**, 53–58.

[4] S. Iikubo, K. Shimoyama, S. Kawano, M. Fujii, K. Yamamoto, M. Matsushita, T. Shinmei, Y. Higo and H. Ohtani, *AIP Adv.*, 2018, **8**, 015008.

[5] Z. Liu, W. Fu, E. A. Payzant, X. Yu, Z. Wu, N. J. Dudney, J. Kiggans, K. Hong, A. J. Rondinone and C. Liang, *J. Am. Chem. Soc.*, 2013, **135**, 975–978.

[6] N. Lepley, N. Holzwarth and Y. A. Du, *Phys. Rev. B*, 2013, **88**, 104103.

[7] Y. Yang, Q. Wu, Y. Cui, Y. Chen, S. Shi, R.-Z. Wang and H. Yan, *ACS Appl. Mater. Interfaces*, 2016, **8**, 25229–25242.

[8] J. Yang and S. T. John, *Comput. Mater. Sci.*, 2015, **107**, 134–138.

[9] P. Giannozzi, S. Baroni, N. Bonini, M. Calandra, R. Car, C. Cavazzoni, D. Ceresoli, G. L. Chiarotti, M. Cococcioni, I. Dabo *et al.*, *J. Phys. Condens. Matter*, 2009, **21**, 395502.

[10] P. Giannozzi, O. Andreussi, T. Brumme, O. Bunau, M. B. Nardelli, M. Calandra, R. Car, C. Cavazzoni, D. Ceresoli, M. Cococcioni *et al.*, *J. Phys. Condens. Matter*, 2017, **29**, 465901.

[11] P. Giannozzi, O. Baseggio, P. Bonfà, D. Brunato, R. Car, I. Carnimeo, C. Cavazzoni, S. De Gironcoli, P. Delugas, F. Ferrari Ruffino *et al.*, *J. Chem. Phys.*, 2020, **152**, 154105.

[12] G. A. Tribello, M. Bonomi, D. Branduardi, C. Camilloni and G. Bussi, *Comput. Phys. Commun*, 2014, **185**, 604–613.

[13] G. Henkelman, B. P. Uberuaga and H. Jónsson, *J. Chem. Phys.*, 2000, **113**, 9901–9904.

[14] M. Tachez, J.-P. Malugani, R. Mercier and G. Robert, *Solid State Ionics*, 1984, **14**, 181–185.

[15] Z. Zhang, P.-N. Roy, H. Li, M. Avdeev and L. F. Nazar, *J. Am. Chem. Soc.*, 2019, **141**, 19360–19372.

[16] J. G. Smith and D. J. Siegel, *Nat. Commun.*, 2020, **11**, 1–11.

[17] G. K. P. Dathar, J. Balachandran, P. R. Kent, A. J. Rondinone and P. Ganesh, *J. Mater. Chem. A*, 2017, **5**, 1153–1159.

[18] T. Famprikis, J. A. Dawson, F. Fauth, O. Clemens, E. Suard, B. Fleutot, M. Courty, J.-N. Chotard, M. S. Islam and C. Masquelier, *ACS Mater. Lett.*, 2019, **1**, 641–646.

[19] K. Sau, T. Ikeshoji, S. Kim, S. Takagi, K. Akagi and S.-i. Orimo, *Phys. Rev. Mater.*, 2019, **3**, 075402.

[20] K. Sau and T. Ikeshoji, *J. Phys. Chem. C*, 2020, **124**, 20671–20681.

[21] Z. Zhang, H. Li, K. Kaup, L. Zhou, P.-N. Roy and L. F. Nazar, *Matter*, 2020, **2**, 1667–1684.

CHAPTER 6

CONCLUSION

Ion conducting solids find numerous technological applications, particularly in energy storage devices. The traditional liquid/gel electrolytes, which continues to find use even in the present day Li^+-ion batteries, poses several health and safety hazards. Replacing them with solid electrolytes promises higher energy density, wider operational window, better chemical stability, longer life-cycles and superior safety standards. Thus the design of *all-solid-state-battery* is one of the major directions of concurrent research. Alkali ion conductors, specially Li^+/Na^+-ion conductors, are perceived to be the most promising candidates for the development of *all-solid-state-batteries*. Chapter-1 of the thesis surveys the current status of the research activity, including experimental as well as computational studies, on Li^+/Na^+- conducting materials,. Tailor making of potential material for commercial uses demands a concerted approach of both experimental and computational studies. In the works presented in this thesis, atomistic simulation studies have in carried out on promising materials to address various issues. The theoretical background of the methods used for the studies are described in the chapter-2.

Chapter-3 discusses the effect of framework dynamics on ion transport in Li^+ substituted NASICONs, $LiM_2(PO_4)_3$ where M=Zr, Hf, Sn and Ti. Classical MD has been employed for the study, using potential parameters proposed earlier for the *true*-NASICON family, $Na_{1+x}Zr_2Si_xP_{3-x}O_{12}$, where $0 \le x \le 3$. It is found that the Li^+-ion conductivity in $LiM_2(PO_4)_3$ decreases with the radius of the M-ion, in qualitative agreement with previous experimental studies. This is attributed to the reduction in the size of the geometrical bottleneck in the conduction channel. The present work further investigates this aspect to find that the geometrical bottlenecks in the conduction channel are sensitive to approaching Li^+-ions. It is noted that simulations with *frozen-in* framework results in significant drop in the Li^+ diffusion. Thus a strong correlation between framework dynamics and ion diffusion is proposed.

Chapter-4 demonstrates the utility of metadynamics technique in the study of slow diffusing systems. Metadynamics is an accelerated sampling technique for 'rare-events' in which external repulsive Gaussian-shaped potentials or 'hills' are applied on the appropriate collective variable (CV) at intervals so as to drive the system out of its local minima. For the study, the phosphate and silicate end members of the *true*-NASICON family, namely $NaZr_2(PO_4)_3$ and $Na_4Zr_2(SiO_4)_3$, are chosen which are relatively low conducting materials. *Well-tempered* metadynamics technique has been employed within canonical ensemble (NVT) classical MD simulations, with the position of a single Na^+-ion chosen as the CV. The free energy landscape is later reconstructed from the information of the external potentials deposited. MTD simulations have been carried out at 500 K for 100 ns and 200 ns for $NaZr_2(PO_4)_3$ and $Na_4Zr_2(SiO_4)_3$ respectively. The convergence of free energy barriers with the progress of the simulation has been demonstrated. The free energy barriers for Na^+-ion migration in these systems are compared with the potential energy profiles of individual Na^+ ions as well as that from NEB calculations. In $NaZr_2(PO_4)_3$ the energy barriers calculated from different methods are found to be in good agreement with each other. However, for $Na_4Zr_2(SiO_4)_3$ the free energy barrier from metadynamics differs from the individual potential energy profiles of Na^+ ions as well as with the NEB calculations. This is attributed to the strongly correlated Na^+ dynamics in the system. Trajectory analysis of neighbouring Na^+ ions demonstrates simultaneous hops of ions, supporting the proposal of correlated movement of ions in the system. The investigation also provides certain insights related to the optimal tuning of 'hills' for improving the efficiency of MTD sampling.

In Chapter-5, the utility of the metadynamics technique has been extended to the low diffusive γ-Li_3PS_4 system to understand the diffusion mechanism associated with the Li^+ in the system. *Ab-initio* MD simulations, coupled with well-tempered metadynamics is performed for a time length of 750 ps at a temperature of 400 K in the NVT ensemble. Well connected Li^+ migration pathways have been achieved, analyses of which showed various hops to neighbouring sites, producing a complex ion migration network. The overall free energy profile has been calculated from the information of the applied bias potentials. Also, in order to find the energy barriers for the individual hops, CI-NEB calculations are carried out based on the hopping mechanisms obtained from the metadynamics trajectory. Analysis of the trajectories show that there are clusters of 'local' Li^{+} sites, which are well inter-connected with low energy barriers (0.1 eV). These clusters, however, are connected through percolation channels of large energy barriers (0.5 eV). Further, the dynamics of the framework tetrahedra has also been investigated. It has been observed that the accelerated Li^{+} diffusion driven by the applied bias potential, has caused larger wobbling in the framework tetrahedra. The observation indicates a possible coupling between the two.

Hopefully, the works presented in this thesis will contribute to the concurrent research in the field of solid state ionics.

APPENDIX

A

APPENDIX FOR CHAPTER 4

A.1 Correlated Dynamics of Na^+ in $Na_4Zr_2Si_3O_{12}$

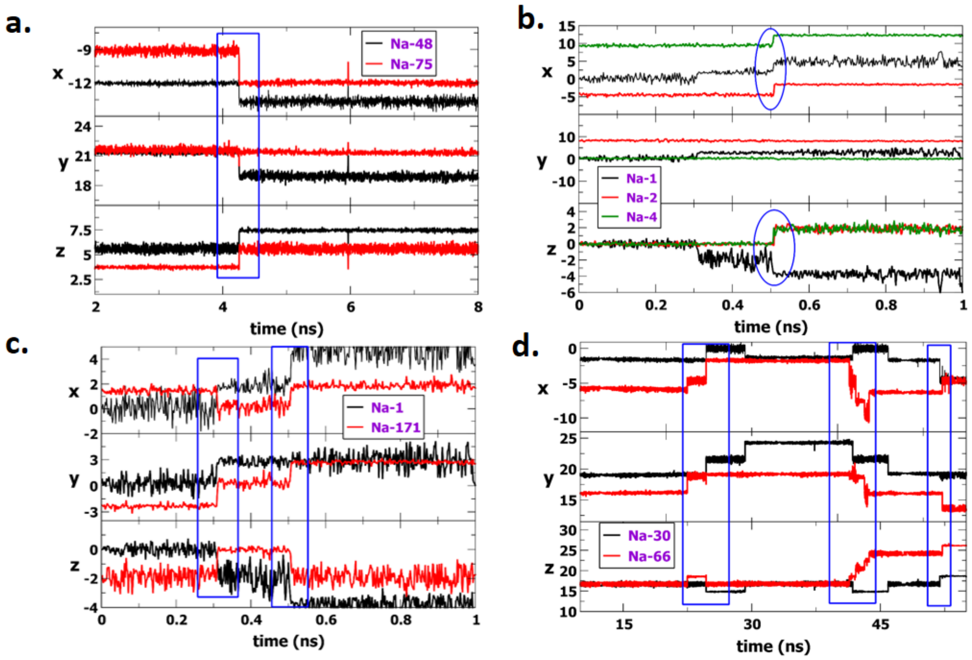

Figure A.1: The time-evolution of the Cartesian coordinates of a few randomly picked Na^+ ions and some of their respective neighbours from MTD simulation of $Na_4Zr_2Si_3O_{12}$ at 500 K (with the bias factor, γ = 6). The simultaneous changes in the x,y or z –coordinates of different ions indicates correlated hops of neighbouring ions - a few are highlighted.

To demonstrate the correlated motion of Na^+-ion in $Na_4Zr_2Si_3O_{12}$, A few Na^+ is picked up from the system, along with their nearest neighbours. Then there trajectory is plotted as a function of the simulation time. At multiple instances, simultaneous movements are visible (Figure A.1).

A.2 Bias Factor Dependence

Shown in figure A.2 are the simulation boxes with the tagged Na^+ trajectory, obtained from two different bias factors (γ) values (3 and 9) for both $NaZr_2P_3O_{12}$ and $Na_4Zr_2Si_3O_{12}$.

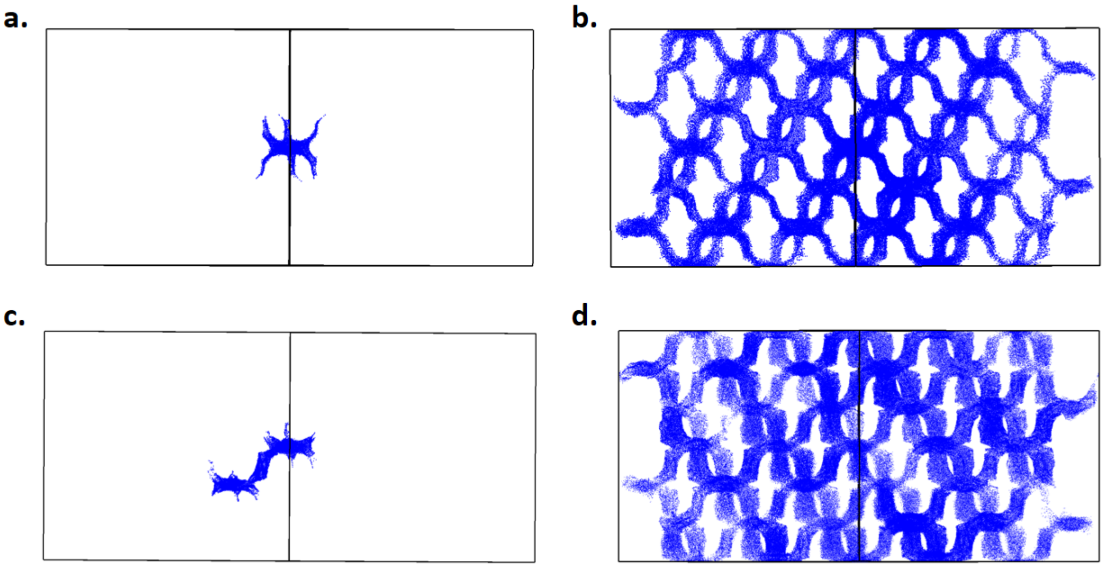

Figure A.2: Statistical distribution of the tagged Na^+ ion (panels a, b) for $NaZr_2P_3O_{12}$, respectively for γ = 3, and 9, during the 100 ns of MTD simulation at 500 K; and (panels c, d) for $Na_4Zr_2Si_3O_{12}$, respectively for γ = 3, and 9 during the 200 ns MTD simulation at 500 K.

A.3 Site Exploration

Distance of the tagged 'Na^+' from its initial location as a function of the time elapsed (figure A.3a) for $NaZr_2P_3O_{12}$, and (figure A.2b) for $Na_4Zr_2Si_3O_{12}$ from MTD simulations at 500 K, for bias factor γ = 6. In panels c) and d) of figure A.2 an enlarged view of the short time behaviour of Na^+ ions are shown respectively for $NaZr_2P_3O_{12}$ and $Na_4Zr_2Si_3O_{12}$ systems. It shall be noted in figure A.3c) that the tagged ion makes several unsuccessful hops to its neighbours at 6.4 Åwithin about 1.6 ns before hoping off from the initial Na1 site. Figure A.3d) also shows several attempts by the tagged Na^+ to reach the neighbouring Na2 site (3.4 Å) before it succeeds. The motion of the ion in its newer sites also follow this pattern. In figure A.3a) and b) there are instances when the tagged ion after diffusing off to distance sites returns close to the original site, respectively after durations of 80 ns and 60 ns. Thus, the ion explores the local minima quite extensively before diffusing off, thus ensuring the quality of the sampling.

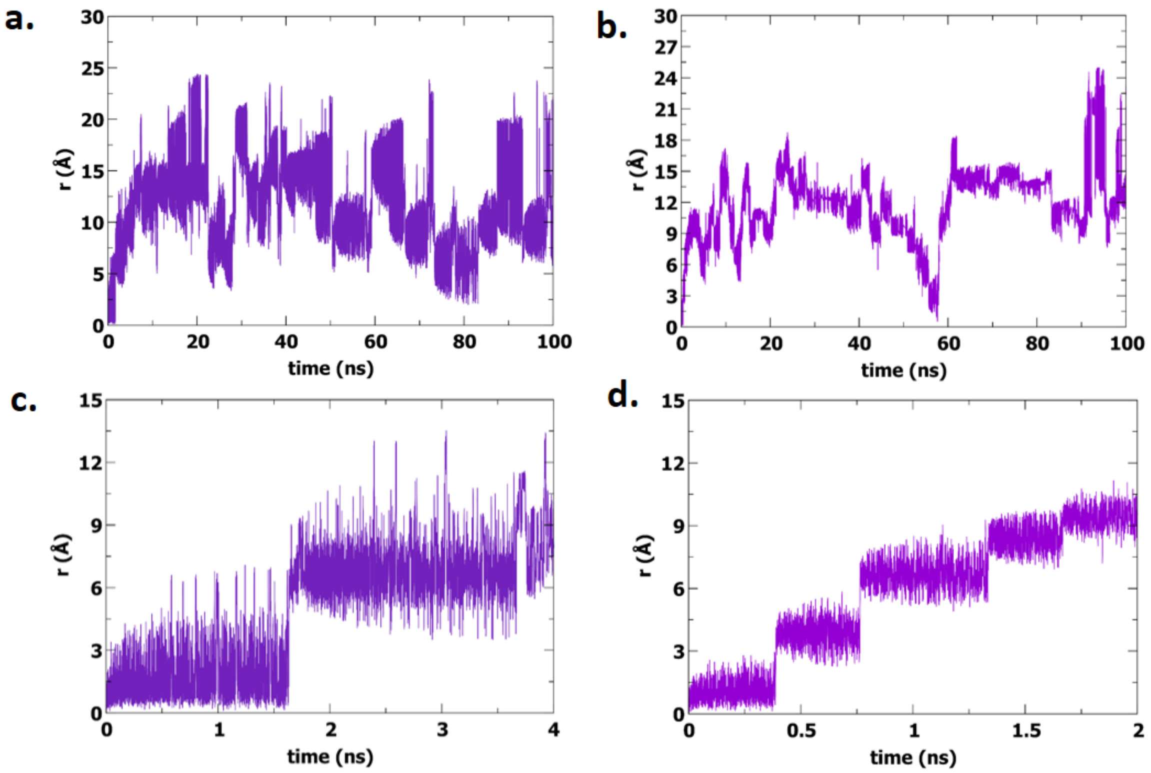

Figure A.3: Distance of the 'tagged' Na^+ from it's initial position as a function of the simulation time, shown for $NaZr_2P_3O_{12}$ (panel a and c) and for $Na_4Zr_2Si_3O_{12}$ (panel b and d), at 500K and for $\gamma = 6$

A.4 Comparison of Free Energy barrier

Figure A.4 shows the free energy profiles calculated for two different bias factors (γ = 6, 9) for $NaZr_2P_3O_{12}$ (*left*) and $Na_4Zr_2Si_3O_{12}$ (*right*). It is to note that the simulations are performed for $\gamma = 6\, and\, 9$ are with different choice of the Na^+ as the 'tagged' one.

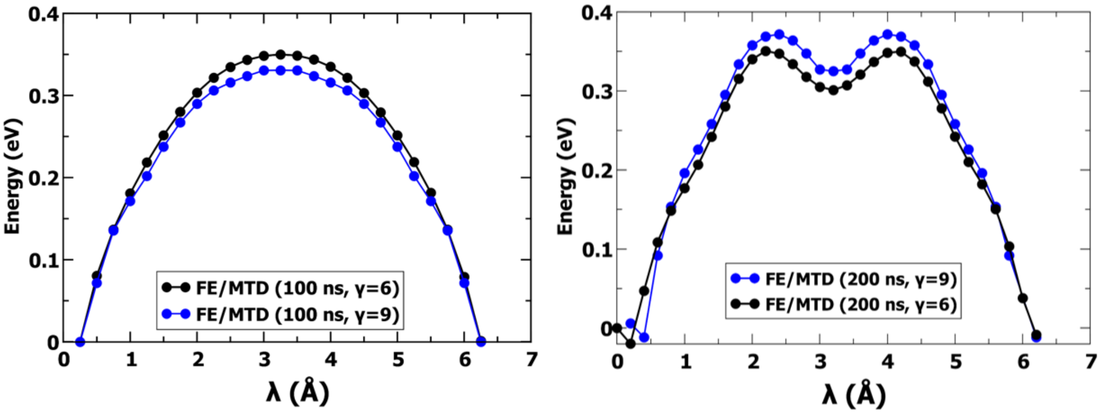

Figure A.4: Free energy profiles for γ= 6 and 9, for $NaZr_2P_3O_{12}$ (*left*), and $Na_4Zr_2Si_3O_{12}$ (*right*) from MTD simulations at 500 K.

Publications Based On the Works

1. Krishnanjan Pramanik, Kartik Sau, and P. Padma Kumar, “**Role of Framework Flexibility in Ion Transport: A Molecular Dynamics Study of $LiM_2^{IV}(PO_4)_3$**", *The Journal of Physical Chemistry C*, 2020, 124(7), 4001-4009.

2. Krishnanjan Pramanik, Sangkha Borah, P. Padma Kumar, “**Accessing Slow Diffusion In Solids Employing Metadynamics Simulation**", *Physical Chemistry Chemical Physics*, 2020, 22, 22796-22804.

3. Krishnanjan Pramanik, Sangkha Borah, P. Padma Kumar, “**Understanding** *Li*-**ion Migration Mechanism in γ-Li_3PS_4: A First Principle Based Study Employing Metadynamics and NEB**" (*manuscript under preparation*)

Conferences/Workshops attended

- Theoretical Chemistry Symposium, IISER Pune, during Dec 18-21, 2014. [Poster presentation]

- National Workshop on Atomistic Simulation Technique, during Dec 21-24, 2015, IIT Guwahati. [Instructor: hands-on-session]

- A Discussion Meeting on Recent Advances In Molecular Simulations, IISc Bangalore, during Feb 8-11, 2018. [Poster presentation]